which each ridge lineshape will be aligned in the two-dimensional spectrum obtained. For example, for a spin $I = 3/2$ nucleus $A^4(I,3/2)/A^4(I,1/2) = (-6/5)/(54/35) = -7/9$. All coefficients $A^n(I,m_I)$ are given in Table 2.2.

The two-dimensional time-domain dataset obtained during any MQMAS experiment is then Fourier transformed to produce a spectrum displaying signal corresponding to the multiple-quantum spectrum in the δ_1 dimension and the anisotropic powder pattern associated with the central transition in the δ_2 dimension. A schematic representation of an MQMAS spectrum obtained post Fourier transformation is shown in Figure 2.27(a). To achieve an isotropic spectrum a projection orthogonal to the ridge lineshape is required, as shown in Figure 2.27(a). This projection is free from all quadrupolar broadening but retains the isotropic shifts. In practice it is easier to use mathematical transformation known as shearing to obtain an isotropic projection in the δ_1 dimension. This transforms the spectrum so that the ridges appear parallel to δ_2. An example of a sheared spectrum is also shown in Figure 2.27(b). The isotropic spectrum is then more easily extracted.

Spectra recorded using the original MQMAS experiment give rise to undesirable 'phase-twist' lineshapes. A two-dimensional ^{87}Rb ($I = 3/2$) spectrum of $RbNO_3$ recorded using the original MQMAS pulse sequence is shown in Figure 2.26(b). The spectrum displays distorted lineshapes, each of which is aligned along R $(-7/9)$. There are three crystallographically distinct resonances in the ^{87}Rb MQMAS NMR spectrum of $RbNO_3$. However, owing to considerable distortion of the lineshape, caused by 'phase-twists', it is difficult to accurately observe the third site. Phase-twist lineshapes result from the real part of the two-dimensional Lorentzian containing both absorption and dispersion mode lineshapes. These are entangled in a complex manner and the lineshapes cannot be phased correctly. This is a major drawback of the original MQMAS sequence and, as a result, adjustments to the original experiment have been made to ensure pure-phase lineshapes are obtained. These 'modified' experiments are of two distinct types; amplitude- and phase-modulated with respect to t_1. The first of these, amplitude-modulated

experiments, produce pure-phase spectra if there is simultaneous selection of two symmetrical coherence pathways (e.g., p = ± 3) and if their transfer to the observable signal has the same efficiency. This sequence was first proposed by Amoureux[177] in 1996 for I = 3/2 nuclei. A modified version of this sequence was later proposed, again by Amoureux, which contained a filter through a population state, as shown in Figure 2.28.[178] This amplitude-modulated pulse sequence, known as a z-filter experiment, consists of the conventional triple-quantum excitation and conversion pulses in addition to a selective 90° pulse, used to convert the populations temporarily stored along the z-axis to observable signal. This sequence ensures equal combination of p = ±3 and can be implemented for all spins, and therefore it is a highly robust technique. Once obtained, the dataset is Fourier transformed to reveal a series of ridge lineshapes, each of which is aligned along an axis with a gradient equal to the MQMAS ratio, R, for that particular nucleus. For example, the spectrum obtained for a spin I = 3/2 nucleus will contain a series of ridges, each with a slope of −7/9. For convenience, spectra recorded using a z-filter pulse sequence are commonly shown post shearing.[179] Two-dimensional ^{87}Rb (I = 3/2) spectra recorded for $RbNO_3$ using a z-filtered pulse sequence are shown in Figures 2.28(a) and (b). The spectra shown are both prior to and post shearing.

Alternatively, a second type of experiment may be used in which a single coherence pathway is selected and the signal is phase-modulated in t_1. Initially proposed by Massiot *et al.*,[180] this is commonly achieved using a shifted-echo pulse sequence, shown in Figure 2.29. Unlike the original MQMAS experiment shifted-echo pulse sequences always result in the acquisition of pure-phase lineshapes owing to the acquisition of a whole echo. To successfully acquire a whole echo using a shifted-echo pulse sequence the correct coherence pathway must first be selected. This depends upon both the spin under investigation and the sign of the MQMAS ratio. For example, for a spin I = 3/2 nucleus R is negative and to successfully acquire a whole echo the pathway through negative multiple-quantum coherence, p = −3, (marked by the solid line in Figure 2.29) must be followed. The converse is true for I = 5/2, 7/2 and 9/2

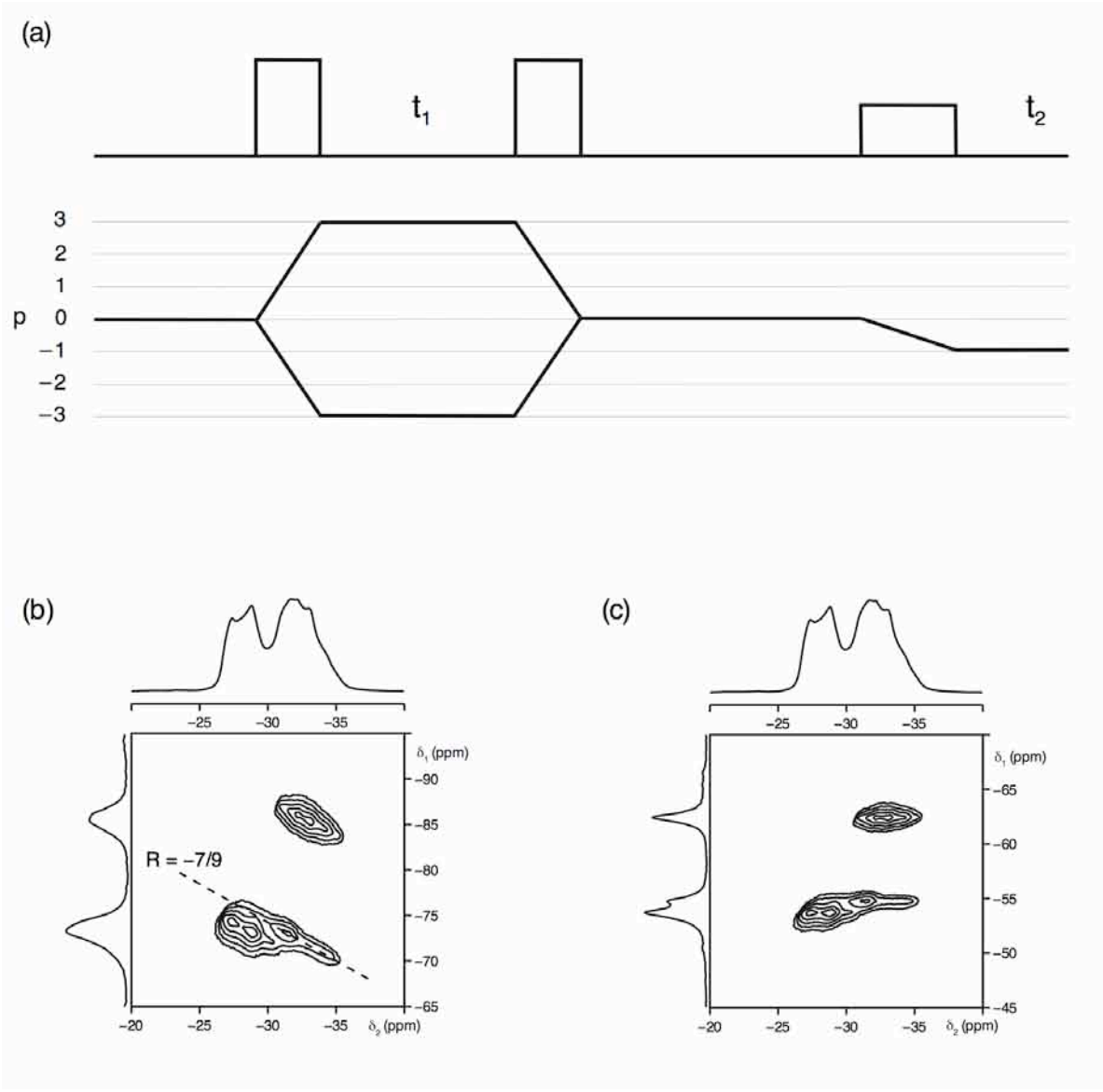

Figure 2.28: (a) Pulse sequence and coherence transfer pathway diagram for the z-filtered MQMAS NMR experiment of Amoureux.[178] (b, c) Conventional ^{97}Rb MAS (14.1 T) NMR spectra, triple-quantum MAS NMR spectra and corresponding projections for $Rb(NO)_3$, recorded using the pulse sequence shown in (a). Each spectrum is the result of averaging averaging 72 transients with a recycle interval of 0.25 s for each of the 512 increments of 60.0 μs. The two-dimensional spectrum shown in (b) exhibits a series of ridges aligned along a gradient of −7/9 (the MQMAS ratio for I = 3/2). The ^{97}Rb MAS NMR spectrum shown in (c) is post shearing, displaying a series of ridge lineshapes parallel to δ_2 and corresponding isotropic projection in the δ_1 dimension. The MAS rate was 12.5 kHz.

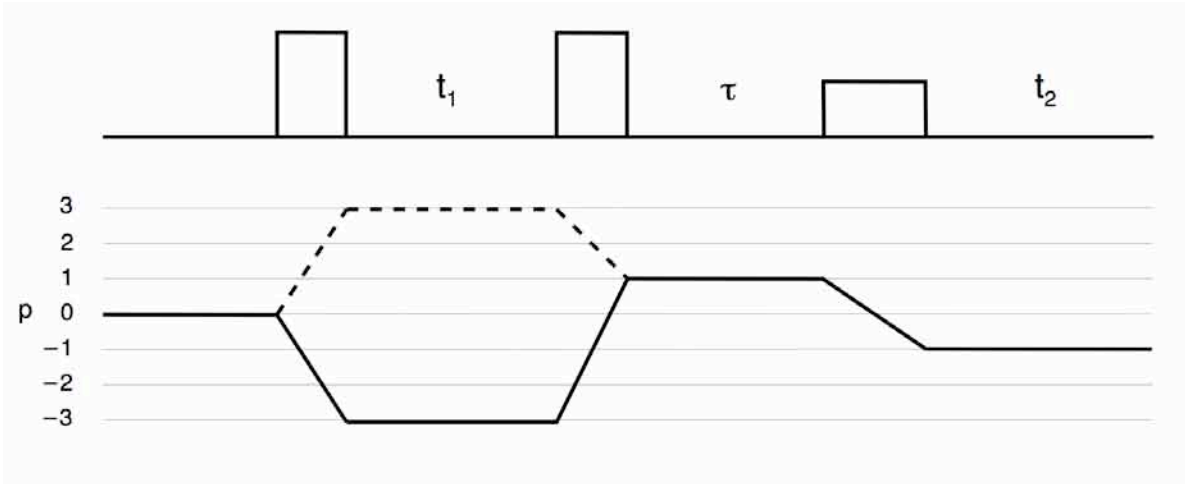

Figure 2.29: Pulse sequence and coherence transfer pathway diagram for the shifted-echo MQMAS experiment of Massiot *et al.*[180] The solid line denotes the correct coherence pathway for spin I = 3/2 nuclei and the dashed line denotes the correct coherence pathway for spin I = 5/2, 7/2 and 9/2 nuclei.

nuclei, i.e., the pathway though positive multiple-quantum coherence, p = +3, must be followed, denoted by the dashed line in Figure 2.29. For shifted-echo experiments it is important to determine the echo interval, τ, as it needs to be sufficiently long enough to acquire a whole echo. Transverse relaxation is, however, a limiting factor in precisely how far the echo can be shifted into the acquisition period, t_2. If τ is too long relaxation may begin to effect data acquisition. Hence, when relaxation causes a detrimental effect it is better to use a z-filtered experiment. Similar to the z-filtered experiment, the spectrum acquired using a shifted-echo contains a series of ridges aligned along an axis with a gradient equal to the MQMAS ratio. Hence, they too require post acquisition processing (shearing) in order to obtain ridges which appear parallel to δ_2.

Brown and Wimperis later proposed a split-t_1 approach, which may be applied to both phase- and amplitude-modulated experiments.[181] The phase-modulated split-t_1 pulse sequence, shown in Figure 2.30(a), divides the t_1 time period into two fractional contributions, kt_1 and $k't_1$, which are related to the MQMAS ratio. The key feature of each of the MQMAS experiments discussed thus far is the refocusing of the fourth-rank anisotropic broadening which occurs at some point in the t_2 period. However, if the t_1 period is split into single- and triple-quantum evolution

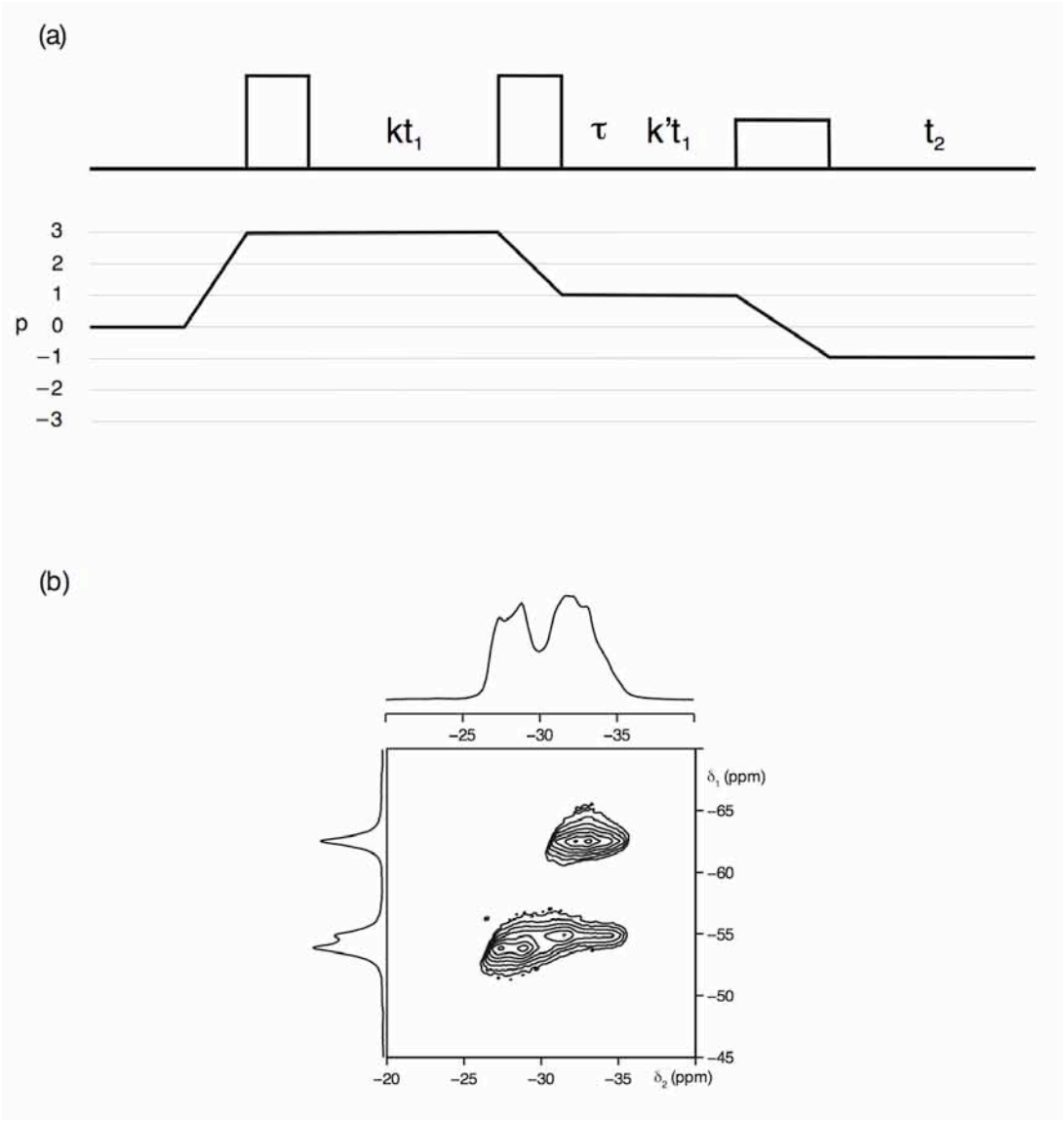

Figure 2.30: (a) Pulse sequence and coherence transfer pathway diagram for the I = 3/2 phase-modulated split-t_1 pulse sequence of Brown and Wimperis,[181] for spins I > 3/2 the $k't_1$ evolution period is placed after the 180° pulse. The t_1 time period is split into two fractional contributions, kt_1 and $k't_1$, which are related to the MQMAS ratio. (b) Conventional ^{97}Rb MAS (14.1 T) NMR spectrum, triple-quantum MAS NMR spectrum and corresponding isotropic projections for $RbNO_3$ recorded using the pulse sequence shown in (a). The triple-quantum MAS NMR spectrum is the result of averaging 96 transients with a recycle interval of 0.25 s for each of the 512 increments of 60.0 μs. The MAS rate was 12.5 kHz.

periods in a ratio determined by the relevant MQMAS ratio then the fourth-rank anisotropic broadening can be refocused at the end of the t_1 period, resulting in ridges which appear parallel to the δ_2 axis. Hence, no additional shearing transformation is required. For example, using this pulse sequence for a spin I = 3/2 nucleus a whole echo is generated utilising a coherence pathway through p = +3, with k = 9/16 t_1 and k' = 7/16 t_1. As a direct result of the splitting of the t_1 period, the spectrum produced contains ridges parallel to δ_2 without the need for shearing. The split-t_1 approach is commonly added to phase-modulated experiments with relative ease. However, it is more challenging to add to amplitude-modulated experiments as complex phase cycling is required to ensure the correct coherence transfer pathways are correlated. A two-dimensional ^{87}Rb (I = 3/2) spectrum of $RbNO_3$, recorded using a phase-modulated split-t_1 pulse sequence is shown in Figure 2.30(b), displaying three distinct resonances, in good agreement with the literature. This spectrum is also in good agreement with the sheared $RbNO_3$ spectrum shown in Figure 2.28(c) obtained using a z-filtered experiment. In each spectrum the isotropic projection onto the δ_1 axis clearly indicate the three sites.

2.9.3 Higher-Order MQMAS

There are various versions of the MQMAS technique including three-, five-, seven- and nine-quantum experiments. There is, however, considerable debate within the literature regarding the associated advantages and disadvantages of using experiments with greater changes in coherence order. Higher-order, principally five- (quintuple-) quantum MAS experiments, were initially introduced by Fernandez and Amoureux in 1995.[182,183] Their early work reported 'extraordinarily high' resolution for spectra recorded using the five-quantum MAS experiment. Work by Wang *et al.*,[184] also suggested similar findings by successfully resolving two aluminum sites which could not be resolved using conventional triple-quantum methods. However, in later years the initial excitement surrounding higher-order MQMAS experiments began to diminish as more experiments were completed.

Numerous investigations have since been completed to compare the associated advantages and disadvantages of higher-order MQMAS experiments and, as a result, there is now a better understanding that many factors need to be considered when deciding which order of multiple-quantum MAS NMR experiment to utilise. Pike[185] and co-workers concluded that multiple-quantum experiments should have inherently higher resolution if the linewidth is due to relaxation, i.e., could be termed 'homogeneous'. The gain in resolution obtained using higher-order MQMAS was found to reduce when the linewidth was 'inhomogeneous'. For example, when there is a distribution of chemical shifts no significant gain in resolution will be observed as this scales with coherence order. Any gain in resolution observed when using higher-order MAS experiments is therefore dependent on the origin of the linewidth. The relative sensitivities of the various MQMAS experiments are widely known to strongly depend on both the quadrupolar coupling constants and strength of the radiofrequency fields used. Therefore, when comparing any two higher-order MQMAS experiments, for example three- and five-quantum, both resolution and sensitivity need to be considered. The spectrum obtained may be of higher resolution using a five-quantum experiment; however it will, typically, be up to five or six times less sensitive than the three-quantum experiment. In past years there has been the development of techniques to try improve the sensitivity of such multiple-quantum experiments, for example the introduction of FAM and SPAM experiments.[186-190] However, in reality, unless there is the necessity for a considerable improvement in resolution it is considered 'convention' to utilise triple-quantum MAS NMR experiments.

2.9.4 Extraction of NMR parameters

It is possible to extract NMR parameters from conventional MAS NMR spectra by computer fitting of the lineshape. One method by which this can be completed is by using the Solids Line Shapes Analysis (SOLA) fitting program (or equivalent) in Topspin 2.1. To demonstrate how this

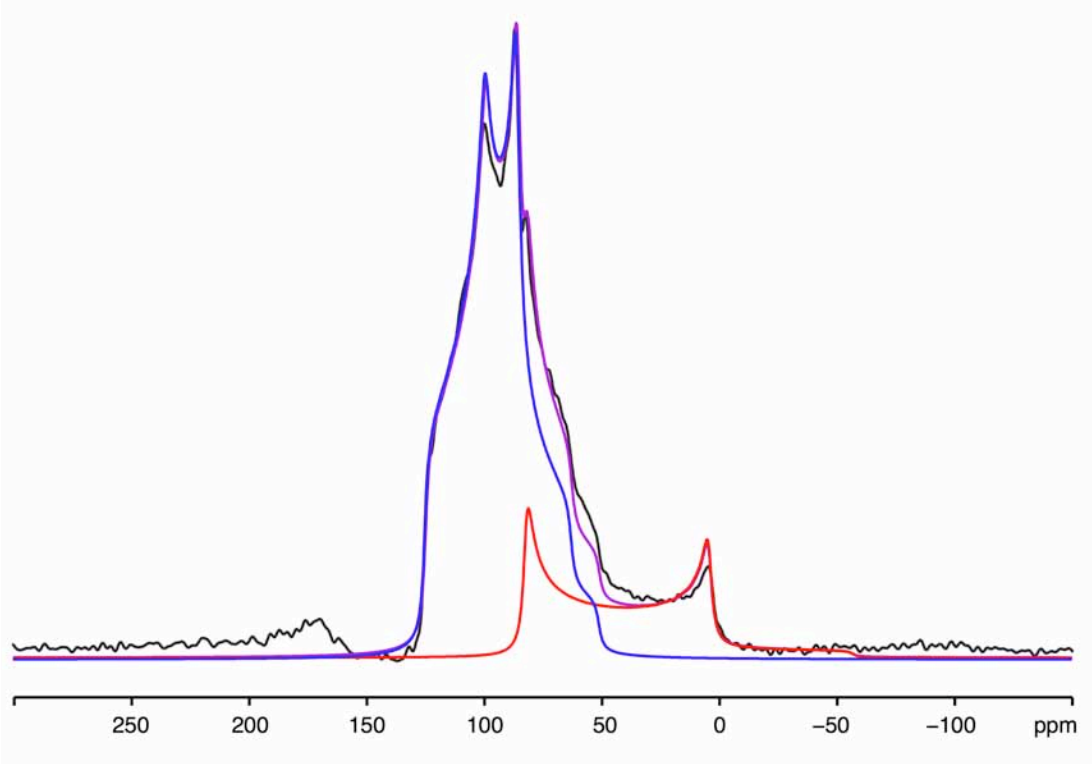

Figure 2.31: Analytical fitting of the ^{45}Sc (14.1 T) MAS NMR spectrum of Sc_2O_3. The experimental spectrum is shown in black, fitted lineshapes for the Sc1 and Sc2 sites are shown by the red and blue lines, respectively, with the summation of the two shown in purple. The spectrum is the result of averaging 512 transients with a recycle interval of 3 s. The MAS rate was 60 kHz. Details of the parameters obtained are given in Table 2.3.

can be achieved a ^{45}Sc (14.1 T) MAS NMR spectrum recorded for Sc_2O_3 has been fitted using SOLA and is shown in Figure 2.31. Sc_2O_3 possesses two crystallographically distinct Sc sites. In Figure 2.31 the experimental spectrum is shown in black with the fitted lineshapes for the Sc1 and Sc2 sites denoted by the red and blue lines respectively. The sum of the two sites is shown in purple. It was possible to extract values for δ_{iso}, C_Q and η_Q for each site. The extracted parameters obtained were in good agreement with the literature and are given in Table 2.3.[191] Whilst this is easy for simple spectra it becomes impractical as the number of sites increases and high-resolution approaches are required.

MQMAS spectra contain a series of ridge lineshapes, each of which corresponds to a different crystallographically-distinct species. Using MQMAS, it is possible to extract information regarding both the

Table 2.3: Experimental ^{45}Sc NMR parameters δ_{iso}, C_Q, η_Q and P_Q for Sc_2O_3 obtained from the MAS spectrum in Figure 2.31.

Site	δ_{iso} (ppm)	P_Q / MHz	C_Q / MHz	η_Q
Sc1	105.8(5)	23.3(1)	23.3(1)	0.0(1)
Sc2	126.6(5)	16.3(1)	15.4(1)	0.6(1)

quadrupolar and chemical shift interactions from spectra. This can be completed in a variety of ways, the most common of which being to obtain the position of the centre of gravity of the ridge lineshape (δ_1, δ_2). This then enables determination of the isotropic chemical shift, δ_{iso}, and the quadrupolar product, P_Q, a combination of the quadrupolar coupling constant, C_Q, and asymmetry, η_Q, given by[192]

$$P_Q = C_Q(1 + \eta_Q^2/3)^{1/2} \quad . \tag{2.57}$$

Alternatively, the parameters δ_{iso}, C_Q and η_Q may be obtained directly by computer fitting of an extracted cross-section along the experimental ridge, parallel to δ_2. However, it must be noted the lineshape obtained in this case can be distorted as a result of non-uniform excitation and conversion of triple-quantum coherences.

To illustrate one method of extracting NMR parameters from an MQMAS spectrum the aluminophosphate AlPO-14 has been used as an example. The aluminophosphates (AlPOs) are an important class of microporous materials with numerous applications in areas such as separation and catalysis. Organic templates, commonly amines or quaternary ammonium salts, are also added during the hydrothermal synthesis of such framework materials. The template molecules are essential in producing the microporous frameworks adopted by aluminophosphates as they are incorporated into the cavities within the structure. Post-synthetic removal of the template can be achieved by conventional calcination methods. Calcined AlPO-14 contains four crystallographically distinct Al sites and the structure is shown in Figure 2.32. ^{27}Al (I = 5/2) is a quadrupolar nucleus and commonly displays

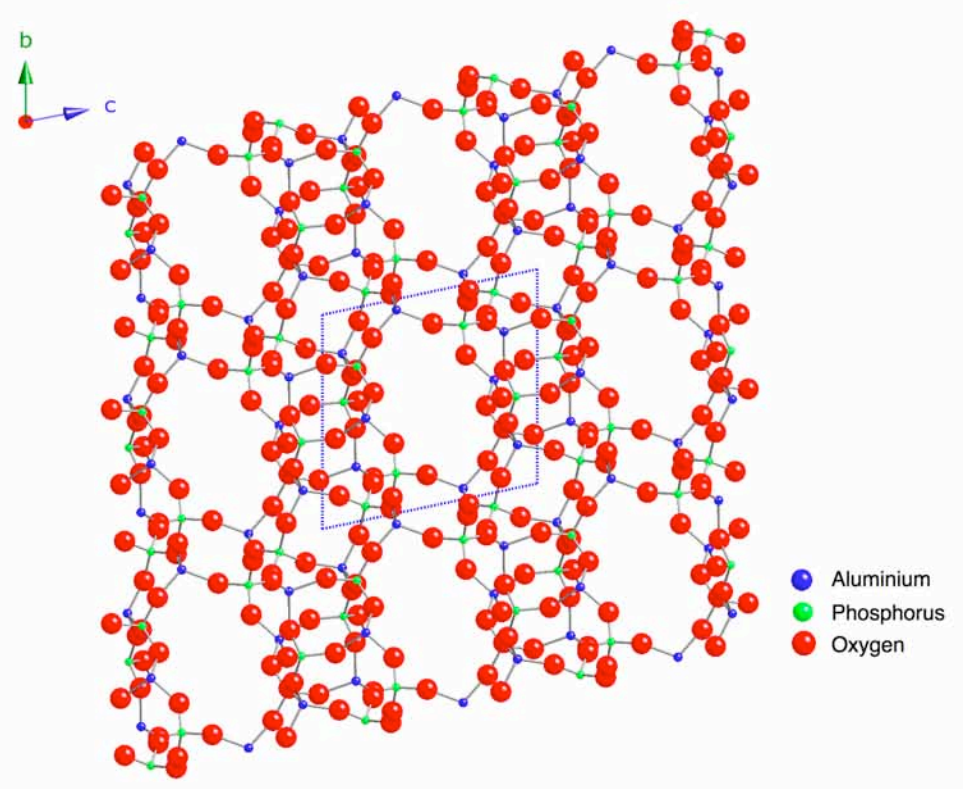

Figure 2.32: Crystal structure of calcined AlPO-14 viewed along the a axis.

broadening as a result of the incomplete removal of second-order quadrupolar interactions. Hence, MQMAS techniques are routinely utilised for materials containing this nucleus. The triple-quantum ^{27}Al MAS NMR spectrum of calcined AlPO-14 is shown in Figure 2.33 and clearly displays four distinct resonances, in good agreement with the literature.[194,195] To determine parameters for each site a cross-section was extracted from each ridge and analysed using SOLA. It was possible to fit each lineshape and obtain values for δ_{iso}, C_Q and η_Q, for each site, all of which are given in Table 2.4. Extracted lineshapes and subsequent fits are also shown in Figure 2.33. It must be noted that it is not always possible to determine quadrupolar parameters for all sites in any two-dimensional spectrum owing to severe line broadening and/or distortion, commonly caused either by non-uniform triple-quantum excitation or possible disorder within the compound. Furthermore, it is often challenging to accurately distinguish between any overlapped sites. In such cases it is often more convenient to quote P_Q values derived from the position of the centre of gravity.

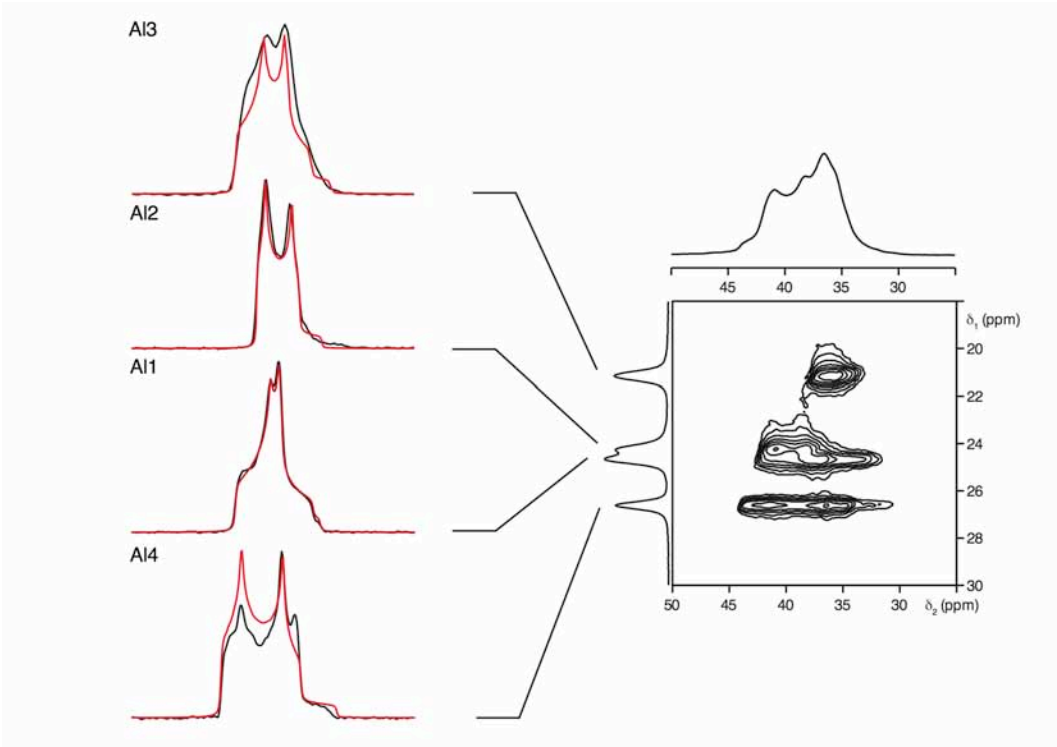

Figure 2.33: Conventional ^{27}Al (14.1 T) MAS NMR spectrum, triple-quantum MAS NMR spectrum, and corresponding isotropic projection. The spectrum was recorded using the phase-modulated split-t_1 shifted echo pulse sequence shown in Figure 2.30 and is the result of averaging 768 transients with a recycle interval of 0.5 s for each of the 256 increments of 129.16 μs. A additional SPAM (soft-pulse added mixing) pulse was added to gain a signal enhancement. The MAS rate was 10 kHz. Also shown (in black) are lineshapes obtained by taking cross sections along ridges parallel to δ_2 corresponding to each site. Each lineshape was subsequently fitted using SOLA, and the fits obtained are also shown in red. The parameters obtained are given in Table 2.4.

2.9.5 MQMAS and Disorder

Disordered materials are a common occurrence throughout solid-state chemistry. Within this particular investigation a variety of perovskite structures have been studied and, like many other materials, they are widely known to exhibit disorder across both the A and B sites. As previously discussed in Chapter 1, there are various synthetic methods that can be utilised to try and promote ordering across these sites.

Table 2.4: Experimental ^{27}Al NMR parameters δ_{iso}, C_Q, η_Q and P_Q for calcined AlPO-14, obtained from the MQMAS spectra in Figure 2.33.

Site	δ_{iso} (ppm)	P_Q / MHz	C_Q / MHz	η_Q
Al1	42.2(5)	4.4(1)	3.9(1)	0.8(1)
Al2	42.5(5)	3.5(1)	3.5(1)	0.2(1)
Al3	37.6(5)	2.7(1)	2.6(1)	0.5(1)
Al4	45.1(5)	5.0(1)	5.0(1)	0.3(1)

However, this is not always successful and, more commonly, a disordered structure will result.

The lineshapes observed for quadrupolar nuclei are commonly broad owing to large quadrupolar interactions. The presence of disorder can produce a substantial effect on the lineshape observed. Therefore, the addition of disorder into any quadrupolar system makes the application of solid-state NMR more challenging. In many quadrupolar spectra the presence of disorder is immediately apparent owing to the observation of 'classic' disordered MAS lineshapes, in which an asymmetric broadening of the central transition is observed with a characteristic 'tail' to lower frequencies. Shown in Figure 2.34 are three different lineshapes which display many of the characteristic features commonly observed in MAS NMR spectra. Figure 2.34(a) displays a quadrupolar lineshape and is representative of a well-ordered crystalline solid. In contrast, Figure 2.34(b) exhibits a broadened lineshape with an asymmetric tail to low frequency. This commonly indicates the presence of a distribution of the quadrupolar interaction. In Figure 2.34(c) a classic 'disordered' lineshape is shown, with no obvious or distinct features. Lineshapes of this type are commonly indicative of a distribution of both quadrupole and chemical shifts. Owing to their broad and often featureless nature it can be difficult to determine the full extent of the disorder exhibited. Therefore, to gain further insight high-resolution two-dimensional techniques such as MQMAS are required. Disorder can result either from a distribution of chemical shifts or a distribution of quadrupolar shifts. However, more commonly, disorder is caused by a combination of the two. The size and shape of the resulting ridge lineshape, in addition to the direction along

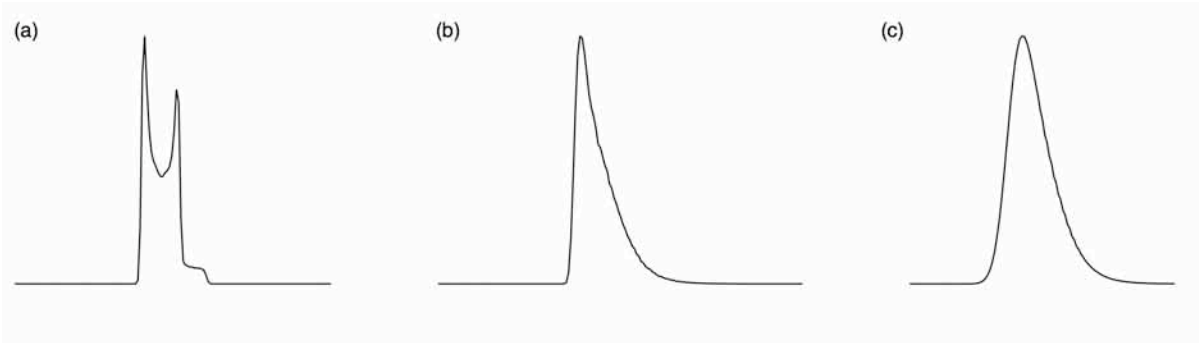

Figure 2.34: Simulated I = 5/2 MAS lineshapes (a) single lineshape with C_Q = 3 MHz, η = 0 and δ_{CS} = 0 ppm, (b) includes a Gaussian distribution of C_Q with a half width at half-height of 0.75 MHz and (c) includes uncorrelated Gaussian distributions of both C_Q (as in (b)) and δ_{CS} (with a half-width at half-height of 2 ppm). All simulations have $\omega_0/2\pi$ = 104.3 MHz.

which each is broadened in any MQMAS spectrum, is highly informative as to the nature of any disorder exhibited. Consider a spin I = 3/2 nucleus, if a single sharp ridge is displayed and aligned along a gradient of −7/9 (the MQMAS ratio, R) no distribution of parameters is present. Hence, the system is well-ordered. However, if the ridge is broadened along a gradient of +3 this is indicative of a distribution of chemical shift environments, $dist_{CS}$. When the ridge is broadened along the ratio $A^0(I,3/2)/A^0(I,1/2)$ this indicates a distribution of quadrupolar contributions, $dist_Q$ is present. Specific values for both $dist_{CS}$ and $dist_Q$ are tabulated in Table 2.5 for half-integer nuclei. When a distribution of both chemical and quadrupolar shifts is exhibited the length and shape of the ridge is altered. Shearing a spectrum also changes the direction along which the ridge is aligned. All values in Table 2.5 are prior to shearing, values post shearing can be found in Appendix I.

To illustrate how different MQMAS spectra of ordered and disordered materials can be, ^{27}Al MQMAS NMR spectra have been recorded and compared for two Al-bearing compounds. Aluminium acetylacetonate, $Al(acac)_3$, is one example of a well ordered material. The ^{27}Al MAS NMR spectrum of $Al(acac)_3$, shown in Figure 2.35(a), displays a single resonance, indicative of a single site. Similarly, the ^{27}Al two-dimensional multiple-quantum MAS NMR spectrum, recorded using a z-

Table 2.5: Values for distribution of chemical shift and quadrupolar shifts for half-integer nuclei.

I	m_I	R	$dist_{CS}$	$dist_Q$
$I = 3/2$	$1/2$			
	$3/2$	$-7/9$	3	-3
$I = 5/2$	$1/2$			
	$3/2$	$19/12$	3	$3/4$
	$5/2$	$-25/12$	5	$-25/4$
$I = 7/2$	$1/2$			
	$3/2$	$101/45$	3	$9/5$
	$5/2$	$11/9$	5	-1
	$7/2$	$-161/45$	7	$-49/5$
$I = 9/2$	$1/2$			
	$3/2$	$91/36$	3	$9/4$
	$5/2$	$95/36$	5	$5/4$
	$7/2$	$7/18$	7	$-7/2$
	$9/2$	$-31/6$	9	$-27/2$

filtered pulse sequence, displays a single narrow ridge aligned along the MQMAS ratio 19/12, thereby confirming there to be no distribution of parameters and hence no disorder (Figure 2.36(a)). In contrast, γ-alumina, γ-Al_2O_3, is a well known example of a disordered material. The ^{27}Al MAS NMR spectrum, shown in Figure 2.35, displays two broad resonances, corresponding to 4 and 6 coordinate Al sites respectively. Both sites display 'disordered' lineshapes with 'tails' to low frequency. The ^{27}Al two-dimensional multiple-quantum MAS NMR spectrum of the 6 coordinate resonance, recorded using a z-filtered pulse sequence, is shown in Figure 2.36(b) and displays a single broad resonance which is suggestive of a distribution of both chemical and quadrupolar shifts. Also shown for completeness in Figure 2.36(c) and (d) are sheared two-dimensional spectra for $Al(acac)_3$ and γ-Al_2O_3 respectively. An extracted cross-section from the $Al(acac)_3$ spectrum in Figure 2.36(a) was fitted using SOLA and the corresponding NMR parameters can be found in Table 2.6. Average chemical shift, $\langle\delta_{iso}\rangle$, and quadrupolar product, $\langle P_Q\rangle$, values

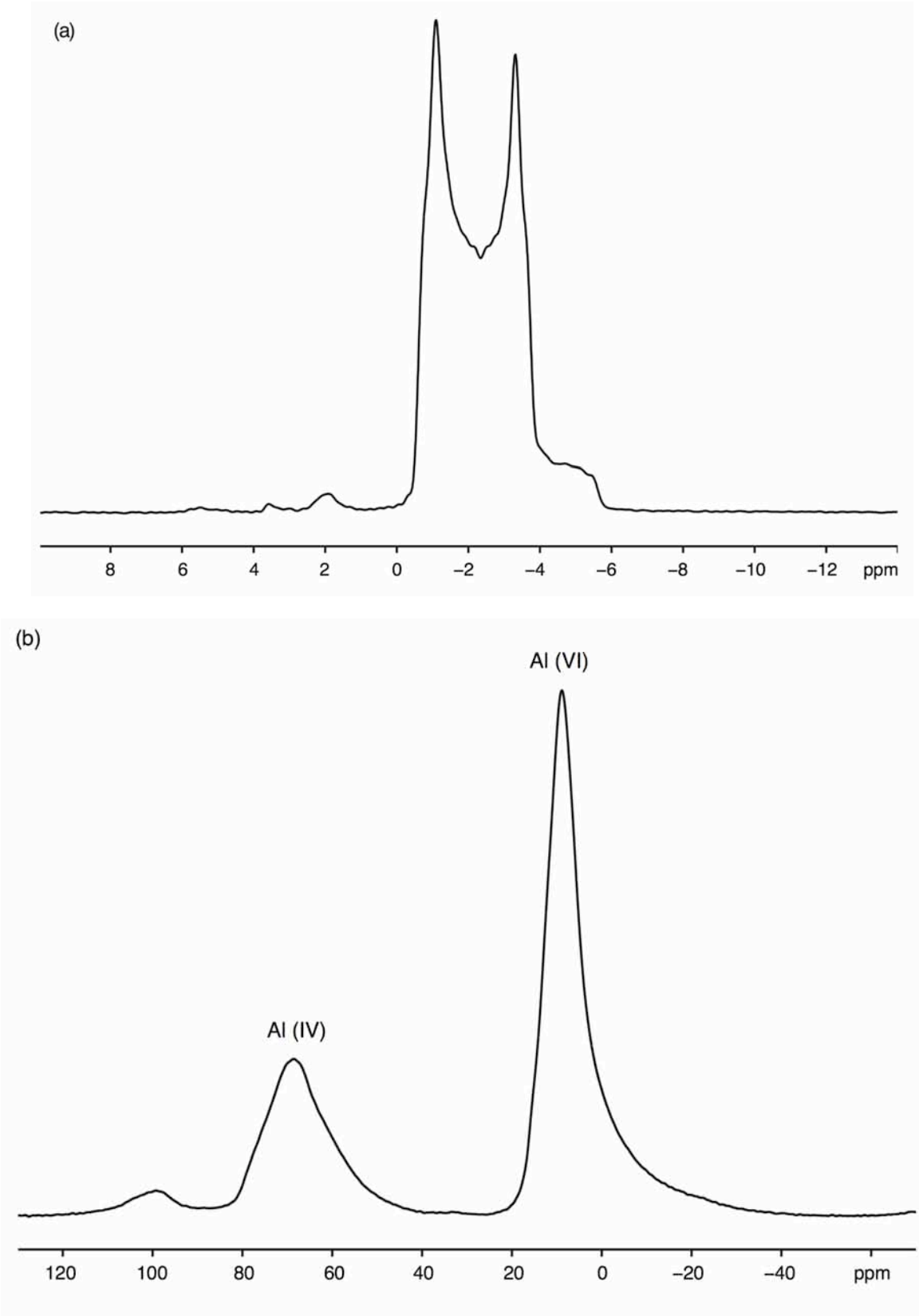

Figure 2.35: Conventional ^{27}Al MAS (14.1 T) NMR spectra for (a) $Al(acac)_3$ and (b) γ-Al_2O_3. Spectra are the result of averaging (a) 64 and (b) 96 transients with a recycle interval of 2 s. The MAS rate was 14 kHz.

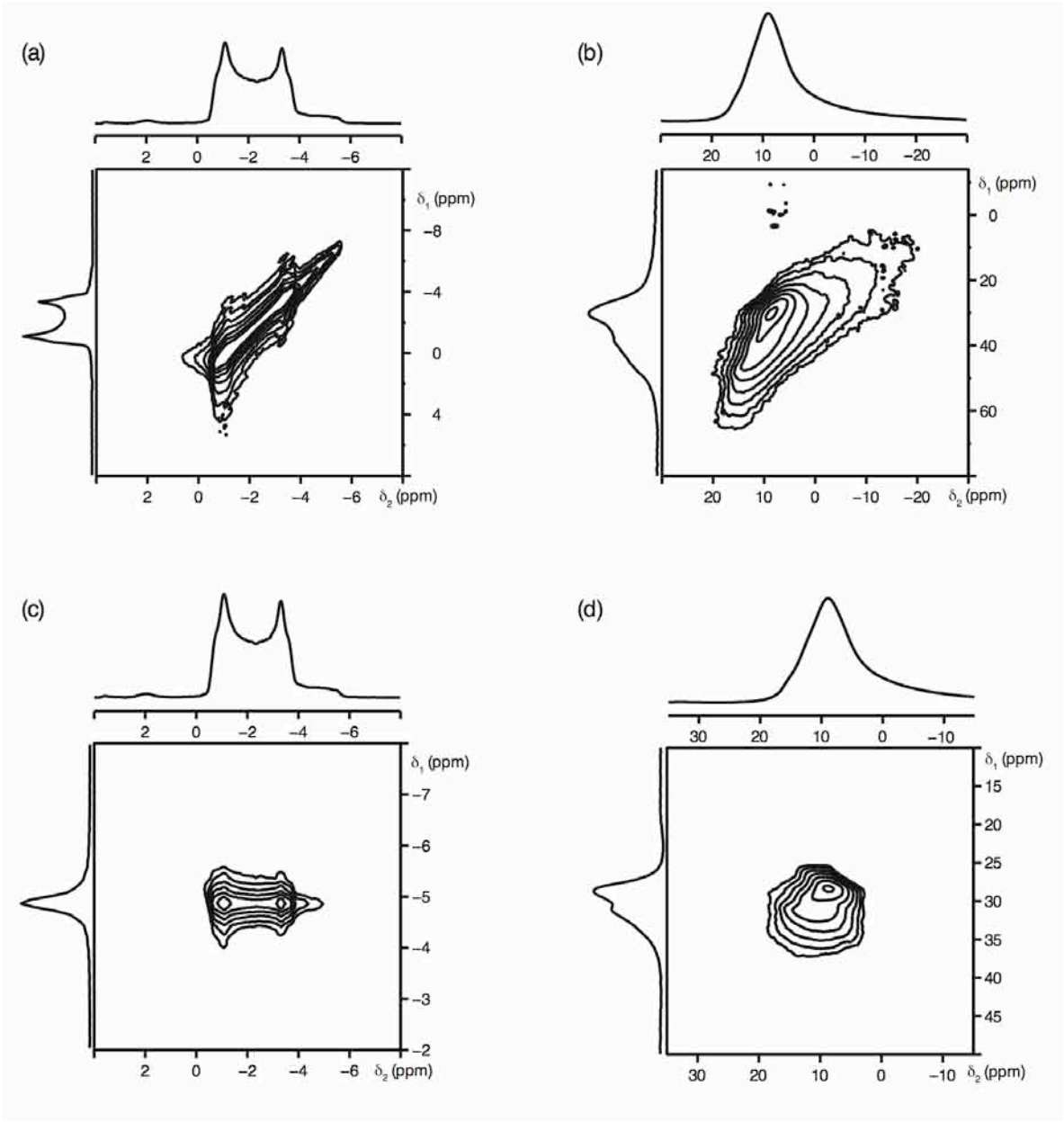

Figure 2.36: Conventional ^{27}Al (14.1 T) MAS NMR spectra and triple-quantum MAS NMR spectra for (a, c) $Al(acac)_3$ and (b, d) γ-Al_2O_3. The spectra in (a) and (b) were recorded using the z-filtered pulse sequence shown in Figure 2.29 and are the result of averaging 96 transients with a recycle interval of 3 s for each of the (a) 768 and (b) 256 increments of 33.3 μs. The MAS rate was 14 kHz. The ^{27}Al MQMAS spectra and corresponding isotropic projections shown in (c) and (d) are post shearing.

Table 2.6: Experimental ^{27}Al NMR parameters δ_{iso}, C_Q, η_Q and P_Q for Al(acac)$_3$ obtained from the MAS spectrum in Figure 2.35.

Site	δ_{iso} (ppm)	P_Q / MHz	C_Q / MHz	η_Q
Al1	−0.09(5)	3.0(2)	3.0(2)	0.2(1)

Table 2.7: Experimental ^{27}Al NMR parameters $\langle\delta_{iso}\rangle$ and $\langle P_Q\rangle$ C_Q, η_Q and P_Q for γ-Al_2O_3 obtained from the position of the centre of gravity in the MQMAS spectrum in Figure 2.36.

Site	$\langle\delta_{iso}\rangle$ (ppm)	$\langle P_Q\rangle$ / MHz
Al1	−0.09(5)	3.0(2)

obtained for γ-Al_2O_3 from the position of the centre of gravity in the MQMAS spectrum shown in Figure 2.36(b) can be found in Table 2.7. MQMAS NMR spectra can therefore be successfully utilised to gain additional insight into the precise nature of any disorder exhibited in a particular system. Furthermore, when used in conjunction with other structural characterisation techniques such as high-resolution powder diffraction it will aid considerably in both the structural understanding and characterisation of the system under investigation.

2.10 Density Functional Theory (DFT) Calculations

2.10.1 Introduction

The use and practical implementation of first-principles calculations within solid-state chemistry has accelerated in recent years owing to major advancements and modifications of computational codes. Within this particular study first-principles or, more specifically, density functional theory (DFT) calculations have been utilised to calculate NMR parameters, such as the isotropic chemical shift, δ_{iso}, and quadrupolar parameters C_Q and η_Q. DFT methods provide a relatively easy way to

monitor the variation of NMR parameters with changes to local coordination environment and, when used in conjunction with high-resolution NMR data, they provide key assistance in spectral understanding, assignment and interpretation. In addition, DFT calculations aid in linking NMR and diffraction directly as the crystal structures initially used in DFT calculations are commonly obtained from X-ray or neutron diffraction.

In recent years the use of *ab initio* or first-principles calculations has become increasingly important in the field of nuclear magnetic resonance. Parameters obtained by calculation can support those obtained experimentally, where lineshapes may be broadened or distorted as a result of practical imperfections. Furthermore, DFT methods can often provide important additional information regarding anisotropy and tensor orientations, parameters which are often not easy to extract from experiments, particularly under MAS. In some cases the prediction of parameters by calculation can guide experiment and spectral acquisition. For example, a calculation may predict a system to possess a very large CSA or C_Q which cannot, feasibly, be observed experimentally or may require a different practical approach. DFT calculations can also provide insight into the more complex properties of solids, for example disorder or dynamics by comparing experimental data to that calculated for model structures or systems. In general, DFT methods provide a flexible way of studying the dependence of NMR parameters upon structure and local coordination. In turn, they also provide a simple way in which to test various structural models for materials with unknown structures against experimental observables. It must be noted that whilst a full description of DFT is beyond the scope of this thesis some of the methodologies relevant to the calculation of NMR parameters will be discussed in the following sections.

2.10.2 First-Principles Calculations

In principle the energy and properties of a system can be predicted by solving the relevant Schrödinger equation.[196] However, this cannot be

solved exactly for systems with more than one electron, and for larger systems approximations must be made. Consider a single particle that may exist in two quantum mechanical states, 0 and 1, with contributions described by coefficients a and b. The total wavefunction, ψ, can be described by

$$\Psi = (a|0\rangle + b|1\rangle) \quad . \tag{2.58}$$

If this approach is then extended to three particles, each of which may exist in two states, it is entirely plausible to believe ψ may be given by

$$\Psi = (a|0\rangle + b|1\rangle)(c|0\rangle + d|1\rangle)(e|0\rangle + f|1\rangle). \tag{2.59}$$

This expression is, however, incorrect as this approach does not consider the effect of the interactions between the particles. The wavefunction, therefore, needs to be described in terms of all possible combinations of the two states. Hence, the expression for ψ becomes considerably more complex and is given by

$$\Psi = a|000\rangle + b|001\rangle + c|100\rangle + d|010\rangle + e|110\rangle + f|011\rangle + g|101\rangle + h|111\rangle \ , \tag{2.60}$$

where there are contributions from 8 coefficients (a-h) as opposed to 6 in the previous expression. If we then consider *n* particles which can exist in *m* states the number of coefficients required to describe the wavefunction increases as m^n. Whilst for small systems such calculations may appear feasible, for larger molecules or systems this quickly becomes intractable owing to the complexity of the quantum mechanical expression required to describe the total wavefunction. In such cases several approximations need to be made to simplify the problem.

2.10.3 Solving the Schrödinger Equation

To calculate the properties of a system it is necessary to solve the many-particle time-dependent Schrödinger equation, given by

$$-i\hbar\frac{\partial\Psi}{\partial t} = \hat{H}\Psi \quad , \tag{2.61}$$

where the Hamiltonian $\hat{H}$ describes the various electrostatic interactions between particles and is expressed as

$$\hat{H} = \hat{T}_{e,n} + \hat{V}_{e-e} + \hat{V}_{e-n} + \hat{V}_{n-n} \quad , \tag{2.62}$$

where $\hat{T}_{e,n}$ is the kinetic energy between the electrons (e) and nuclei (n) in the system and $\hat{V}$ is the potential energy between the electrons and nuclei in the system. *Ab initio* methods such as Hartree-Fock[197-200] include all terms in the Hamiltonian as far as possible which, in turn, becomes computationally demanding and costly. This method is therefore favoured by small molecular systems where there are fewer atoms. Semi empirical methods, however, use parameters or approximations that compensate for neglecting the more computationally complex terms in the calculation. These parameters are commonly derived either from experiment or *ab initio* calculations completed on model systems. Semi empirical methods can therefore be used for much larger systems. However, it must be noted that such techniques are not always transferable.

2.10.4 The Born-Oppenheimer Approximation

The Born-Oppenheimer approximation[201] exploits the difference in mass between the electrons and the nucleus. Compared to electrons, nuclei are massive and slow. This has two consequences; whenever a nucleus moves, the electrons react so quickly that it may as well be instant, and the wavefunctions for nuclei are zero except in a very small region, hence they contribute only a very small potential. Therefore, only the

effect from the electrons needs to be considered and since they react instantaneously to any change in the position of the nuclei this removes the time dependency of the Schrödinger equation given by

$$\hat{H}\Psi = E\Psi \tag{2.63}$$

where

$$\hat{H} = \hat{T}_e + \hat{V}_{e-e} + \hat{V}_{e-n} \quad . \tag{2.64}$$

The Hamiltonian now depends solely on the quantum mechanics of the electrons. The expression is, however, still relatively complex with two unknown variables; the kinetic energy of the electron, $\hat{T}_e$, and the potential energy between electrons, $\hat{V}_{e-e}$.

2.10.5 Density Functional Theory (DFT)

An alternative approach to this problem was presented in the mid 1960s. Two papers by Hohenberg and Kohn[202] and Kohn and Sham[203] showed that the ground state energy and charge density of interacting electrons in any external potential were equivalent to those of non-interacting electrons in a specially modified potential. Hence, the total ground state energy of the system may be written solely in terms of a functional of the electron density using the Hohenberg-Kohn equation, given by

$$E[\rho] = E_{KE}[\rho] + E_{e-e}[\rho] \tag{2.65}$$

$$E[\rho] = E_{KE}^{non-int}[\rho] + E_{e-e}^{non-int}[\rho] + E_{xc}[\rho] \quad , \tag{2.66}$$

where $E_{KE}^{non-int}[\rho]$ and $E_{e-e}^{non-int}[\rho]$ are the kinetic and potential energy of a system of non-interacting electrons respectively. The extra term in this equation, $E_{xc}[\rho]$, is a functional of the electron density $\rho(r)$ and is called the exchange-correlation functional. This accounts for the quantum mechanical energy not described by the first two terms. The exact form of this term is unknown, but can contribute up to ~10% of the total energy.

To accurately determine its contribution physically motivated approximations need to be made. The simplest and most commonly used approximation is the local density approximation, LDA,[204,205] given by

$$E_{xc}[\rho] = \int \varepsilon_{xc}(\rho)\rho(r)d^3r \ , \qquad (2.67)$$

which uses the local value of the electron density to determine $E_{xc}[\rho]$. It calculates the exchange-correlation density at a given point from that of a uniform electron gas with the same electron density. This approximation is based on a first-principles approach and is routinely used for solid-state systems. LDA works surprisingly well, however, it is widely known to encounter problems regarding the energetics of systems. It has subsequently been shown that for many systems the addition of terms dependent upon the gradient of the density can provide an improvement. This is known as the generalized gradient approximation, GGA,[206,207] and is given by

$$E_{xc}[\rho] = \int \varepsilon_{xc}(\rho, \nabla\rho)\rho(r)d^3r \ . \qquad (2.68)$$

In contrast to LDA, this approximation is routinely used for chemical applications. There are a number of possible methods by which this can be achieved, for example in solid-state NMR calculations the GGA proposed by Perdew, Burke and Ernzerhof (PBE)[208] is routinely used and has been shown to be extremely useful.

2.10.6 Planewaves and Pseudopotentials

Wavefunctions, Ψ, are usually expanded in terms of a linear combination of basis set functions, given by

$$\Psi = \sum_j c_j \psi_j . \qquad (2.69)$$

For molecules the extent of the system is well defined and the atomic or molecular orbitals provide a good basis set. Solids, however, are large

extended systems therefore a suitable method is required to accurately calculate such structures. Traditional computational methods typically use cluster approximations to calculate extended systems. Using this method an 'infinite' solid is approximated around a central atom, and any dangling bonds are appropriately terminated, typically using hydrogen bonds. The size, shape and long-range electrostatics of the cluster are dependent upon the precise position of the termination. Conventionally, atom-based orbitals are the basis set used in cluster approximations. The accuracy of any cluster calculation is therefore dependent upon the size and type of basis set used and the precise point of termination. To obtain accurate results large cluster sizes are typically required which are, computationally, expensive and demanding, and often require large computational resources.

In reality, solids such as zeolites, polymers and glasses are large extended periodic systems and atomic orbitals do not usually provide an adequate basis set. Therefore, a basis set is required that exploits the inherent periodicity of a solid. Bloch's theorem states that if the nuclei are arranged in a periodically repeating pattern their potential acting on the electrons must also be periodic. In addition, the density and the wavefunction, or more specifically its magnitude, must also be periodic. The translational symmetry of solids may therefore be exploited computationally. Three-dimensional periodic boundary conditions can be imposed using the unit cell, enabling long-range effects to be reproduced. Unlike cluster approximations, there are no 'termination' problems when using this method. One basis set which exploits the periodicity of the wavefunctions is planewaves.[209] They form a mathematically simple basis whilst naturally incorporating periodic boundary conditions. Planewave calculations can be taken systematically to convergence as a function of the size of the basis set. There are, however, an infinite number of possible planewaves with increasing energy, and so a cut-off energy, E_{cut}, needs to be defined which results only in planewaves with energy less than this to be included. All calculations must be 'converged' with respect to E_{cut}, i.e., this parameter should be increased until the answer no longer changes within the specified tolerance range. Wavefunctions which

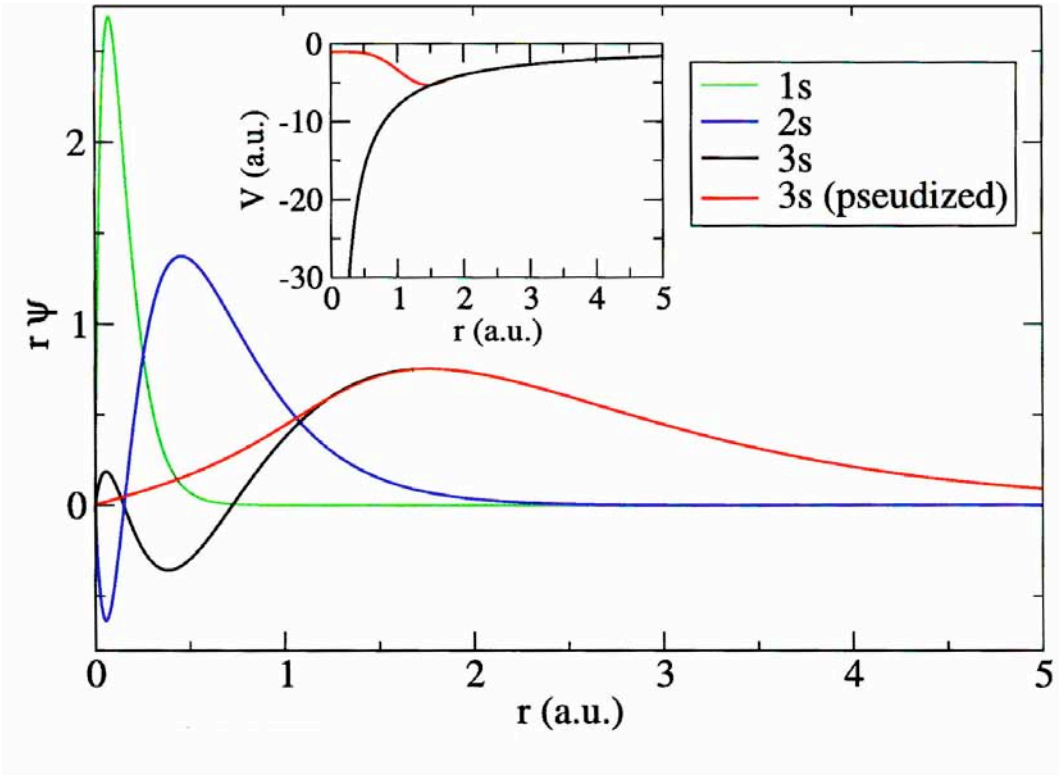

Figure 2.37: Pseudized (red line) and all electron (black line) wavefunction for the 3s valence state of silicon. The two are in good agreement beyond the core radius r_c.

rapidly oscillate require many planewaves to accurately describe them and hence higher cut-off energies.

The use of planewaves is highly advantageous, however, there are some associated technical difficulties. For example, the explicit representation of core and valence electrons near to the nucleus would require too many planewaves. Therefore to ensure the efficiency of all calculations when using planewaves two major approximations must be made; (1) the frozen core approximation and (2) the pseudopotential approximation. The electrons in an atom can be divided broadly into two types, core and valence. The core electrons are tightly bound to the nucleus and are, in turn, not directly involved in bonding, hence they play no part in the interactions between atoms. The core electrons simply provide a shielding or screening of the nuclear charge effect. The frozen core approximation ensures the core electrons are constrained not to differ from their free atomic nature when placed in the molecular or solid-state environment. This approximation reduces the number of electronic degrees of freedom in an all-electron calculation. The pseudopotential

approximation is a different but physically relevant approximation.[210,211] Once the frozen core approximation has been used the valence electron wavefunctions can oscillate rapidly close to the nucleus, thereby requiring many planewaves. Pseudopotentials allow a simplification of the wavefunctions close to the nucleus. The nodal structure of the all-electron wavefunction is replaced by a node-less smooth pseudo wavefunction within the 'core radius', r_c, of the nucleus, as illustrated in Figure 2.37. The pseudo wavefunctions are then used to calculate the resulting pseudopotentials for each atom, each of which is then used in subsequent calculations.

Almost all physical properties depend on the region outside r_c. For core region properties the simplified core region description does not provide accurate results, therefore a true all-electron description of the core region is necessary. This can be achieved using the projector augmented wave (PAW) method, developed by van de Walle and Blöchl.[212] This approach uses the pseudopotential description of the core region and from this the all-electron observables are reconstructed, thereby enabling accurate calculation of the NMR parameters. One major advantage of this method is its ability to compute large systems with high accuracy and low computational cost. The PAW method is, however, not applicable to studying solid systems in a uniform magnetic field. A modification to this method is therefore required. The introduction of an external magnetic field induces a current from both the core and valence electrons and to calculate parameters such as the chemical shift in the presence of a magnetic field this current needs to be accurately calculated. The contribution to the current from the core electrons can be calculated relatively easily. The contribution from the valence electrons, however, is more challenging to calculate as these electrons are described using pseudo wavefunctions in a region close to the nucleus. To accurately calculate the all-electron current in this region an augmentation of the pseudo wavefunction is required. One method for doing this is the Gauge Including Projector Augmented Wave[213] (GIPAW) formalism. This introduces gauge invariance to the PAW method in order to preserve

translational invariance in the magnetic field. This, in turn, enables accurate calculation of chemical shieldings.

2.11 CASTEP

The CASTEP[214-216] code uses first-principles quantum mechanical methods, namely density functional theory, for electronic structure calculations. CASTEP is a planewave DFT code which exploits the inherent periodicity of many solids and enables accurate calculation of NMR parameters from the shielding, quadrupolar and scalar coupling tensors.

2.11.1 Convergence Studies

Once the pseudopotenial has been decided the accuracy of any CASTEP calculation depends on an optimal set of computational parameters, namely the cut-off energy, E_{cut}, of the planewave and the k-point spacing. To accurately determine these optimised values a series of convergence tests are required for individual systems. To do this several calculations must be undertaken with one of the variables fixed whilst the effect on the calculated NMR parameters of varying the other is investigated. These parameters converge to a specific value (within a specified tolerance range) and the point at which convergence is achieved indicates the optimal value for that particular variable. This sequence is then repeated for the other variable. Once completed the optimal cut-off energy and k-point spacing can be used to accurately calculate the NMR parameters for the system of interest. It must be noted that as the specified tolerance limit is increased the answer will become more accurate, however, this accuracy comes at a greater computational cost. Therefore, the exact tolerance used is a compromise between the level of accuracy required and the computational resources available.

Convergence studies were undertaken for the various systems discussed in this work. Detailed below are the convergence tests completed for the Pbcm phase of sodium niobate, $NaNbO_3$.[217] The k-point

spacing in initial tests was fixed at 0.1 $Å^{-1}$. Calculations were then completed using cut-off energies of 30, 40, 50, 60 and 70 Ry respectively. The variation of the isotropic shielding, σ_{iso}, quadrupolar coupling constant, C_Q and asymmetry, η_Q, with cut-off energy for Na1, Na2 and Nb are shown in Figures 2.38, 2.39 and 2.40 respectively. All parameters monitored displayed convergence by 50 Ry, as highlighted in Figures 2.38, 2.39 and 2.40. To ensure complete convergence E_{cut} was fixed at 60 Ry and a series of similar calculations were undertaken to optimise the k-point spacing, testing 0.03, 0.04 and 0.05 $Å^{-1}$ respectively. In a similar manner the variation of σ_{iso}, C_Q and η_Q with k-point spacing were plotted, and convergence occurred at a k-point spacing of k = 0.04 $Å^{-1}$, as shown in Figures 2.41, 2.42 and 2.43. Thus, the optimum k-point spacing and cut-off energy for $NaNbO_3$ were 0.04 $Å^{-1}$ and 60 Ry respectively. All subsequent calculations used these parameters.

2.11.2 Structural Optimisation

DFT calculations are a convenient way of directly linking diffraction and NMR. However, a common problem with such calculations is the quality of the initial crystallographic data used to describe the unit cell. Calculations completed using structures obtained directly from X-ray and neutron powder diffraction commonly possess very high energies and large atomic forces on each atom in the unit cell. In contrast, calculations completed using structures obtained from single crystal diffraction data usually possess very low atomic forces. The high energies and large atomic forces exhibited by many of the structures calculated from powder diffraction data therefore suggest that each structure is not in a local energy minimum and geometry optimisation is required. This process 'relaxes' the structure to a true local minimum by minimising the forces on each of the atoms in the unit cell. During geometry optimisation the energy of the electrons for fixed atomic positions is minimised, the atomic forces are evaluated and the atoms are moved in the direction indicated most favourable by the forces. This process is repeated until the force on each atom is below a specified

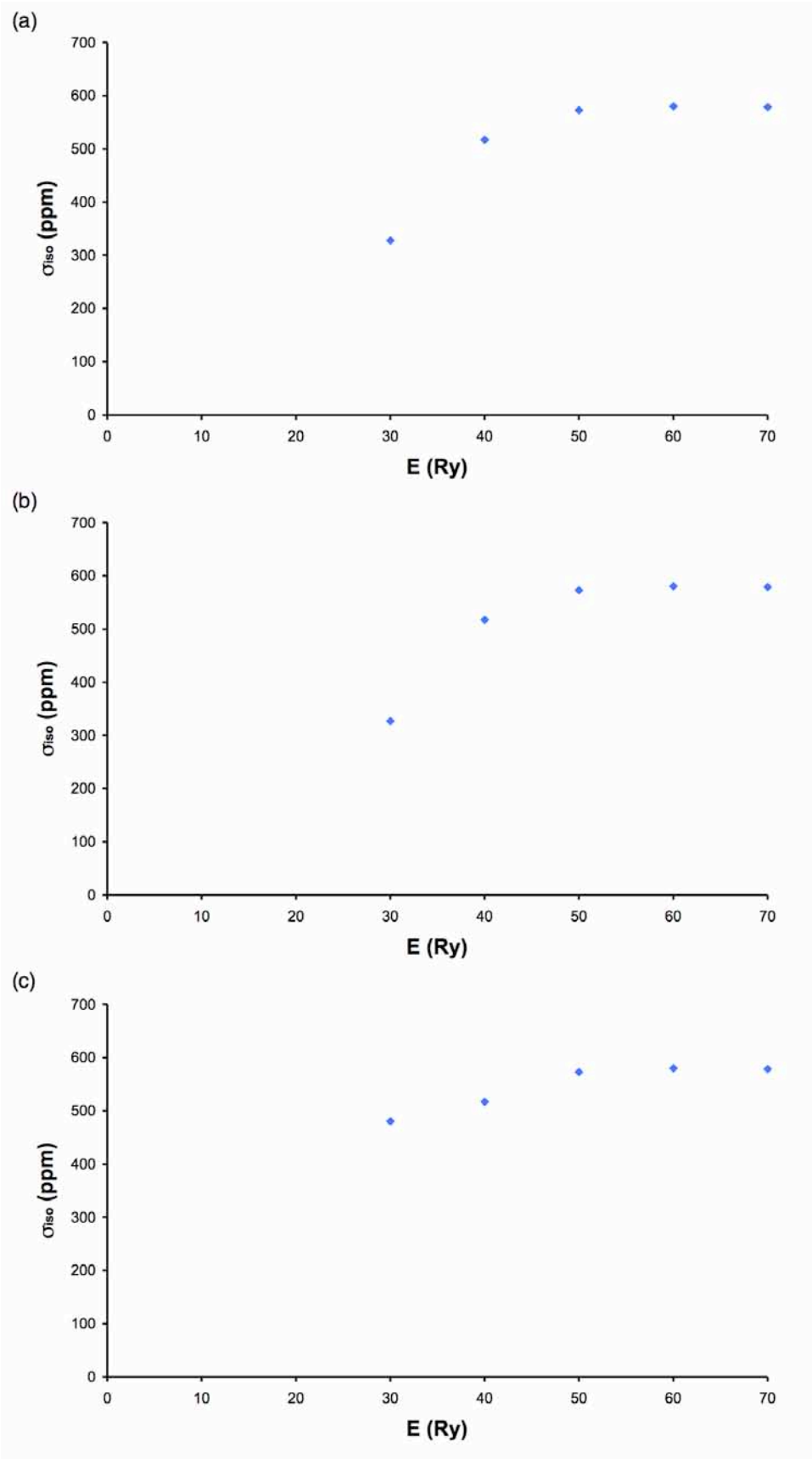

Figure 2.38: Variation of the isotropic shielding, σ_{iso}, with cut-off energy for (a) Na1, (b) Na2 and (c) Nb in $NaNbO_3$.

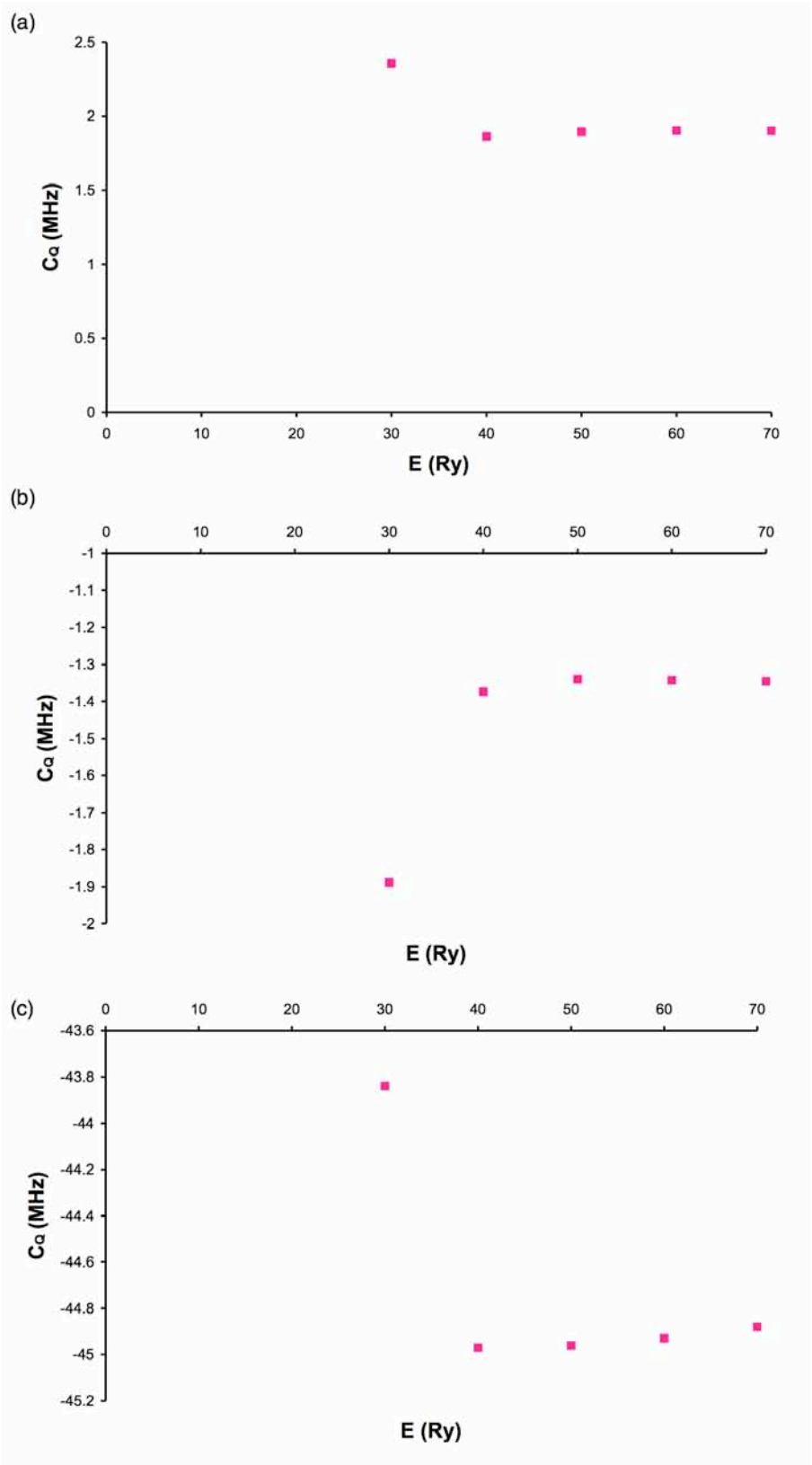

Figure 2.39: Variation of the quadrupolar coupling constant, C_Q, with cut-off energy for (a) Na1, (b) Na2 and (c) Nb in $NaNbO_3$.

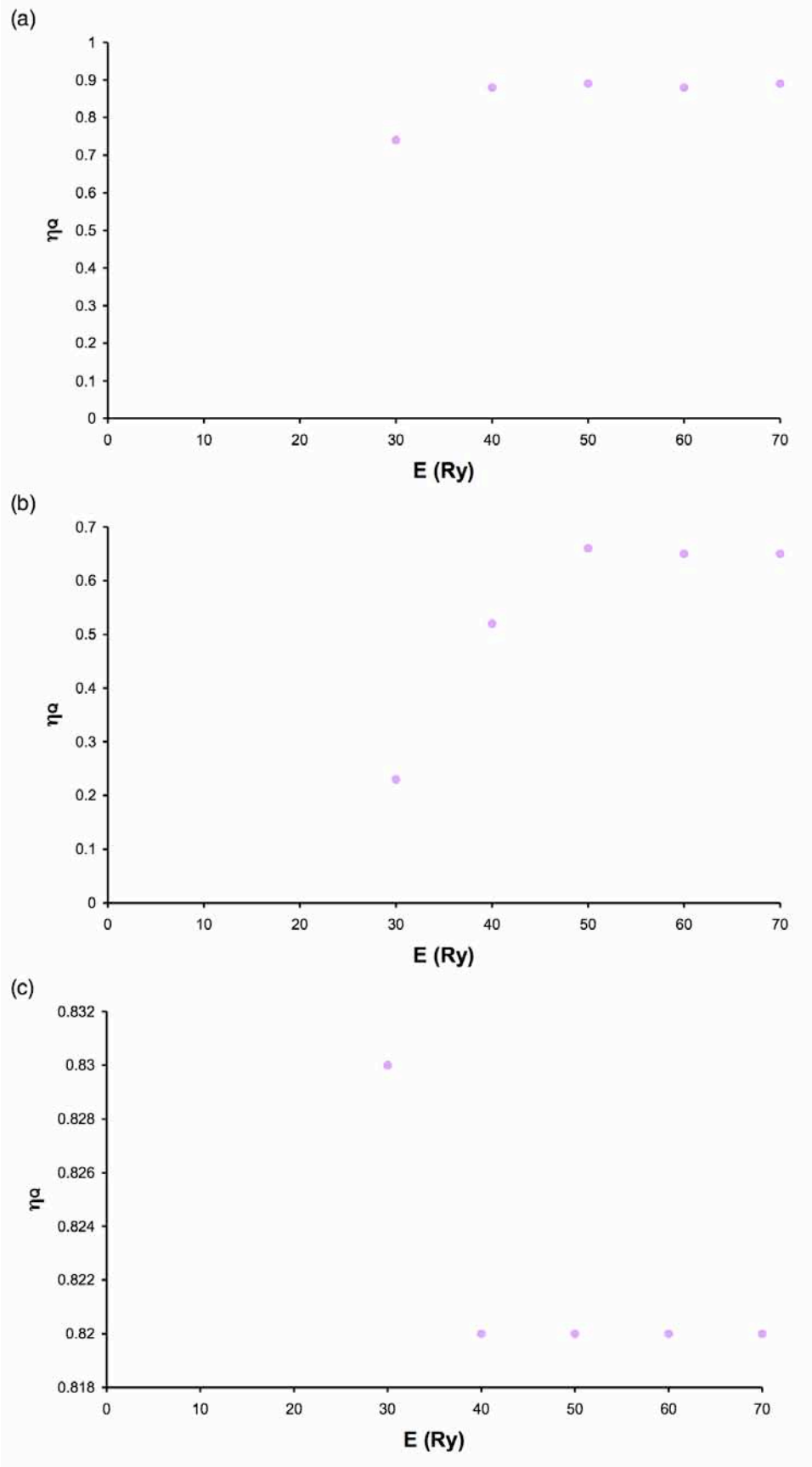

Figure 2.40: Variation of the asymmetry, η_Q, with cut-off energy for (a) Na1, (b) Na2 and (c) Nb in $NaNbO_3$.

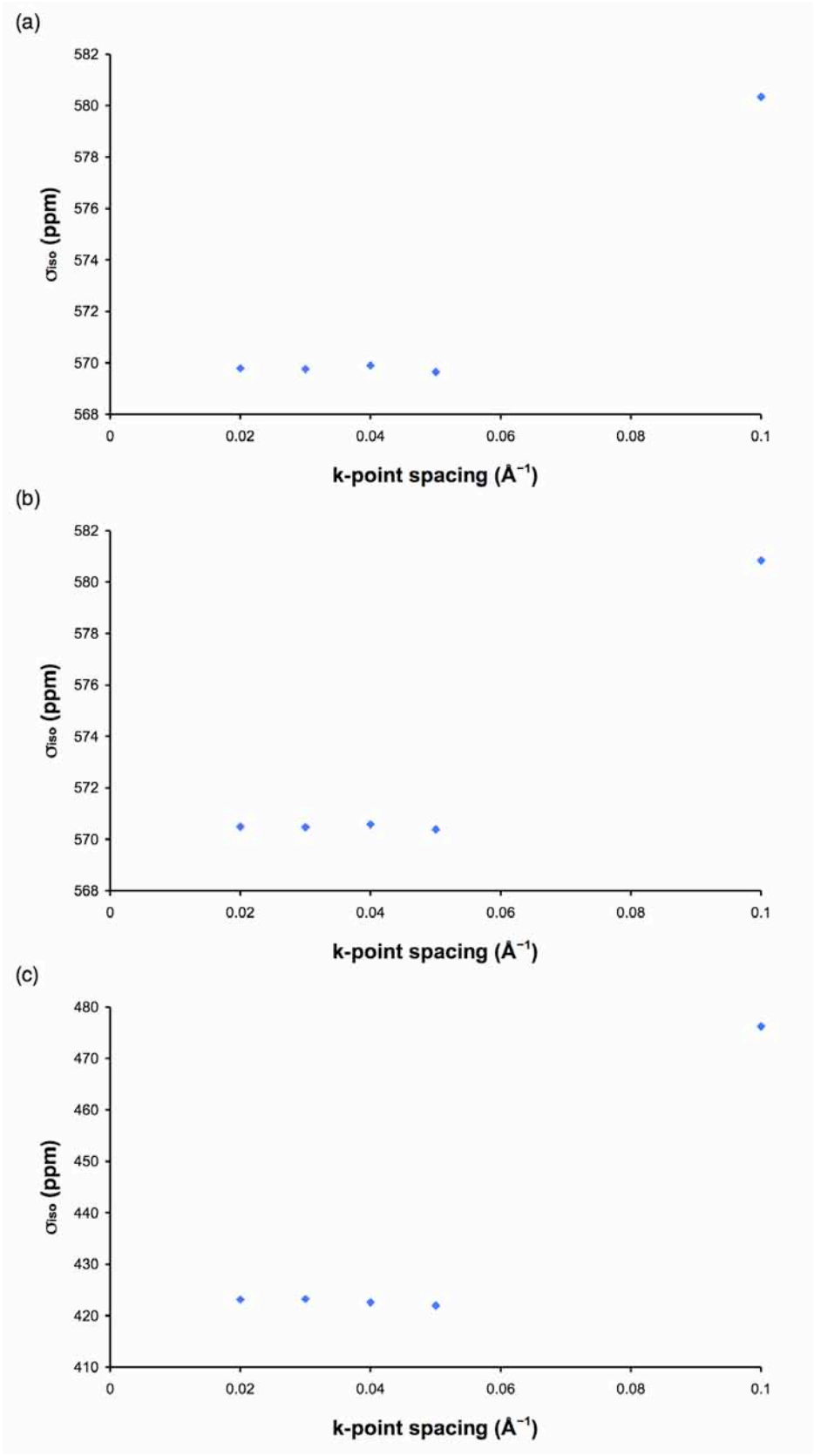

Figure 2.41: Variation of the isotropic shielding, σ_{iso}, with k-point spacing for (a) Na1, (b) Na2 and (c) Nb in $NaNbO_3$.

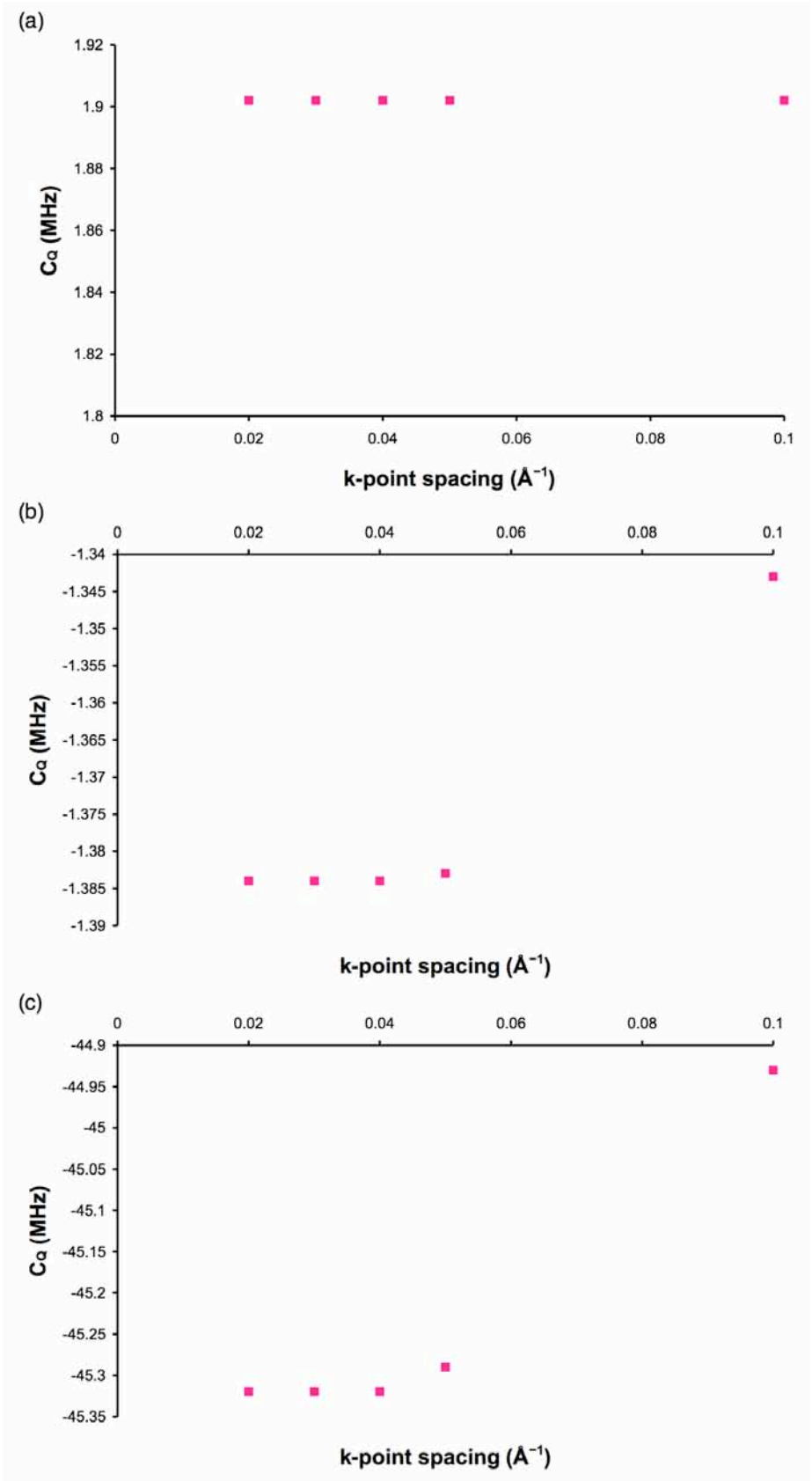

Figure 2.42: Variation of the quadrupolar coupling constant, C_Q, with k-point spacing for (a) Na1, (b) Na2 and (c) Nb in $NaNbO_3$.

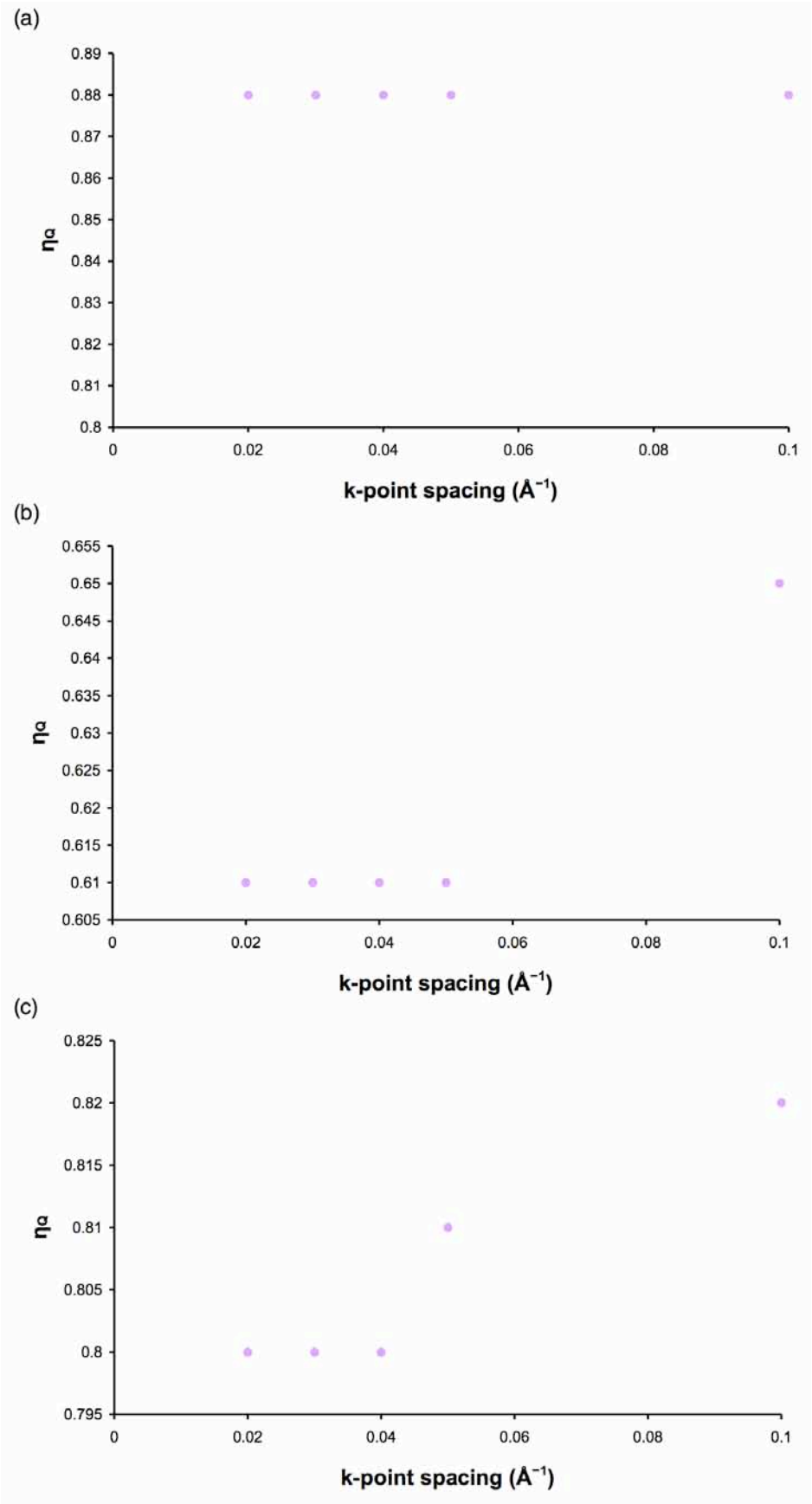

Figure 2.43: Variation of the asymmetry, η_Q, with k-point spacing for (a) Na1, (b) Na2 and (c) Nb in $NaNbO_3$.

tolerance. This then enables the closest local minimum to be found. However, it must be noted that this may not be the global minimum. The structure obtained with the lowest forces is then utilised in subsequent NMR calculations to determine the associated NMR parameters. During a geometry optimisation calculation it is possible to constrain the unit cell parameters (a, b, c, α, β, γ) and allow solely the atomic coordinates to vary. Alternatively all constraints can be removed, enabling both the unit cell and atomic coordinates to vary simultaneously.

Geometry optimisation is an extremely useful method for obtaining the lowest energy structure. However, there is an important issue regarding the accuracy of the structure obtained post optimisation. For example, GGA[206,207] is widely known to overestimate the lattice parameters of a structure during any geometry optimisation whilst LDA[204,205] is known to underestimate the lattice parameters. Therefore, it may be argued that the fully optimised structure is no longer an accurate representation of the initial structure obtained from diffraction. The changes made to the fractional coordinates and/or unit cell are often extremely small, except for atoms that are not initially placed by diffraction, for example protons in microporous materials. NMR parameters are often sensitive to small changes in local structure, hence optimisation is often necessary. There are many associated advantages for relaxing structures prior to calculation of the NMR parameters. For example, within this particular study the greatest degree of correlation between experiment and DFT calculations was generally observed after allowing both the unit cell and atomic coordinates to vary simultaneously. DFT calculations were completed for several different perovskite structures and interestingly, the NMR parameters (δ_{iso}, C_Q and η_Q) calculated for each were found to vary quite considerably depending on whether the structure had been geometry optimised. During any structural optimisation very small adjustments are made to the unit cell and/or atomic coordinates. To highlight how subtle these changes usually are consider the geometry optimisation of $LaScO_3$, an orthorhombic perovskite in space group Pbnm.[218] It must be noted that during optimisation of the structure only the La and O positions are optimised, as the Sc sites are crystallographically fixed on a special

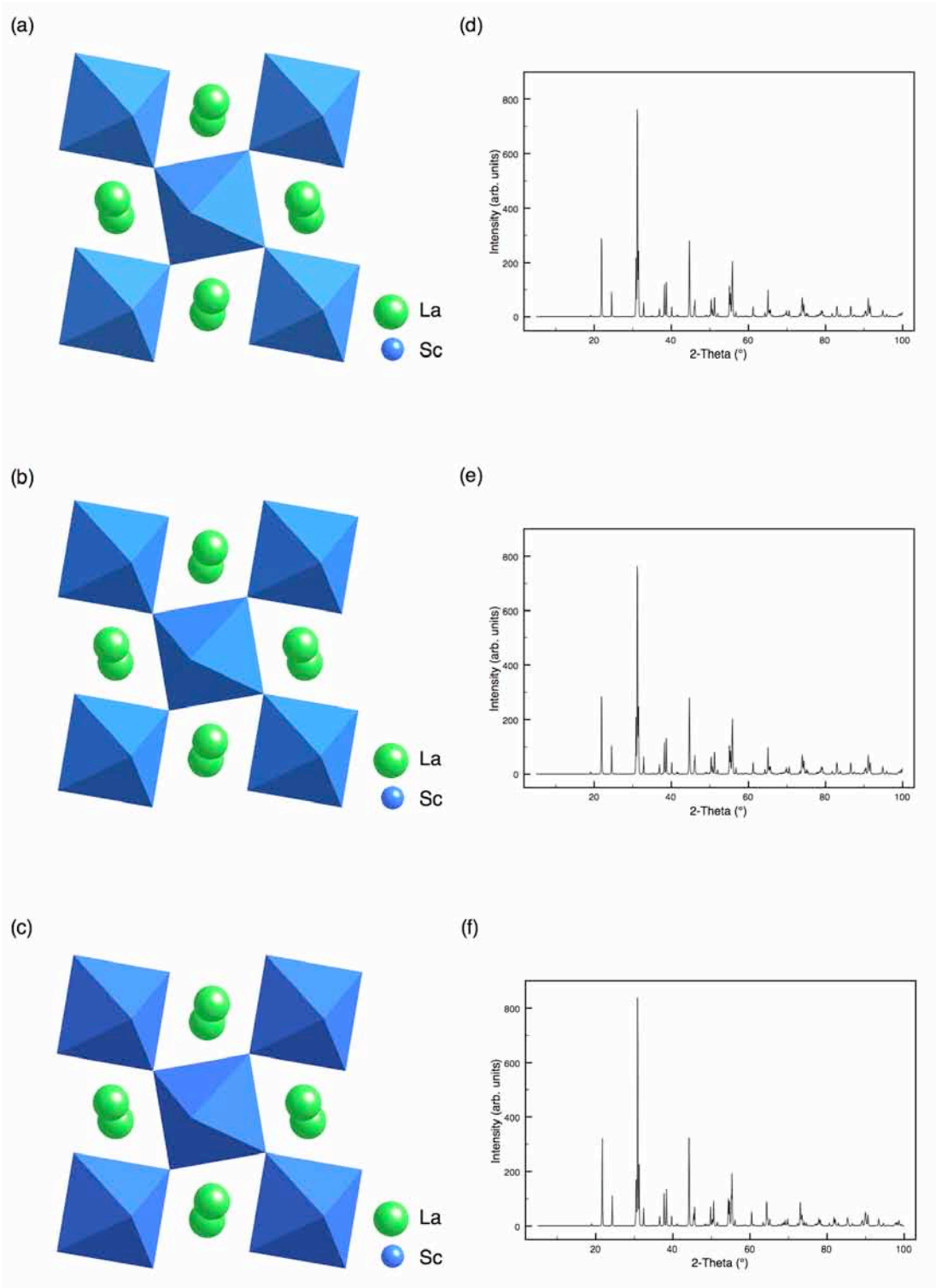

Figure 2.44: The crystal structure of $LaScO_3$ (a) prior to geometry optimisation, (b) post geometry optimisation allowing solely the atomic coordinates to vary, keeping the unit cell fixed and (c) post geometry optimisation allowing both the atomic coordinates and unit cell to vary simultaneously. Also shown in (d-f) are simulated X-ray diffraction patterns for the non-optimised and optimised structures.

Table 2.8: Experimental and calculated (using CASTEP) ^{45}Sc NMR parameters, δ_{iso}, P_Q, C_Q and η_Q, for $LaScO_3$. (a) Experimental parameters for $LaScO_3$ (see Chapter 6), calculated parameters obtained (b) using a structure obtained directly from the literature,[218] (c) post optimisation (fixed unit cell) and (d) post optimisation, allowing both the unit cell and atomic coordinates to vary simultaneously.

	Site	δ_{iso} (ppm)	P_Q / MHz	C_Q / MHz	η_Q
$LaScO_3^{(a)}$	Sc	162.0	4.00	3.90	0.30
$LaScO_3^{(b)}$	Sc	160.9	6.49	5.89	0.80
$LaScO_3^{(c)}$	Sc	161.8	2.80	2.54	0.81
$LaScO_3^{(d)}$	Sc	162.0	3.26	3.05	0.66

position and cannot move. Shown in Figure 2.44(a) is the non-optimised $LaScO_3$ structure (obtained from the literature)[218] and two geometry optimised structures, Figure 2.44(b) and (c), obtained from calculation by (1) fixing the unit cell and enabling solely the atomic coordinates to vary and (2) allowing both the unit cell and atomic coordinates to vary simultaneously. Structurally, all three appear virtually identical; however, the positions of the La and O atoms have been changed in the two optimised structures. (Details of all fractional coordinates prior to and post optimisation can be found in Appendix I). Also shown in Figure 2.44(d-f) are simulated diffraction patterns for each structure. When compared the three patterns appear identical, indicating structural optimisation produces very little effect on the diffraction pattern. The subtle change in atomic position of each atom does, however, produce an associated effect on the calculated NMR parameters. For example, prior optimisation a C_Q = 5.9 MHz was predicted for Sc, however, after optimising both the unit cell and atomic coordinates a considerably smaller value was obtained (C_Q = 3.0 MHz). These differences highlight a very important point regarding structural optimisation. Minor adjustments to both the unit cell and fractional coordinates can produce a

substantial change to the local environment of any nucleus and in such cases parameters sensitive to very local changes, such as C_Q and η_Q, often exhibit large differences in their calculated values. Full details of all NMR parameters calculated for $LaScO_3$, both prior to and post optimisation of the structure, can be found in Table 2.8. Also shown for comparison are the ^{45}Sc (I = 7/2) experimental NMR parameters obtained for $LaScO_3$.

2.11.3 Computational Methods

All calculations were completed using the CASTEP[214] density functional theory code, a planewave pseudopotential method that utilises the gauge-including projector augmented wave (GIPAW) formalism. The CASTEP code enables accurate calculation of quadrupolar and shielding interactions for NMR active nuclei. Calculations used the generalised gradient approximation (GGA) PBE functional with ultrasoft pesudopotentials[219] and periodic boundary conditions, and typical values of the k-point spacing and cut-off energy were 0.04 $Å^{-1}$ and 60 Ry respectively. Calculations were converged as far as possible with respect to the cut-off energy and k-point spacing, as described above.

Crystal structures were obtained from both the Inorganic Crystal Structure Database[140] and Rietveld refinement of high-resolution neutron diffraction experimental data. Where necessary, geometry optimisation of the structure was performed, enabling both the unit cell and atomic positions to vary. Fully optimised structures were then used to calculate NMR parameters. Calculations generate the absolute shielding tensor, $\boldsymbol{\sigma}$, and electric field gradient (EFG) tensor, $\mathbf{V}$, in the crystal frame. From these the isotropic chemical shift, δ_{iso}, is given by

$$\delta_{iso} = -(\sigma_{iso} - \sigma_{ref}) \ , \qquad (2.)$$

where σ_{iso}, the isotropic shielding, is (1/3) Tr{$\boldsymbol{\sigma}$} and σ_{ref} is a shielding reference determined experimentally. The shielding reference is obtained by setting the calculated isotropic chemical shift equal to that determined experimentally. The magnitude (C_Q) and asymmetry (η_Q) of the

quadrupolar interaction can be generated from the principal components of the EFG tensor (V_{xx}, V_{yy}, V_{zz}) through $C_Q = eQV_{zz}/h$ and $\eta_Q = (V_{xx} - V_{yy})/V_{zz}$. It must be noted that experimentally it is often difficult to determine the sign of C_Q, however, this information is automatically generated by calculation. The signs of all calculated values of C_Q are included in the DFT data presented within this thesis.

Chapter 3

The Polar Phase of $NaNbO_3$: A Combined Study

3.1 Introduction

Sodium niobate, $NaNbO_3$, is a perovskite of significant interest at present owing to recent reports of exceptional piezoelectric responses in $NaNbO_3$-derived ceramics such as the solid-solution $K_xNa_{1-x}NbO_3$ (KNN); these properties have the potential to make KNN-based ceramics a viable lead-free alternative to the most widely used piezoelectric material $Pb(Zr_xTi_{1-x})O_3$ (PZT).[25,26] In recent years research on the KNN system has accelerated, with studies concentrated, in particular, around the x = 0.5 region of the phase diagram at the suggested Morphotropic Phase Boundary (MPB), where the highest piezoelectric responses were initially located. Ultimately, however, to fully understand this system each end-member in the solid-solution requires complete structural characterisation. Whilst the crystal structure of the room temperature form of $KNbO_3$ is widely accepted as orthorhombic, in space group Amm2,[220] with a = 3.971 Å, b = 5.697 Å and c = 5.723 Å, the various polymorphs of $NaNbO_3$ are still a subject of significant discussion. $NaNbO_3$ possesses an extremely complex phase diagram containing a series of complicated and poorly understood phase transitions as a function of temperature.[217,220-224] In more recent work, the existence of several new room temperature polymorph(s) of $NaNbO_3$ has been suggested.[225,226] In the light of these recent findings, in addition to the existing ambiguities regarding the various $NaNbO_3$ polymorphs,[222] the present work concentrates on the synthetic chemistry and structural characterisation of the room temperature polymorphs of $NaNbO_3$.

Published crystallographic data indicates that the most commonly reported room temperature phase of $NaNbO_3$ has an orthorhombic unit cell, space group Pbcm, with a = 5.506 Å, b = 5.566 Å and c = 15.520 Å (Figure 3.1(a)). This phase, first characterised by Sakowski-Cowley *et al.*,[217]

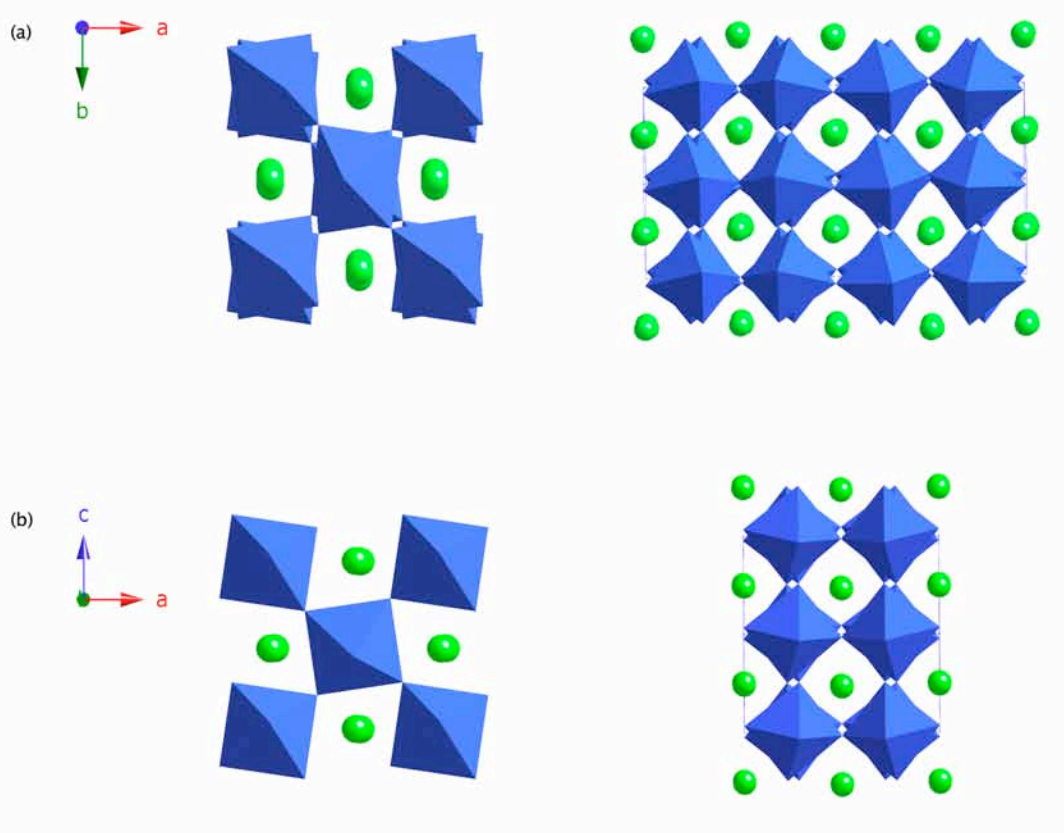

Figure 3.1: Crystal structures reported for the polymorphs (a) Pbcm and (b) $P2_1ma$ of $NaNbO_3$. Green spheres represent the sodium atoms, and the NbO_6 octahedra are shown as enclosed units (blue). Crystallographic data are taken from the literature.[217,228]

displays an unusual 'octahedral tilting' scheme with three independent tilts leading to a $\sqrt{2}a_p \times \sqrt{2}a_p \times 4a_p$ supercell of the basic cubic perovskite subcell, where a_p is the idealised cubic perovskite lattice parameter ~3.9 Å.[227] This structure possesses two crystallographically distinct Na sites. However, on the basis of peak broadenings observed using high-resolution neutron powder diffraction, Darlington and Knight suggest this phase is actually monoclinic, with $\gamma = 89.94°$.[222] Despite such structural confusion $NaNbO_3$ is well documented as being antiferroelectric at room temperature and, as a result of work presented by Shuvaeva *et al.*, it is known to undergo an electric field induced phase transition to a ferroelectric phase, in the polar space group $P2_1ma$, with unit cell dimensions a = 5.569 Å, b = 7.790 Å and c = 5.518 Å.[228] In contrast to the Pbcm polymorph, the $P2_1ma$ polymorph exhibits a simpler octahedral tilt system leading to a smaller unit cell described by $\sqrt{2}a_p \times \sqrt{2}a_p \times 2a_p$, as

shown in Figure 3.1(b). This phase results from the polarisation of single crystals of $NaNbO_3$.

Amongst the various structural studies undertaken on polycrystalline samples, submicron powders and single crystals of $NaNbO_3$, Waser and co-workers[226,227] have suggested, based on X-ray powder diffraction and Raman spectroscopy, that samples of $NaNbO_3$ reveal a number of structural phase transitions as a function of particle size. One of the most interesting proposals is that $NaNbO_3$ crystallises in the polar (and hence potentially ferroelectric) space group $Pmc2_1$ (alternative setting $P2_1ma$) at submicron particle sizes. This phase apparently corresponds to the 'field-induced' phase of Shuvaeva.[228] Many of the ambiguities in determining the exact nature of the various $NaNbO_3$ polymorphs arise from the subtleties in the different octahedral tilting schemes well-known in perovskites. Octahedral tilting is an intrinsic property of perovskites and is a direct consequence of the relative sizes and nature of the A- and B-site cations. As previously discussed in Chapter 1 section 1.3, Glazer developed a convenient notation to describe the most commonly encountered tilt systems.[16,20] Owing to the ambiguities regarding the correct structural models for the various polymorphs of $NaNbO_3$ a variety of Glazer systems have been proposed. Subtle changes of this nature can be extremely difficult to detect using diffraction methods alone, and for this reason techniques that probe short-range order are highly beneficial as they enable local changes in the cation environments, particularly the A-sites, to be monitored closely. Moreover, given the confusion and apparent complexity surrounding the proposed ambient temperature polymorphs of $NaNbO_3$ it is essential to employ a variety of complementary techniques in order to establish their nature and how their occurrence depends on synthetic variables, particle size, temperature and other intrinsic and extrinsic effects.

Here we present a comprehensive structural study of $NaNbO_3$ at room temperature using a variety of complementary techniques, including high-resolution X-ray (PXRD) and neutron powder diffraction (NPD), high-resolution solid-state ^{23}Na and ^{93}Nb magic-angle spinning (MAS) NMR, density functional theory (DFT) calculations, scanning electron

microscopy (SEM) and second harmonic generation (SHG) measurements. Previous studies of $NaNbO_3$ have often focused primarily on the use of PXRD and NPD as methods for structural characterisation. In contrast, there have been relatively few investigations using solid-state NMR,[230,231] the most detailed of which was by Ashbrook *et al*.[231] There has been a growing interest in the use of DFT calculations to aid assignment and interpretation of NMR spectra, that has accelerated in recent years owing to the advancement and modification of computational codes. In particular, the introduction of codes which exploit the inherent periodicity and translational symmetry of solids has made them an integral addition to the solid-state NMR community, and a variety of applications investigating structure, order and dynamics in a range of materials have been demonstrated.[232-239] Calculations provide a relatively easy way to monitor the variation of the NMR parameters with changes to local coordination environment, providing key assistance in the structural characterisation of many solids, in this case $NaNbO_3$. In an effort to gain an understanding of the relationship between structure and synthetic route a variety of different synthesis methods have also been heavily investigated. Within this chapter conventional solid-state synthetic techniques[240,241] are compared with molten salt[242] and sol-gel[243] approaches and significant differences are observed in the relative phases formed, as well as in both crystallinity and crystal morphology, thereby implying synthesis route heavily influences both crystal structure and microstructure.

3.2 Experimental

3.2.1 Synthesis

A sample of $NaNbO_3$ was purchased from Sigma-Aldrich (99.9%) and used without further purification. All other $NaNbO_3$ samples were synthesised using conventional solid-state, molten salt and sol-gel methods. Using a solid-state approach stoichiometric amounts of purchased Na_2CO_3 (Fisher Scientific, 99.5%) and Nb_2O_5 (Sigma-Aldrich, 99.99%) were mixed and ground in an agate mortar and pestle. Samples

were pressed into 1 cm diameter pellets, using a pressure of 10 tons cm^{-2}, and sintered at temperatures ranging from 450 °C to 950 °C for up to 48 hours (Solid-State Samples A and B).[240,241] Excess Na_2CO_3 (~1-10%) was also added to a number of the solid-state reactions in an attempt to reduce the volatilisation of the Na (Solid-State Sample C). In addition, different cooling rates were tested: slow cooling and quenching techniques were compared. Using the molten salt method stoichiometric amounts of purchased Na_2O (Sigma-Aldrich, 80%) and Nb_2O_5 were ground and mixed with a quantity of NaCl equal to the total amount of reagents added and annealed at temperatures ranging from 850 °C to 1100 °C for between 3 and 48 hours. Once fully cooled, samples were washed in distilled H_2O, filtered and allowed to air dry at room temperature.[242] Using a sol-gel process sodium ethoxide (3.67 mmol) and niobium (V) ethoxide (2.99 mmol) were dissolved in 2-methoxyethanol (10 ml) and refluxed at 80 °C for 90 minutes then at 120 °C for an additional 90 minutes. Once fully heated, the solution was allowed to cool and the resultant product was sintered at 950 °C for 12 hours.[243] Post-synthetic ^{17}O enrichment of selected solid-state and molten salt samples was performed by heating each sample under 50% ^{17}O enriched O_2 gas (Isotec, 99% ^{17}O) for 7 days at 950 °C. All enrichments were completed in collaboration with Professor Clare Grey and Dr Frédéric Blanc at the State University of New York, Stony Brook.

3.2.2 X-ray and Neutron Powder Diffraction

Room temperature "laboratory" powder X-ray diffraction (l-PXRD) experiments were carried out on a Stoe STADI-P X-ray diffractometer using Cu $K_{\alpha 1}$ (λ = 1.54056 Å) radiation. Using Beamline I11 at the Diamond Light Source Synchrotron (λ = 0.827267 Å) high-resolution room temperature powder X-ray diffraction (s-PXRD) experiments were conducted.[122,123] Room temperature time-of-flight neutron powder diffraction (NPD) experiments were completed using the High Resolution Powder Diffractometer (HRPD) at the ISIS neutron spallation source, Rutherford-Appleton Laboratories. All diffraction data were analysed by

Rietveld refinement using the General Structure Analysis System (GSAS) software package.[125] Parameters refined included background coefficients, detector zero point, instrumental parameters, lattice parameters, profile coefficients, isotropic thermal factors and atomic positional coordinates. An absorption correction was also applied to the neutron diffraction data.

3.2.3 NMR Spectroscopy

Solid-state NMR spectra were acquired using either Bruker 400, 600 or 850 Avance III spectrometers, equipped with wide-bore 9.4 T, 14.1 T and 20 T magnets, respectively, using Larmor frequencies of 105.8 MHz, 158.75 MHz and 224.88 MHz for ^{23}Na (I = 3/2), 97.94 MHz, 146.89 MHz and 208.08 MHz for ^{93}Nb (I = 9/2) and 81.36 MHz for ^{17}O (I = 5/2). The finely powdered samples were tightly packed into conventional 4-, 3.2- and 2.5-mm ZrO_2 rotors and magic-angle spinning (MAS) rates of 14 kHz and 30 kHz respectively were employed. Chemical shifts were referenced to 1 M NaCl (aq), a saturated solution of $K[NbCl_6]$ in acetonitrile and H_2O (aq), using NaCl (s) (δ_{iso} = 7.8 ppm), $LiNbO_3$ (s) (centre of gravity of MAS lineshape at δ = –1036.4 ppm at 14.1 T) and 35% ^{17}O enriched clinohumite $4Mg_2SiO_4.Mg(OH)_2$ (δ = 57.0 ppm) as secondary references. Conventional ^{23}Na MAS NMR spectra were obtained using single pulse experiments at 9.4 T, 14.1 T and 20 T with typical (central-transition selective) pulse lengths of 0.9 μs, 1.1 μs and 1.1 μs respectively. Conventional ^{93}Nb and ^{17}O MAS NMR spectra were also obtained using single pulse experiments at 14.1 T with typical (central-transition selective) pulse lengths of 0.65 μs and 1.5 μs. Optimised recycle intervals for ^{23}Na, ^{93}Nb and ^{17}O were 3 s, 0.5 s and 20 s. Typical radiofrequency field strengths employed were between 100-170 kHz. Two-dimensional triple-quantum MAS NMR experiments were recorded at 9.4 T and 14.1 T using a phase-modulated rotor-synchronised split-t_1 shifted echo pulse sequence.[181] At 9.4 T spectra result from the averaging of 192 transients with a recycle interval of 3 s for each of the 98 t_1 increments of 126.98 μs, whilst at 14.1 T spectra result from the averaging of 96 transients with a recycle interval of 3 s for each of the 128 t_1 increments. ^{93}Nb MQMAS NMR spectra result from the

averaging of 1440 transients with a recycle interval of 0.5 s for each of the 48 t_1 increments of 117.6 μs, and an additional SPAM (soft-pulse added mixing)[189,190] pulse was added (resulting in a signal enhancement of ~40%). Static wideline ^{93}Nb spectra were recorded at 9.4 T, 14.1 T and 20 T using a spin-echo pulse sequence with central-transition selective pulses and a τ interval of 20 μs. A half-echo was recorded and the FID was left shifted prior to Fourier transformation. Conventional ^{17}O MAS NMR spectra were obtained using a spin-echo pulse sequence with a rotor synchronized τ interval of 64.04 μs. A half-echo was recorded and the FID was left shifted prior to Fourier transformation. Chemical shift scales are referenced according to the convention in Reference 185. Further experimental details can be found in the relevant figure captions. Spectral analysis and fitting was performed within Topspin 2.1.

3.2.4 Calculations

^{23}Na, ^{93}Nb and ^{17}O density functional theory (DFT) calculations were completed using the CASTEP[214] code. Calculations were converged as far as possible with respect to k-point spacing and cut-off energy, with typical values of 0.04 $Å^{-1}$ and 60 Ry, respectively. Crystal structures were obtained from both the Inorganic Crystal Structure Database and Rietveld refinement of experimental data. Where necessary, geometry optimisation of the structure was performed prior to calculation of the NMR parameters. The isotropic chemical shift, δ_{iso}, in each was obtained from the isotropic shielding, σ_{iso}, using $\delta_{iso} = -(\sigma_{iso} - \sigma_{ref})$, where σ_{ref} is the isotropic shielding (565.84 ppm for ^{23}Na, −648.12 ppm for ^{93}Nb and 253.70 ppm for ^{17}O), determined from calculations on the ilmenite polymorph of $NaNbO_3$,[225] $LiNbO_3$ and Mg_2SiO_4 respectively. Typical calculation times were up to 24 hours using 12 cores. All structure searching calculations utilised the *Ab Initio* Random Structure Searching[244-247] (AIRSS) algorithm and were completed using the CASTEP code with a planewave cut-off energy of 27 Ry and a Brillouin zone sampling grid spacing of 0.07 $Å^{-1}$. The lowest energy phases were then selected and their energies and properties were recalculated at a higher level of accuracy using a

planewave cut-off energy of 60 Ry and a grid spacing of 0.07 $Å^{-1}$. Refer to section 3.6 for specific details regarding the strategy utilised to structure search. All structure searching has been completed in collaboration with Professor Chris J. Pickard and Dr Maria Baias, University College London, UK.

3.2.5 Second Harmonic Generation (SHG)

Nonlinear Optic (NLO) properties were studied using powder Second Harmonic Generation (SHG) techniques. Samples were pressed between two microscope slides and analysed using a Nd vanadate pulsed laser. Each pulse had a typical duration of 12 ps. Pulses typically came in bundles of 2-5 and at a rate of 1 kHz. The beam diameter was 5 mm and the power used varied between 1 and 2.5 W.

3.2.6 Scanning Electron Microscopy (SEM)

The crystal morphology of each sample was examined using scanning electron microscopy (SEM) on a Jeol JSM-5600 microscope operating at 20-30 kV equipped with an Oxford INCA system for energy-dispersive X-ray spectroscopy (EDX).

3.3 Experimental Results

3.3.1 Commercial Sample

Initial investigations concentrated on $NaNbO_3$ purchased commercially (Sigma-Aldrich). Structure and phase purity were initially verified using l-PXRD and subsequently s-PXRD, both of which displayed excellent agreement with the orthorhombic structure reported in the literature (Pbcm).[248] The Rietveld refinement using the s-PXRD data is shown in Figure 3.2(a), and full refinement details can be found in Table 3.1. All bond lengths obtained from refinement are given in Appendix II. The ^{23}Na MAS NMR spectrum (Figure 3.2(b)) contains a broadened lineshape, hindering the extraction of information regarding the number

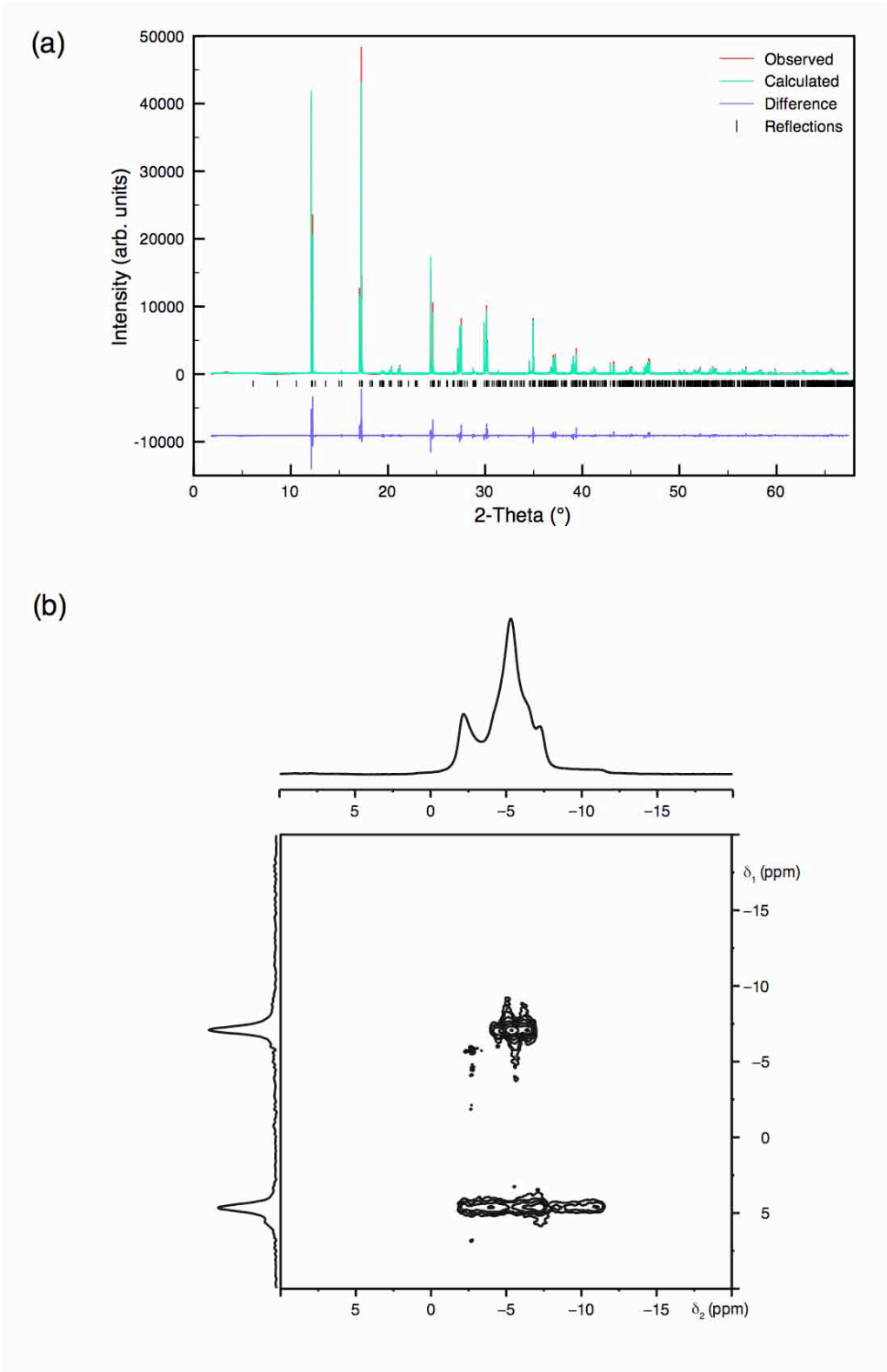

Figure 3.2: Commercial $NaNbO_3$ (Aldrich) (a) Rietveld profile (Pbcm model) of s-PXRD data and (b) conventional ^{23}Na (14.1 T) MAS NMR spectrum, triple-quantum MAS NMR spectrum and corresponding isotropic projection. The MAS rate was 14 kHz.

Table 3.1: Structural parameters for $NaNbO_3$ (Aldrich) from s-PXRD data using isotropic thermal factors. Space group Pbcm, a = 5.50398(1) Å, b = 5.56950(1) Å, c = 15.51647(1) Å and V = 475.648(1) Å^3. $\chi^2 = 7.9$, $wR_p = 14.6\%$ and $R_p = 10.9\%$.

Atom	Site	x	y	z	U(iso) × 100 / Å^2
Na	4c	0.2288(5)	0.25	0	1.62(9)
Na	4d	0.2296(5)	0.2243(3)	0.25	0.99(8)
Nb	8e	0.2525(1)	0.7316(1)	0.1250(1)	0.84(1)
O1	4c	0.6886(10)	0.25	0	0.61(16)
O2	4d	0.1846(10)	0.7541(6)	0.25	1.19(17)
O3	8e	0.4743(4)	0.4653(5)	0.1418(3)	2.43(9)
O4	8e	0.0330(4)	0.0292(4)	0.1108(3)	1.52(8)

of crystallographically distinct Na sites present. ^{23}Na (I = 3/2) is a quadrupolar nucleus and under conventional MAS ^{23}Na lineshapes commonly exhibit broadening as a result of the inefficient removal of second-order quadrupolar interactions. For this reason high-resolution NMR techniques such as multiple-quantum MAS[171] (MQMAS) are required to fully remove inhomogeneous second-order quadrupolar broadenings and resolve distinct sites. The ^{23}Na triple-quantum MAS spectrum of $NaNbO_3$, shown in Figure 3.2(b), clearly displays two distinct Na resonances, in agreement with the reported crystal structure for Pbcm $NaNbO_3$.[248] The projection of the spectrum onto the δ_1 axis also exhibits two sharp isotropic peaks, again highlighting the presence of two distinct Na environments. The NMR parameters extracted from the position of the centre of gravity from the spectrum in Figure 3.2(b) are given in Table 3.2. The upper, and notably narrower of the two ridges in the two-dimensional spectrum, with $\delta_{iso} = -4.2$ ppm, has $P_Q = 1.2$ MHz, whilst the lower ridge, with $\delta_{iso} = -0.6$ ppm, has a considerably larger quadrupolar contribution, $P_Q = 2.2$ MHz. It is possible to confirm the accuracy of the parameters extracted by simulating the MAS spectrum which would result. This is shown in Figure 3.3 and is in good agreement with that obtained experimentally.

Table 3.2: ^{23}Na NMR parameters, δ_{iso}, P_Q, C_Q and η_Q, for commercially purchased $NaNbO_3$ (Aldrich), Solid-State Sample A $NaNbO_3$ and sol-gel $NaNbO_3$ sample, obtained from the MAS and MQMAS spectra in Figures 3.2(b), 3.6(a-b) and 3.28(c) respectively.

	Site	δ_{iso} (ppm)	P_Q / MHz	C_Q / MHz	η_Q
Commercial Sample (Aldrich)					
Pbcm	Na1	−0.6(5)	2.2(1)	-	-
	Na2	−4.2(5)	1.2(2)	-	-
Solid-State Sample A (14.1 T)					
Pbcm	Na1	−0.7(5)	2.2(1)	-	-
	Na2	−4.4(5)	1.2(2)	-	-
"$P2_1ma$"	Na1	−5.1(5)	1.1(2)	-	-
Solid-State Sample A (9.4 T)					
Pbcm	Na1	−0.5(5)	2.1(1)	2.1(1)	0.0(1)
	Na2	−4.2(5)	1.2(2)	1.0(2)	0.8(1)
"$P2_1ma$"	Na1	−1.4(5)	2.4(1)	2.1(1)	0.9(1)
	Na2	−5.1(5)	1.2(2)	1.1(2)	0.7(1)
Sol-gel Sample					
"$P2_1ma$"	Na1	−1.5(5)	2.4(1)	-	-
	Na2	−5.1(5)	1.2(2)	-	-

3.3.2 Solid-State Preparation

$NaNbO_3$ was also synthesised using conventional solid-state techniques (Solid-State Sample A). Phase purity was examined using l-PXRD and displayed good agreement with the literature, initially suggesting the presence of single-phase Pbcm $NaNbO_3$, as shown in Figure 3.4(a). However, under MAS the ^{23}Na NMR spectrum appears different in comparison to that obtained for the commercially purchased sample, as shown in Figures 3.5(a) and (b). In addition, the crystallinity

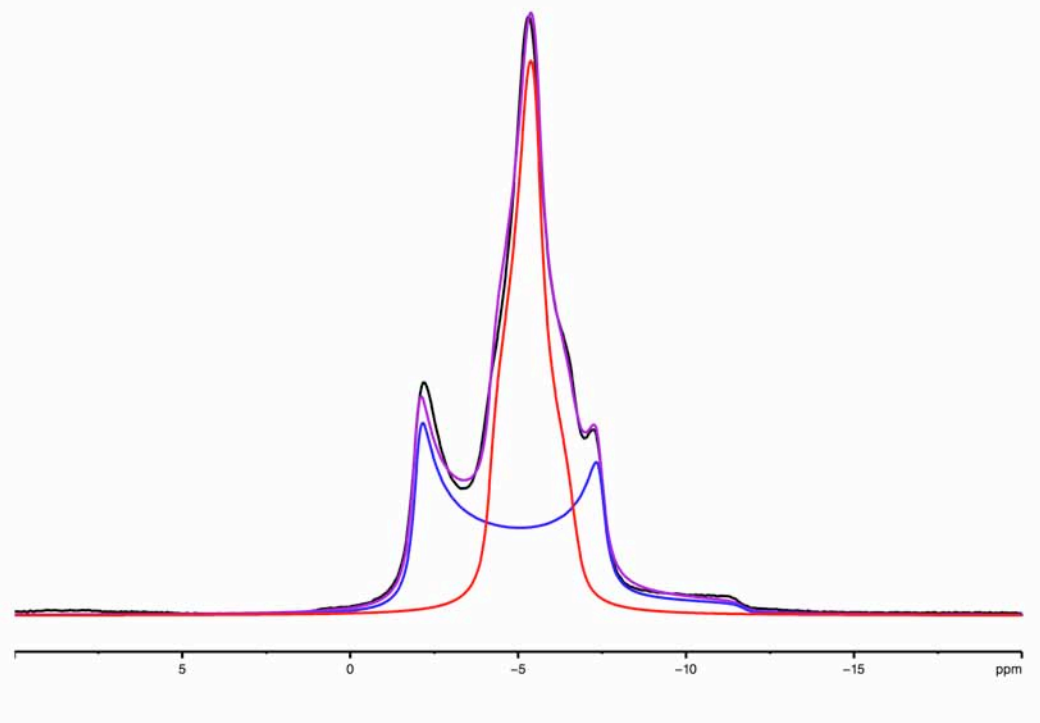

Figure 3.3: Analytical fitting of the ^{23}Na (14.1 T) MAS NMR spectrum of commercially-purchased (Aldrich) $NaNbO_3$. The experimental spectrum is shown in black, fitted lineshapes for the Na1 and Na2 sites are shown by the blue and red lines, respectively, with the summation of the two sites shown in purple.

and microstructure displayed visible differences (Figures 3.5(g) and (h)). Using ^{23}Na MQMAS NMR, however, it was evident a second Na-containing phase was present in Solid-State Sample A. At 14.1 T an additional resonance was clearly observed at $\delta_1 = -9.3$ ppm, as shown in Figure 3.6(a). In addition, the resonance at $\delta_1 = 4.3$ ppm covers a wider δ_2 shift range, suggesting the potential overlap of two resonances here also. This is highlighted in the overlay of the ^{23}Na MQMAS NMR spectra for this sample and that of the commercial material shown in Figure 3.7. Therefore, in an attempt to resolve any overlapped sites an MQMAS spectrum was recorded at 9.4 T. The position of resonance in an isotropic MQMAS spectrum depends not only upon the chemical shift but also on the quadrupolar interaction, and owing to the differing field dependences of these interactions (proportional to B_0 and B_0^{-1}, respectively) resolution may be improved both at lower and higher magnetic field strength. As shown in Figure 3.6(b) four crystallographically distinct Na sites are clearly observed, suggesting the presence of a second Na-containing

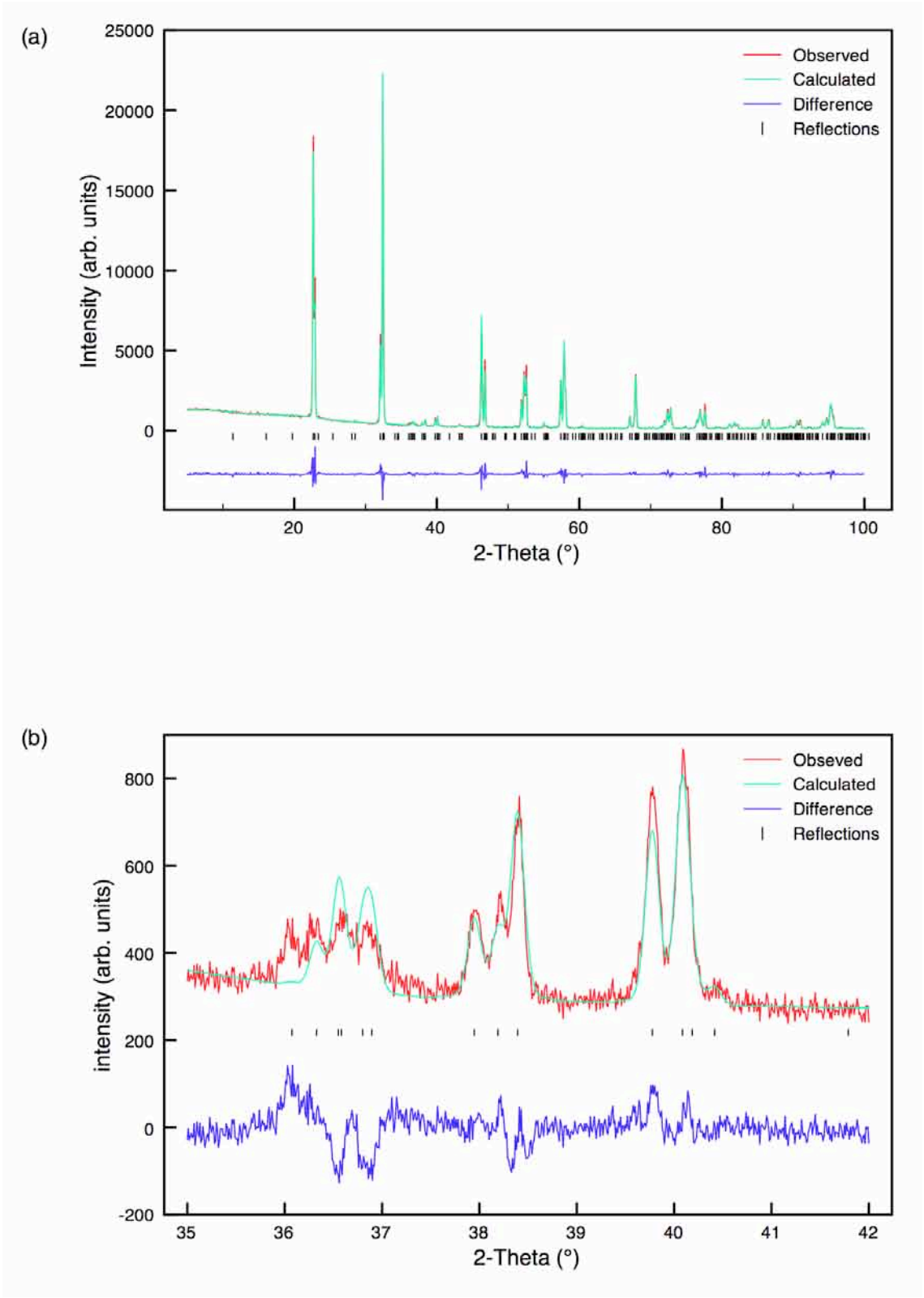

Figure 3.4: (a) Rietveld profile for Solid-State Sample A $NaNbO_3$ using l-PXRD data and Pbcm model, and (b) expansion of the superstructure region 2θ = 34° – 42°.

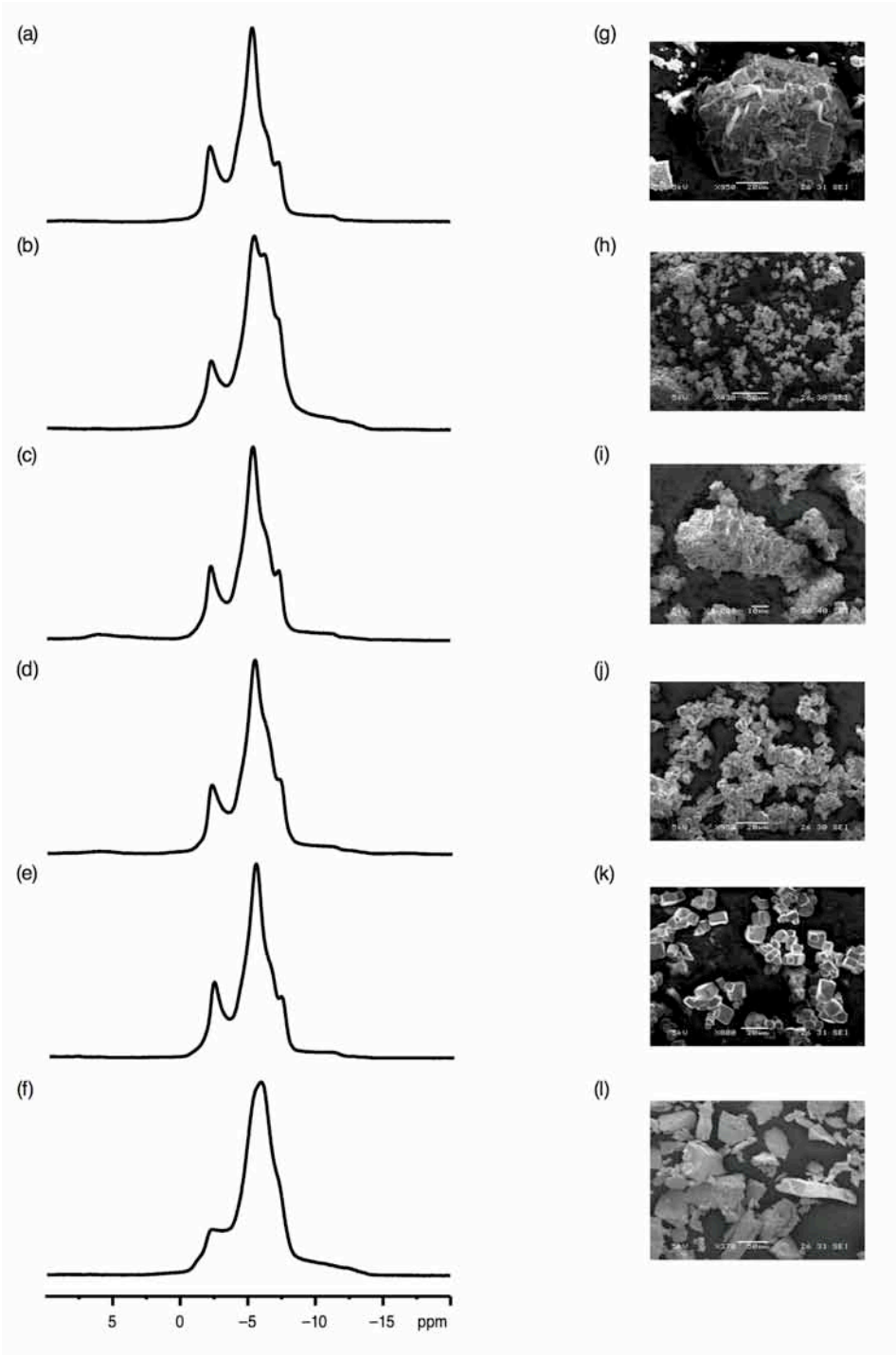

Figure 3.5: Comparison of (a-f) ^{23}Na (14.1 T) MAS NMR spectra and (g-l) Scanning Electron Microscopy (SEM) images of (a, g) commercially purchased $NaNbO_3$ (Aldrich), (b, h) Solid-State Sample A $NaNbO_3$, (c, i) Solid-State Sample B $NaNbO_3$, (d, j) Solid-State Sample C $NaNbO_3$, (e, k) molten salt $NaNbO_3$ (850°C for 24 hours) and (f, l) sol-gel $NaNbO_3$.

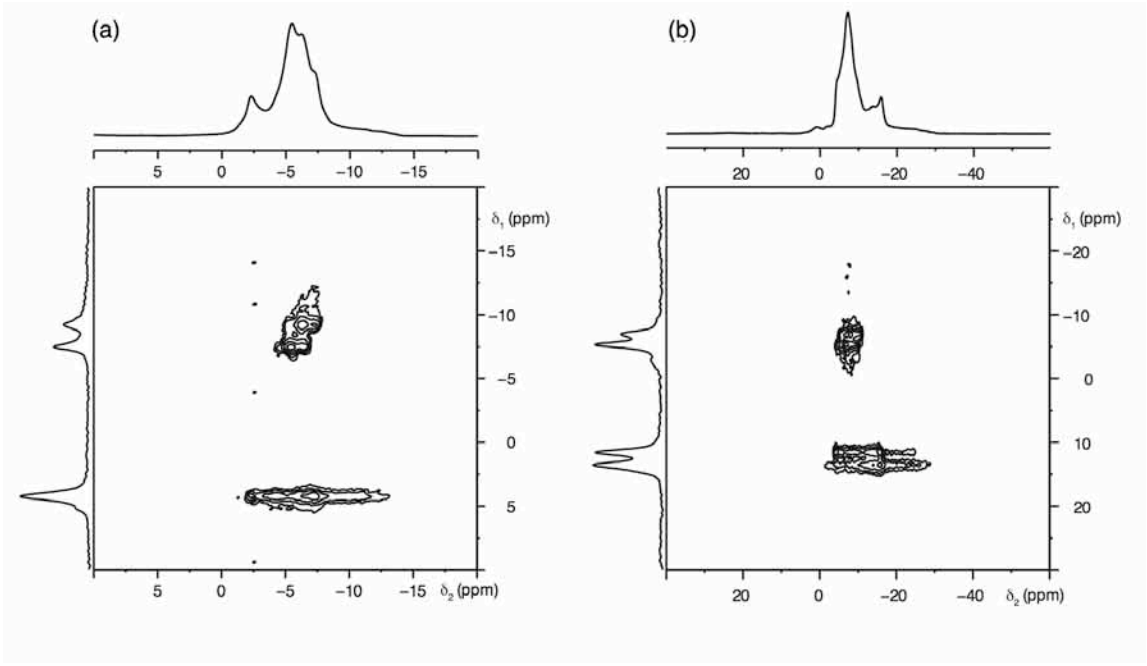

Figure 3.6: ^{23}Na MAS NMR spectra, triple-quantum MAS NMR spectra and corresponding isotropic projections for Solid-State Sample A $NaNbO_3$ at (a) 14.1 T and (b) 9.4 T. The MAS rate was 14 kHz.

phase, with two Na species. Although the intensity of resonances in MQMAS spectra is in general non-quantitative (i.e., does not accurately reflect the proportions of different phases), for species with very similar quadrupolar interactions it is possible to interpret spectral intensities in a quantitative way. The two peaks at δ_1 = –9.3 ppm and –7.5 ppm, suggest that the second phase accounts for ~40% of the material synthesised in this case. NMR parameters extracted for each phase at both 14.1 T and 9.4 T are given in Table 3.2. Accurate quadrupolar parameters could not be extracted for all sites owing to spectral overlap and significant line broadening and distortion, potentially caused by non-uniform triple-quantum excitation. Therefore, P_Q values derived from the position of the centre of gravity have been quoted for these sites. To confirm that the additional resonances observed were not unreacted Na-based starting reagents various anhydrous and hydrous samples of the starting reagent Na_2CO_3 were analysed using ^{23}Na MAS NMR. Two-dimensional ^{23}Na MQMAS spectra were recorded for two commercially purchased samples of anhydrous Na_2CO_3 (Sigma-Aldrich and Fisher Scientific), monohydrate Na_2CO_3 (Sigma-Aldrich) and sodium bicarbonate, $NaHCO_3$ (Sigma-

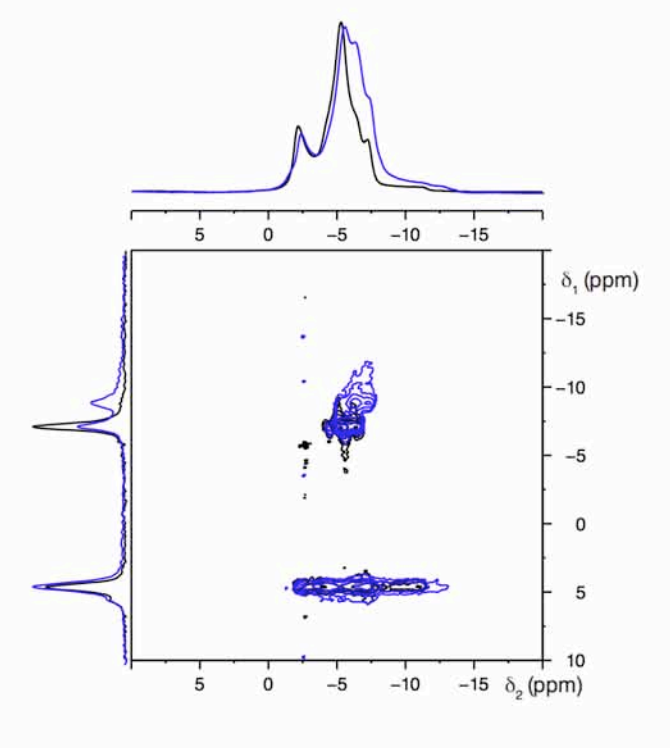

Figure 3.7: ^{23}Na (14.1 T) MAS NMR spectra, two-dimensional triple-quantum MAS NMR spectra and corresponding isotropic projections of phase pure commercially-purchased Pbcm $NaNbO_3$ (shown in black) and Solid-State Sample A $NaNbO_3$ (shown in blue). The MAS rate was 14 kHz.

Aldrich). Each spectrum confirmed that the additional resonance present in Solid-State Sample A did not correlate with any of the anhydrous or hydrous forms of the starting reagent Na_2CO_3. All two-dimensional spectra recorded are shown in Appendix II.

Using solid-state techniques several additional samples were synthesised to determine whether the extra phase identified in Solid-State Sample A was consistently and repeatably produced in all samples synthesised using solid-state methods. Various experimental conditions were thoroughly investigated, including annealing temperature and time, the effects of different cooling rates (e.g., quenching vs. slow cooling) as well as the effect of addition of an excess (1-10%) of the primary starting reagent, Na_2CO_3. An excess was added in order to compensate for the volatile nature of the Na-based starting reagents. Using solely l-PXRD Rietveld refinements were completed for all samples and initially suggested the presence of a single-phase perovskite in space group Pbcm.

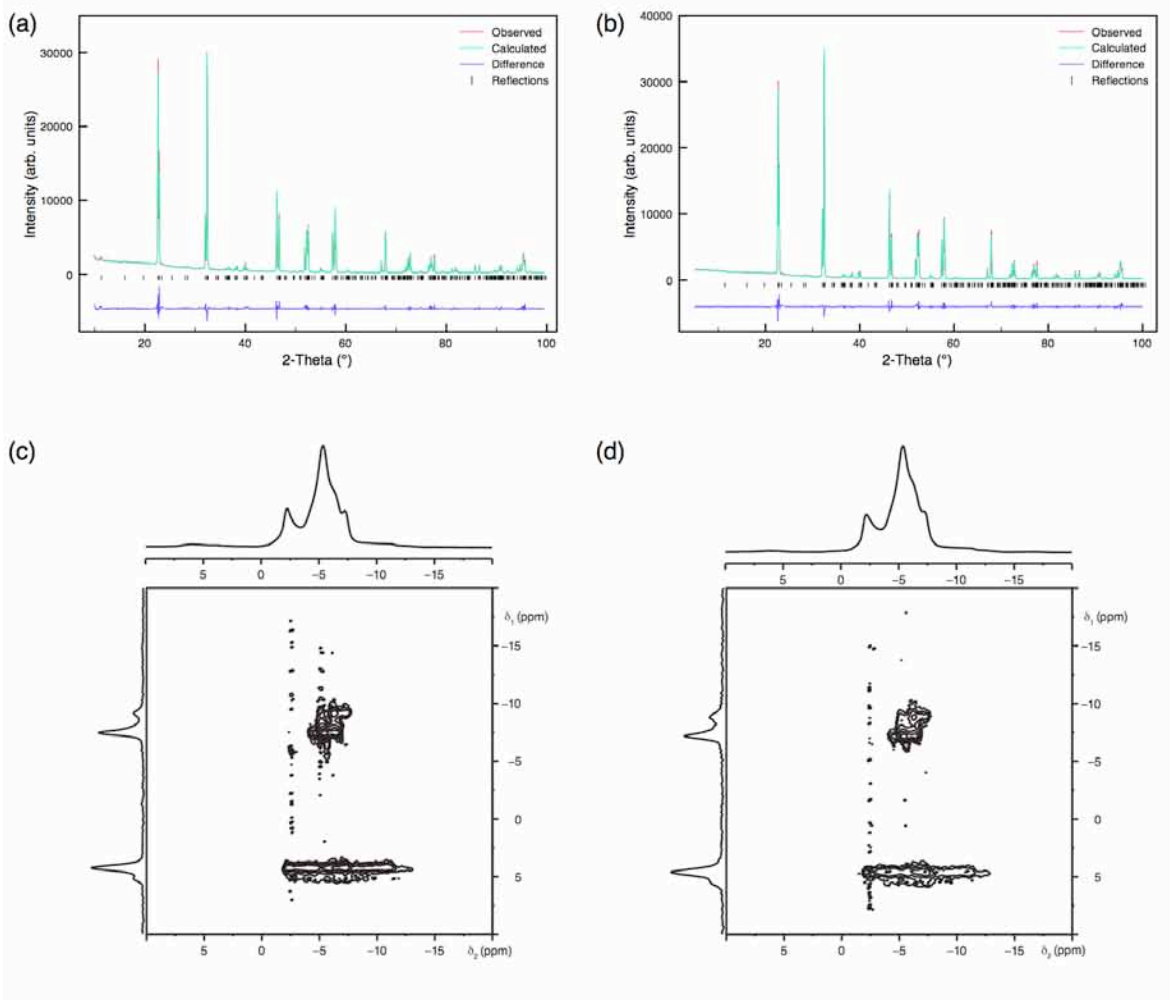

Figure 3.8: Rietveld profiles of l-PXRD data using Pbcm model for (a) Solid-State Sample B $NaNbO_3$ and (b) Solid-State Sample C $NaNbO_3$. Refined lattice parameters for each are located in Table 3.3. Conventional ^{23}Na (14.1 T) MAS NMR spectra, triple-quantum MAS NMR spectra and corresponding isotropic projections for (c) Solid-State Sample B $NaNbO_3$ and (d) Solid-State Sample C $NaNbO_3$.

Full Rietveld refinements for Solid-State Samples B and C are shown in Figures 3.8(a) and (b). The refined lattice parameter values from each refinement are given in Table 3.3. Again, using ^{23}Na MAS NMR the lineshapes obtained for Solid-State Samples B and C displayed subtle variations when compared with the commercially purchased sample, suggesting a different composition within each (Figures 3.5(a), (c) and (d)). This is perhaps more easily seen when the lineshapes for these different phases are superimposed, as shown in Figure 3.9. Upon closer inspection using two-dimensional ^{23}Na MQMAS NMR it was evident the same secondary phase was consistently present, with two additional Na sites.

Table 3.3: Refined lattice parameters, χ^2, wRp and Rp values for (a) Solid-State Sample B and (b) Solid-State Sample C, both from l-PXRD data. All refinements were completed using the Pbcm model by Chizhova *et al.*[248]

	a (Å)	b (Å)	c (Å)	V (Å^3)	χ^2	wR_p (%)	R_p (%)
(a)	5.50746(4)	5.57290(4)	15.52295(10)	476.438(7)	5.0	7.5	5.5
(b)	5.51131(5)	5.57569(4)	15.53211(11)	477.291(8)	6.0	8.4	6.0

Interestingly, Solid-State Samples A and B were synthesised using exactly the same reaction conditions. However, the two possess very different ratios of the two phases, as shown in Figure 3.8. Using variations of the original solid-state synthesis it was possible to vary the quantities of each phase significantly, from as little as a few percent to almost a 50% mix of the two; however the Pbcm phase was consistently present in abundance, suggesting it to be the more thermodynamically stable of the two. It was possible to slightly reduce the quantity of second phase by addition of a small excess of Na_2CO_3, as in Solid-State Sample C; however it was never possible to fully eradicate it using such methods.

Systematic studies of both annealing temperature and time were completed to accurately determine the effect on quantity of second phase produced. Initially, the annealing temperature was fixed at 850 °C and reaction times were varied between 3 and 72 hours. All l-PXRD data for each of the samples in this series refined well to the orthorhombic Pbcm model,[248] with no obvious additional peaks. This therefore suggested the presence of a single phase perovskite. The Rietveld refinements completed for each sample in this series are shown in Figures 3.10(a-g). However, two-dimensional ^{23}Na MAS NMR spectra indicated the presence of an additional Na-bearing phase, clearly visible in Figures 3.11(a-g). The same second phase was consistently produced in all samples; however, the quantities exhibited varied considerably. This variation is easily observed in the isotropic projections obtained from each two-dimensional spectrum, as shown in Figure 3.12(a). It must be noted that the sample annealed at 850 °C for 36 hours exhibits two considerably

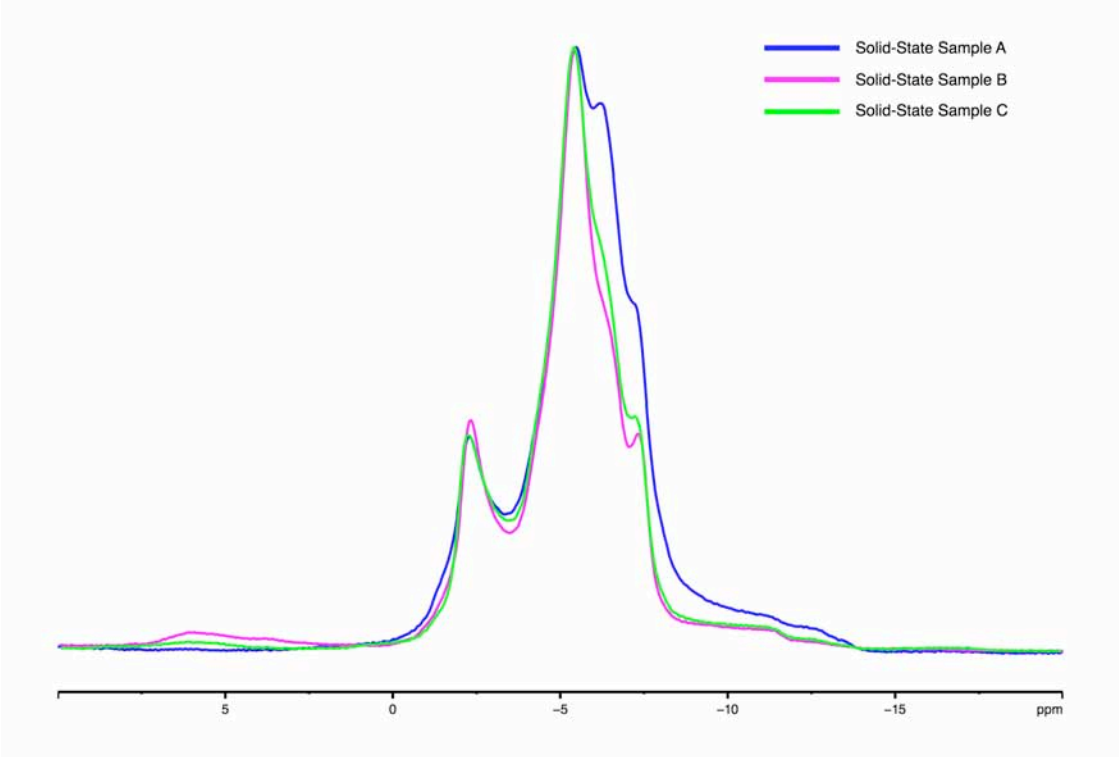

Figure 3.9: Overlay of ^{23}Na (14.1 T) MAS NMR spectra for Solid-State Samples A, B and C $NaNbO_3$.

broader isotropic peaks when compared with all other samples in this series, most probably owing to poor crystallinity. A second heating series was also completed in which the annealing temperature remained constant at 950 °C and reaction time was again varied. In this particular series, relatively short annealing times were investigated, from 15 minutes to 5 hours and in a similar manner to the earlier series all l-PXRD data refined to the orthorhombic Pbcm model,[248] suggesting each to be single phase. All Rietveld refinements completed for this series are shown in Figures 3.13(a-h). Refined lattice parameters obtained from each refinement are given in Appendix II. However, the two-dimensional ^{23}Na MQMAS NMR spectra recorded for each highlights the presence of the same secondary phase previously identified, indicating it is consistently synthesised in all solid-state samples, irrespective of annealing temperature or time. All ^{23}Na MQMAS spectra recorded in this series are shown in Figures 3.14(a-h). Only the relative quantities of the additional phase appeared to vary depending on the specific synthesis conditions

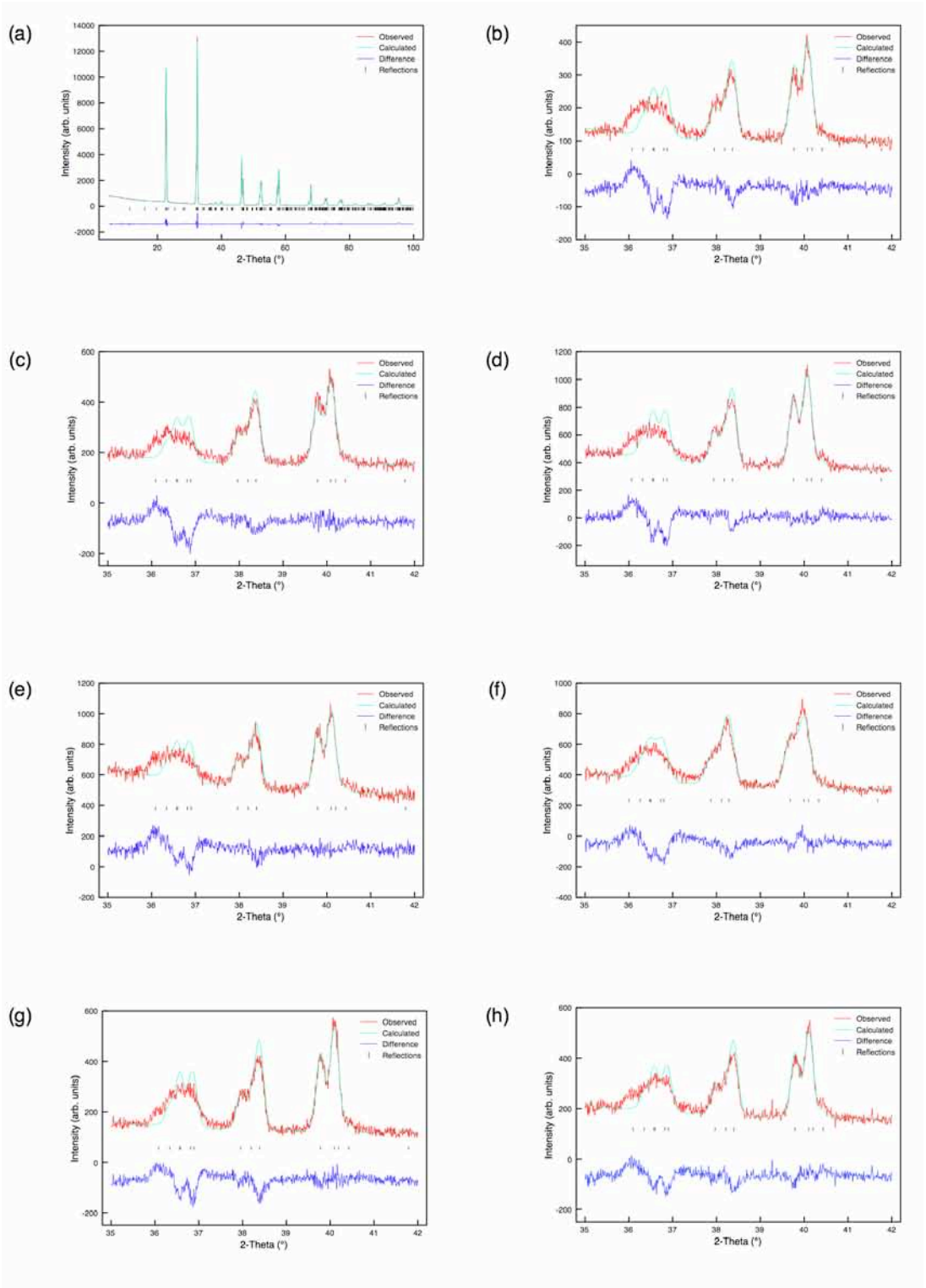

Figure 3.10: Rietveld profiles of l-PXRD data for samples of $NaNbO_3$ prepared in the solid-state heating series where annealing time was varied using (a) 3 hours, (c) 6 hours, (d) 12 hours, (e) 24 hours, (f) 36 hours, (g) 48 hours and (h) 72 hours. In each, the annealing temperature was fixed at 850 °C. Full Rietveld profiles for all samples are given in Appendix II.

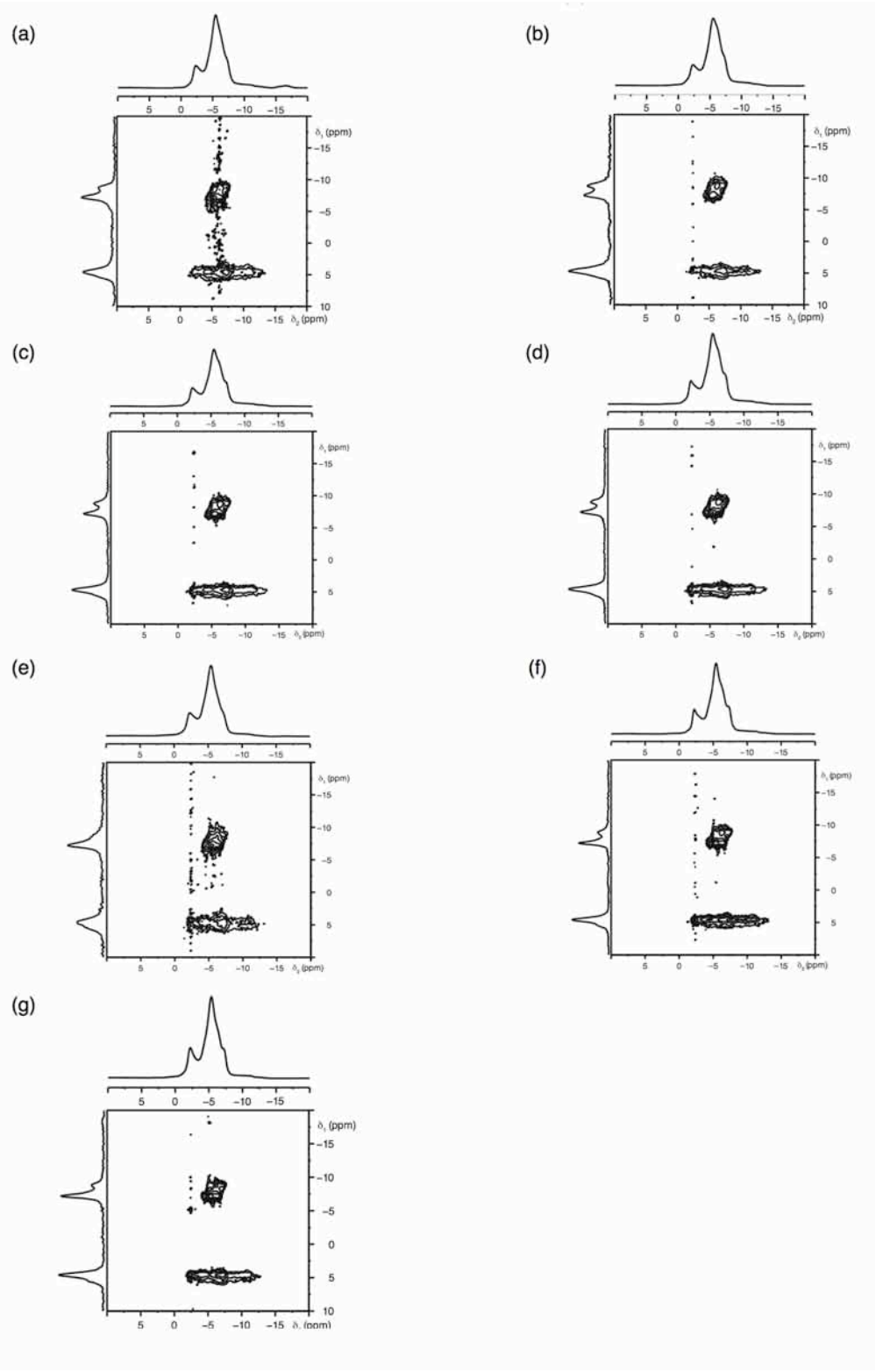

Figure 3.11: Conventional ^{23}Na (14.1 T) MAS NMR spectra, triple-quantum ^{23}Na MAS NMR spectra and corresponding isotropic projections, for solid-state samples of $NaNbO_3$ prepared using annealing times of (a) 3 hours, (b) 6 hours, (c) 12 hours, (d) 24 hours, (e) 36 hours and (f) 48 hours. In each case the annealing temperature was fixed at 850 °C.

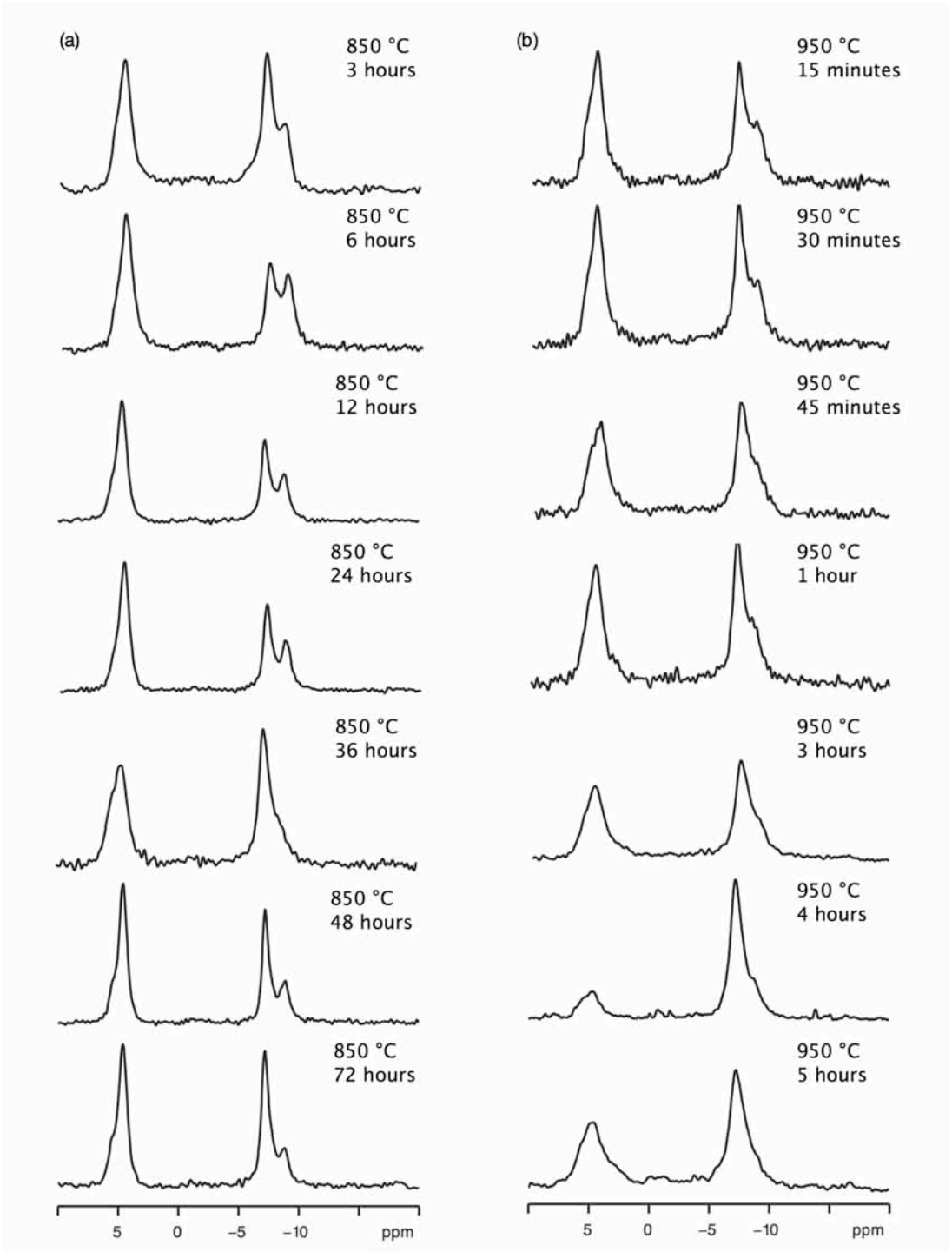

Figure 3.12: Isotropic projections obtained from triple-quantum ^{23}Na (14.1 T) MAS NMR spectra of solid-state samples of $NaNbO_3$. In (a), annealing time was varied between 3 and 48 hours, with a fixed annealing temperature of 850 °C. In (b), the annealing time was varied from 15 minutes to 6 hours, with a fixed annealing temperature of 950 °C.

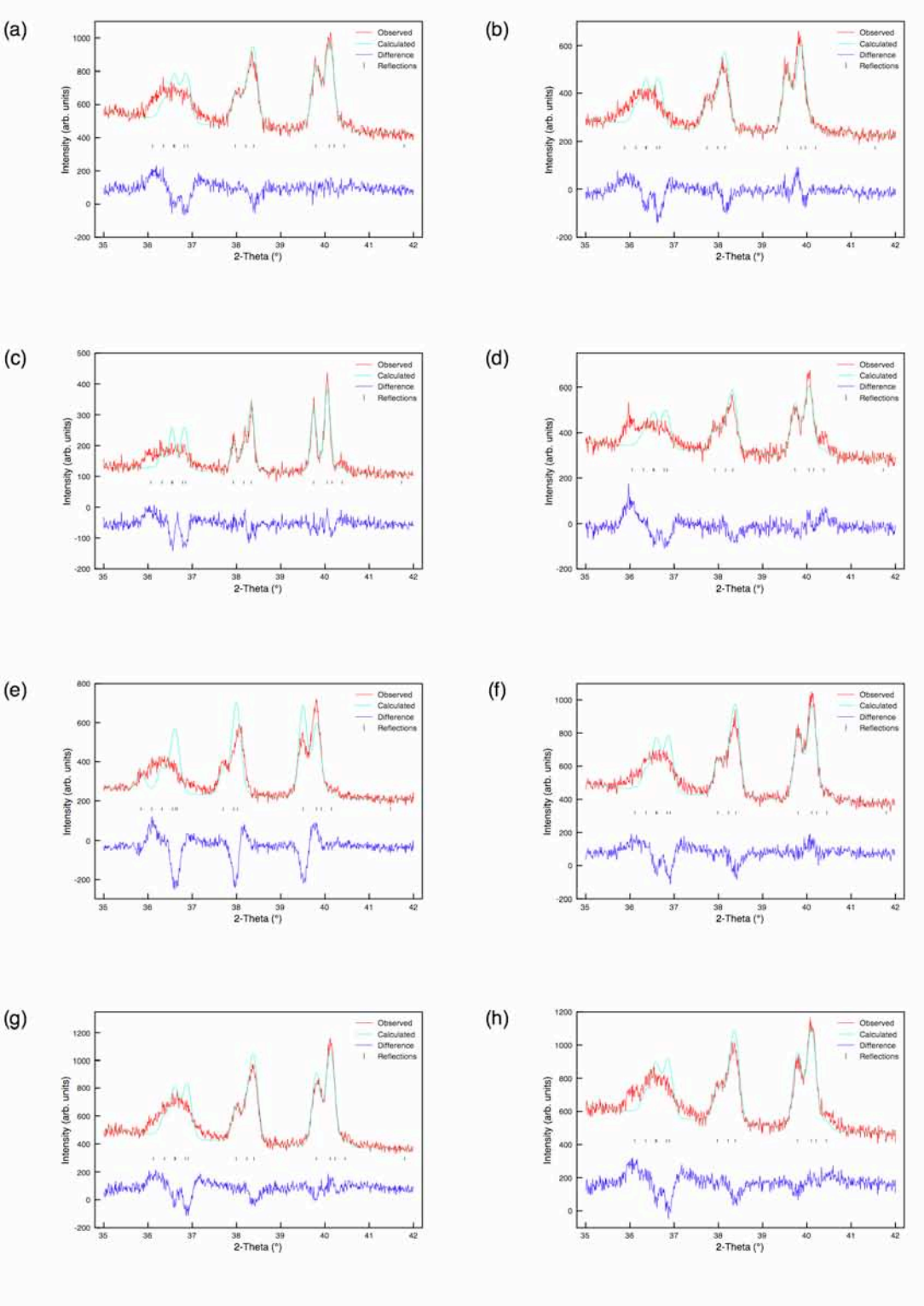

Figure 3.13: Rietveld profiles of l-PXRD data for samples of $NaNbO_3$ prepared in the solid-state heating series where annealing time was varied using (a) 15 minutes, (b) 30 minutes, (c) 45 minutes, (d) 1 hour, (e) 3 hours, (f) 4 hours, (g) 5 hours and (h) 6 hours. In each, the annealing temperature was fixed at 950 °C. Full Rietveld profiles can be found in Appendix II.

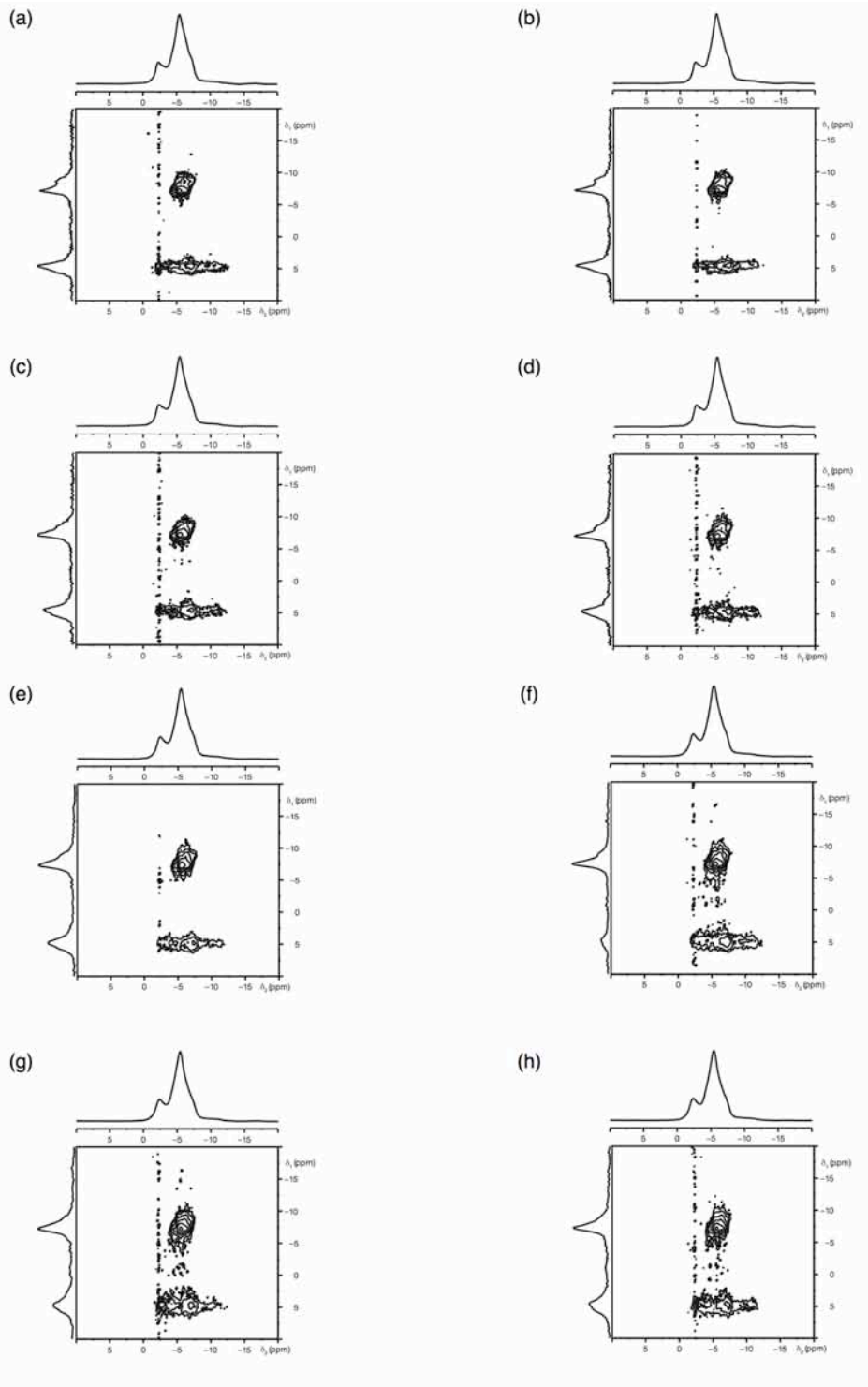

Figure 3.14: Conventional ^{23}Na (14.1 T) MAS NMR spectra, triple-quantum ^{23}Na MAS NMR spectra and corresponding isotropic projections, for solid-state samples of $NaNbO_3$ prepared using annealing times of (a) 15 minutes, (b) 30 minutes, (c) 45 minutes, (d) 1 hour, (e) 3 hours, (f) 4 hours, (g) 5 hours and (i) 6 hours. In each case the annealing temperature was fixed at 950 °C.

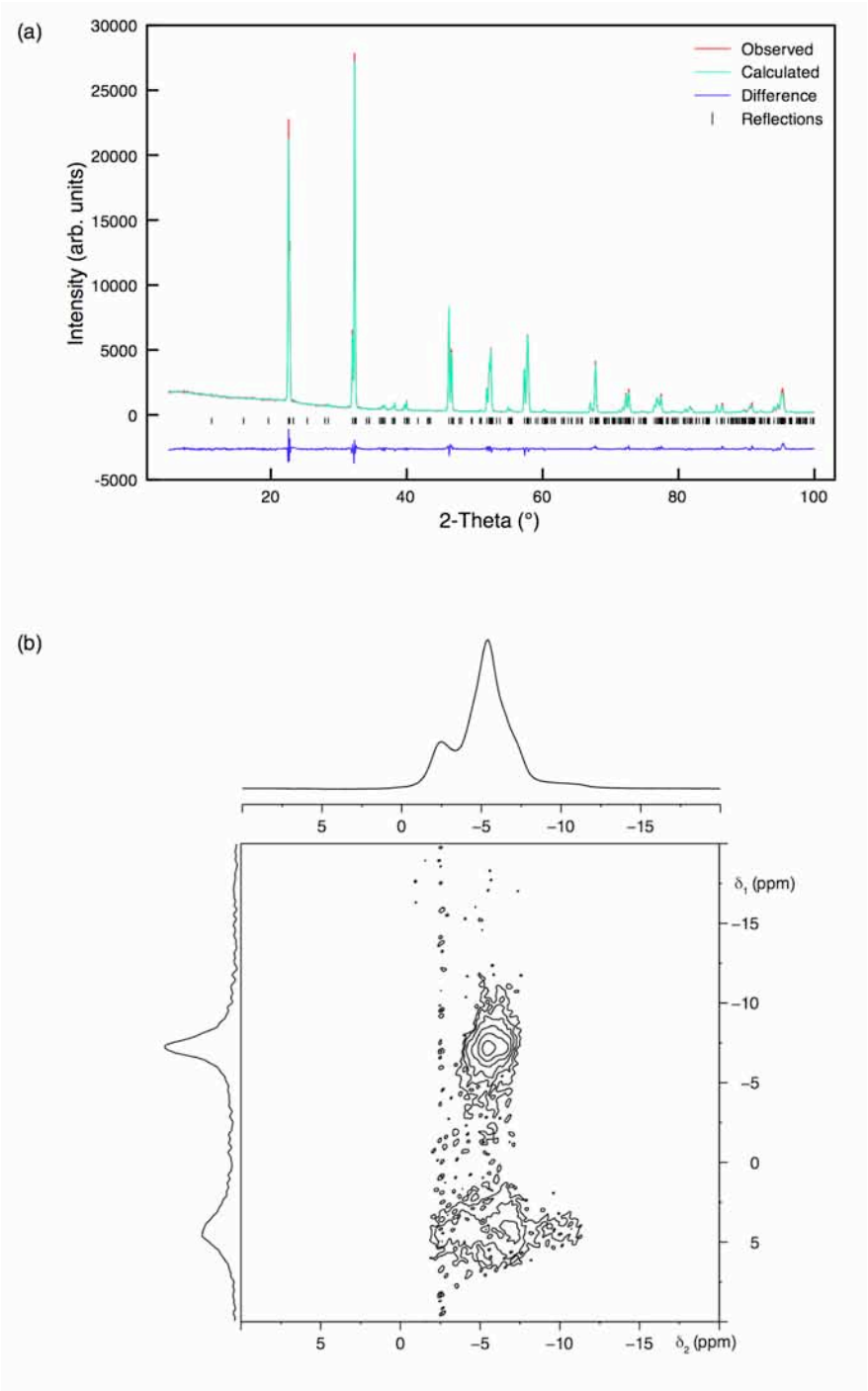

Figure 3.15: (a) Rietveld profile and (b) conventional ^{23}Na (9.4 T) MAS NMR spectrum, triple-quantum MAS NMR spectrum and corresponding isotropic projection for solid-state sample of $NaNbO_3$ prepared using an annealing temperature of 1000 °C for 24 hours.

used. The isotropic projections obtained from each two-dimensional spectrum displayed severe peak broadening (Figure 3.12(b)), suggesting all samples in this series to possess relatively poor crystallinity.

In such cases it is difficult to quantitatively measure the amount of second phase in each sample. This reduction in crystallinity is, most probably, as a result of the use of both relatively short reaction times and high annealing temperatures. Fast reaction rates commonly produce samples with low crystallinity. A sample of $NaNbO_3$ was also synthesised using 1000 °C for 24 hours to determine the effect of higher annealing temperature on sample crystallinity. Using l-PXRD the sample refined well the Pbcm phase of $NaNbO_3$, suggesting a single phase perovskite. The ^{23}Na MQMAS spectrum displayed two broad resonances, as shown in Figure 3.15(b). The spectrum exhibited considerable peak broadening when compared with other samples of $NaNbO_3$. The broadening exhibited is believed to be owing to a reduction in crystallinity in the sample. This, therefore, suggests that to successfully synthesise samples of $NaNbO_3$ with good crystallinity lower annealing temperatures are required. For example, samples synthesised using 850 °C appear to possess very good crystallinity, therefore, temperatures close to this should be utilised to synthesise samples of reasonably high crystallinity.

The systematic studies completed appear to suggest that there is no obvious correlation between the conditions of the solid-state synthesis and the quantity of the second phase produced. All solid-state experimental conditions were tested multiple times to establish the feasibility of achieving reproducible results, each of which confirmed it was not possible to routinely synthesise samples with identical ratios of the two phases. This is perhaps more easily observed in Figures 3.12(a) and (b) where the isotropic projections obtained from each two-dimensional spectrum for both heating series have been overlaid and compared. This suggests solid-state synthesis is not an easily controlled experimental method and, in this particular case, it is presumably owing to the volatile nature of the Na-based starting reagents. Working with highly volatile materials can lead to a non-stoichiometric reaction mixture, resulting in incomplete reaction or, more commonly, the formation of unknown intermediate phases. It is also extremely difficult to ensure complete mixing of the powdered starting reagents; therefore, to overcome this, the precursors are often mixed in a solvent (commonly

acetone or ethanol) prior to reaction at high annealing temperatures. This reduces particle size and ensures complete mixing of the powders. In contrast to sol-gel techniques, solid-state methods commonly produce samples with reasonably good crystallinity. This is highlighted in Figures 3.5(h-j) in which partially formed cube-like microstructures are observed for Solid-State Samples A and C. To obtain highly crystalline samples a relatively slow rate of reaction is required.

The sample containing the largest quantity of the second phase (~50%), Solid-State Sample A, was analysed in more detail. Using l-PXRD it was virtually impossible to identify any significant differences between this and that of phase pure Pbcm $NaNbO_3$, indicating the two phases must be, structurally, very closely related. X-ray diffraction principally examines the long-range order within a material whereas solid-state NMR investigates more local, short-range effects. The two techniques are therefore highly complementary to one another and enable enhanced structural characterisation of many complex solids. For the case of $NaNbO_3$, solid-state NMR provides more detailed information regarding the number of crystallographically distinct Na sites present and, in turn, the number of phases. NMR identifies the presence of two highly crystalline phases, confirming that X-ray diffraction is not simply missing the identification of an amorphous phase. This, in turn, provides confirmation that both phases diffract in a similar manner producing peaks that essentially overlap, thereby suggesting the second phase to be a polymorph of $NaNbO_3$ rather than an impurity phase. Without high-resolution diffraction data, it is extremely challenging to distinguish between the two; with the only subtle visible discrepancies occurring in the superstructure peaks ($2\theta = 34° - 42°$), as shown in Figure 3.4(b). However, solid-state NMR generally does not provide detailed information regarding the symmetry adopted within a structure or the precise location of the oxygen or sodium positions. To obtain this detailed information, diffraction is a necessity. Neutron diffraction is therefore essential for the study of $NaNbO_3$ as it enhances superstructure peaks and enables accurate location of the oxygen atoms, which ultimately aids in structural refinement and, in turn, spectral interpretation. Hence, both

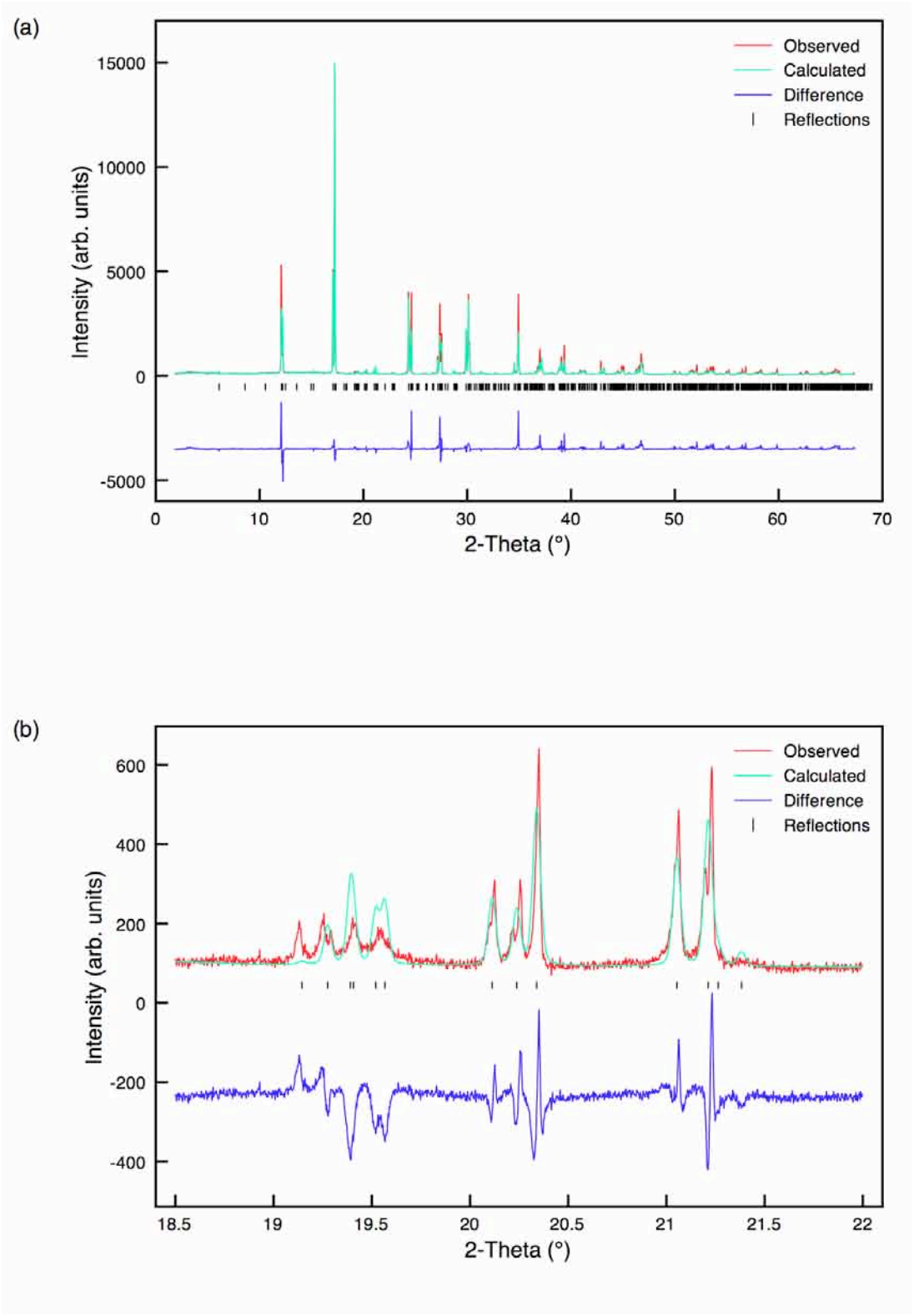

Figure 3.16: (a) Rietveld profile of s-PXRD data using Pbcm model for Solid-State Sample A $NaNbO_3$, (b) expansion of the corresponding superstructure peaks, 2θ = 18.5° – 22°.

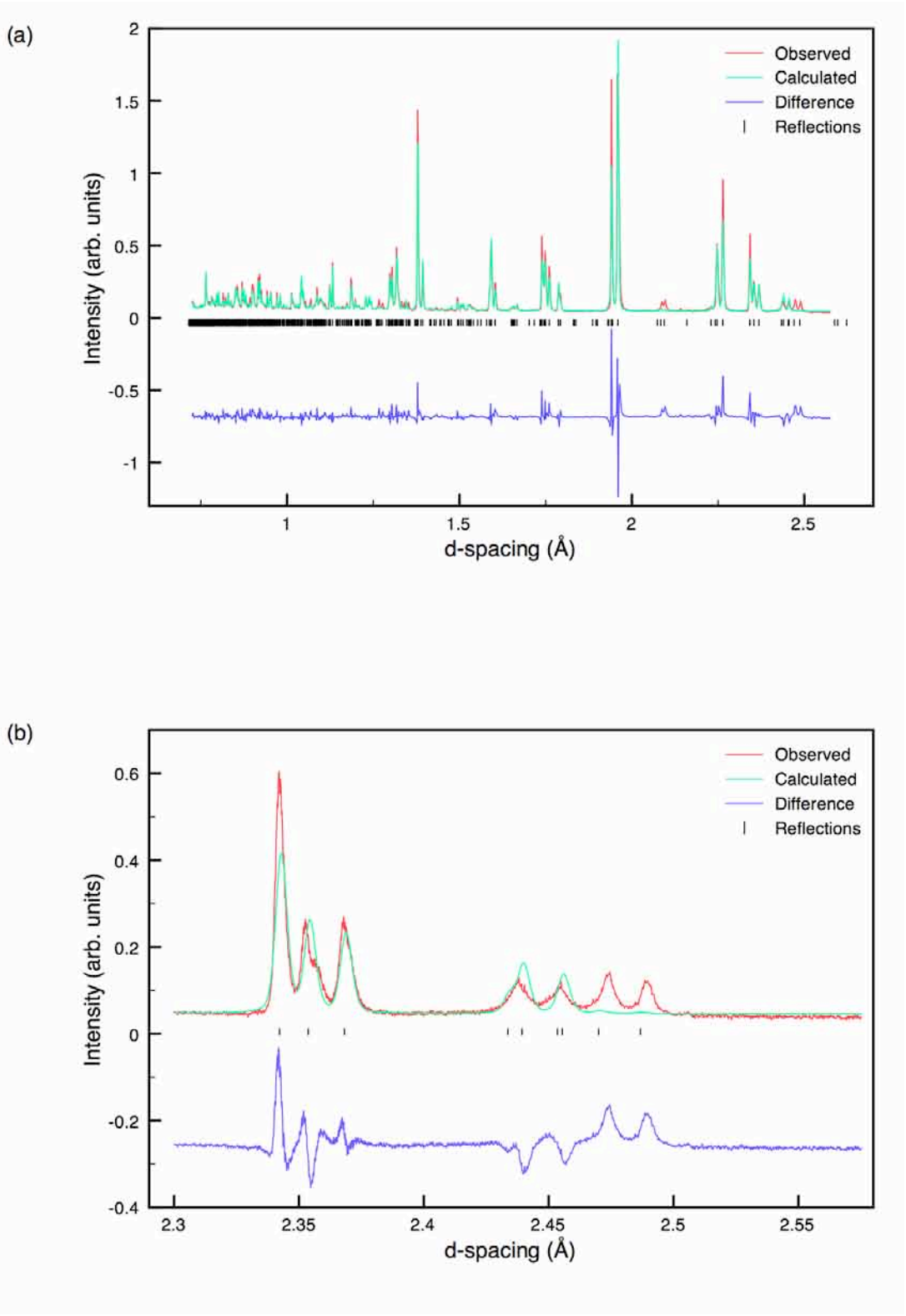

Figure 3.17: (a) Rietveld profile of NPD data using Pbcm model for Solid-State Sample A $NaNbO_3$, (b) expansion of the corresponding superstructure peaks, d = 2.3 Å – 2.55 Å.

Table 3.4: Structural parameters for Solid-State Sample A $NaNbO_3$ from s-PXRD data using isotropic thermal factors. Space group Pbcm, a = 5.51010(4) Å, b = 5.57279(3) Å, c = 15.52287(6) Å and V = 476.655(3) Å^3. χ^2 = 23.0, wR_p = 24.5% and R_p = 17.6%.

Atom	Site	x	y	z	U(iso) × 100 / Å^2
Na1	4c	0.2455(12)	0.25	0	2.00(5)
Na2	4d	0.2426(11)	0.2227(15)	0.25	0.40(4)
Nb1	8e	0.2577(2)	0.7412(2)	0.1251(4)	0.83(1)
O1	4c	0.6804(20)	0.25	0	3.49(10)
O2	4d	0.1817(21)	0.7725(28)	0.25	3.49(10)
O3	8e	0.4981(17)	0.4428(13)	0.1414(8)	3.49(10)
O4	8e	0.0159(21)	0.0075(19)	0.1100(8)	3.49(10)

Table 3.5: Structural parameters for Solid-State Sample A $NaNbO_3$ from NPD data using isotropic thermal factors. Space group Pbcm, a = 5.51088(7) Å, b = 5.57325(6) Å, c = 15.52551(17) Å and V = 476.843(7) Å^3. χ^2 = 61.1, wR_p = 13.8% and R_p = 13.6%.

Atom	Site	x	y	z	U(iso) × 100 / Å^2
Na1	4c	0.2585(14)	0.25	0	3.5(2)
Na2	4d	0.2606(10)	0.2298(10)	0.25	0.92(12)
Nb1	8e	0.2511(4)	0.7408(4)	0.1256(2)	1.19(5)
O1	4c	0.6956(8)	0.25	0	2.85(12)
O2	4d	0.1796(6)	0.7670(6)	0.25	0.08(6)
O3	8e	0.4619(6)	0.4513(5)	0.1417(3)	3.32(9)
O4	8e	0.0200(5)	0.0163(5)	0.1094(2)	1.62(6)

high-resolution synchrotron X-ray and neutron powder diffraction were undertaken on Solid-State Sample A.

The high-resolution diffraction data collected for Solid-State Sample A were analysed in significant detail and single phase refinements were completed for both datasets using the Pbcm model[248] and are shown in Figures 3.16(a) and 3.17(a). Full refinement details including structural parameters are given in Tables 3.4 and 3.5, respectively. It was immediately apparent in both datasets that a single model was insufficient owing to considerable discrepancies between the theoretical model and experimental data. The Rietveld refinement completed using the s-PXRD data highlighted regions in which shoulders and/or peaks were unaccounted for, as shown in Figure 3.16(b). Upon closer inspection it was evident split peaks were not indexed by the model and the lattice parameters considered them as simply single peaks. In addition, a number of the most intense peaks were not allocated sufficient intensity by the model, leading to relatively poor agreement factor, wR_p (24.5%) and χ^2 (23.0) values. The Rietveld refinement completed using the NPD data was significantly more informative, and is shown in Figure 3.17(a). Neutron diffraction enhances superstructure peaks therefore the small discrepancies initially identified by l-PXRD were magnified considerably by neutrons. The quality of refinement produced using solely the conventional Pbcm model was relatively poor (wR_p = 13.8% and χ^2 = 61.1), in particular over lower d-spacings. More specifically, two peaks in the experimental data at 2.47 Å and 2.49 Å were not accounted for in the model, suggesting they were associated with the additional polymorph present. These peaks are highlighted in Figure 3.17(b). Using this in conjunction with the ^{23}Na NMR data it was obvious a second phase very closely related to the orthorhombic Pbcm phase was present. A more detailed discussion of the possibility of multiphase refinements for Solid-State Sample A is given later.

3.3.3 Molten Salt Preparation

Initially, the precise experimental conditions required to synthesise a sample of $NaNbO_3$ using molten salt techniques were unknown therefore several 'test' reactions were undertaken to establish feasible reaction conditions. Using an annealing temperature of 850 °C for 24 hours a sample of $NaNbO_3$ was synthesised. Phase purity was verified using PXRD, and Rietveld refinement confirmed the sample refined well to the orthorhombic structure, Pbcm, as shown in Figure 3.18(a). EDX analysis revealed no presence of residual Cl^- from the synthesis. These spectra are given in Figure 3.19. The ^{23}Na MAS NMR spectrum recorded produced a broadened lineshape which appeared subtly different from the commercially purchased sample (Figures 3.5(a) and (e)). An overlay of these lineshapes is also shown in Figure 3.20. The conventional ^{23}Na MAS NMR spectrum failed to provide adequate information regarding both the composition of the sample and number of crystallographically distinct Na sites present; hence MQMAS techniques were utilised. The triple-quantum ^{23}Na MQMAS spectrum, as shown in Figure 3.21(a), indicated the presence of a second Na-containing phase, as observed for materials synthesised using solid-state methods (see Figures 3.6, 3.11 and 3.14). The isotropic spectrum indicated the quantity of this phase to be considerably reduced (to ~1-5%) when compared with the samples prepared using solid-state synthesis. Such a result suggested this synthetic method to be the most promising way of significantly reducing the phase or even eradicating it completely. Therefore, using this approach a systematic study of annealing temperature and time was completed to determine the effect on the quantity of second phase produced. Samples synthesised using this method possessed morphological uniformity, most probably owing to intimate mixing of the starting reagents due to reaction in a liquid medium. In particular, samples synthesised using an annealing temperature of 1000 °C for 24 hours produced crystallites with almost fully formed cube-like microstructures, shown in Figure 3.5(k). This cube-like microstructure was consistently produced for each sample synthesised using molten salt methods. To emphasise the regularity of the

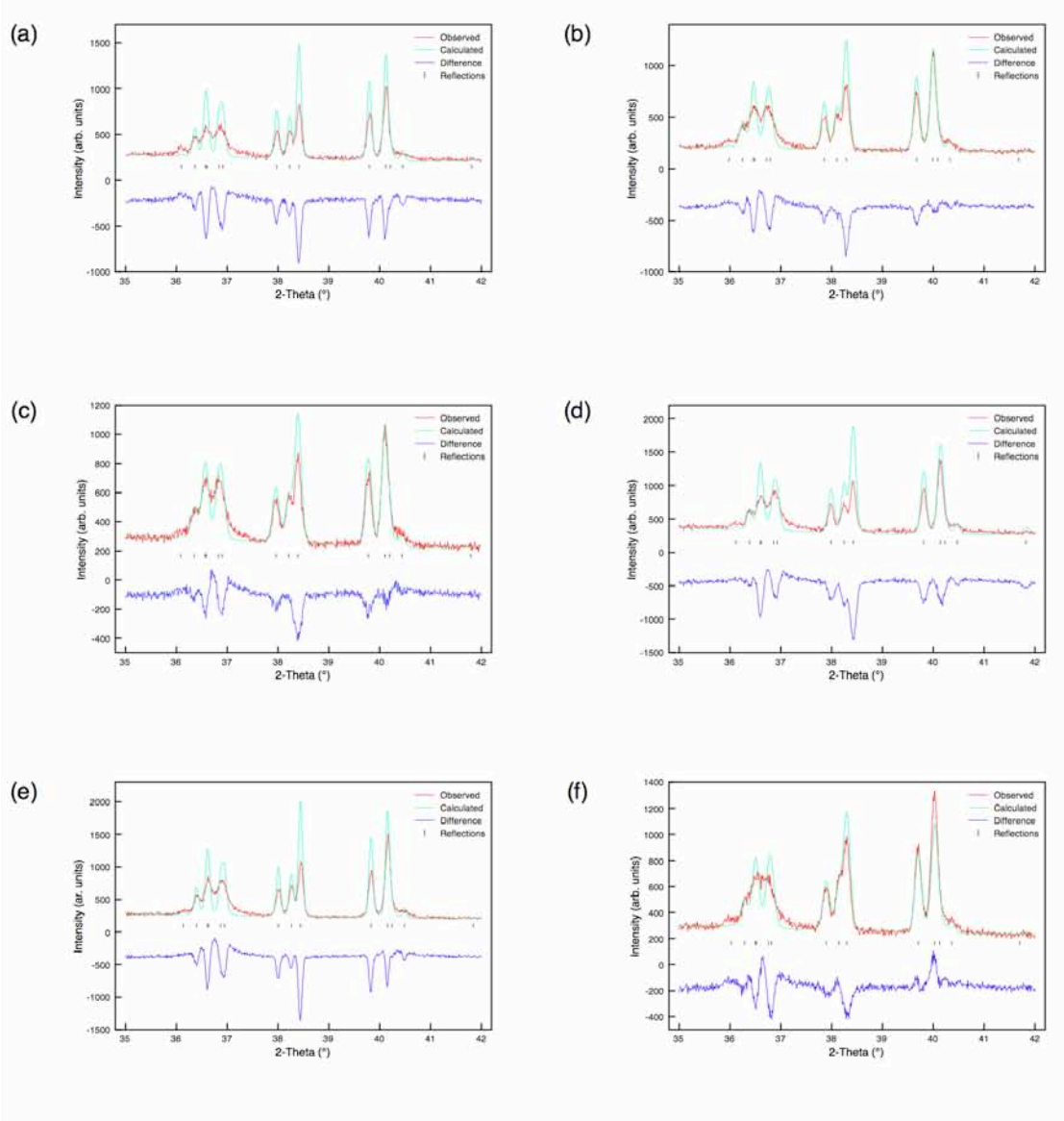

Figure 3.18: Rietveld profiles of l-PXRD data for molten salt $NaNbO_3$ with annealing temperatures of (a) 850 °C, (b) 900 °C, (c) 950 °C, (d) 1000 °C, (e) 1050 °C and (f) 1100 °C. In each case, the annealing time was fixed at 24 hours. Each refinement is consistent with the presence of single phase Pbcm $NaNbO_3$.

microstructure observed in each of the samples synthesised using molten salt methods an expansion of an SEM image is shown in Figure 3.22. The image clearly displays well-defined cubes and further highlights the exceptionally high crystallinity observed in each sample. Initially temperature was the sole variable in the systematic study completed, investigating the range between 850 °C and 1100 °C with annealing times fixed at 24 hours. Using Rietveld refinement all l-PXRD data in this range

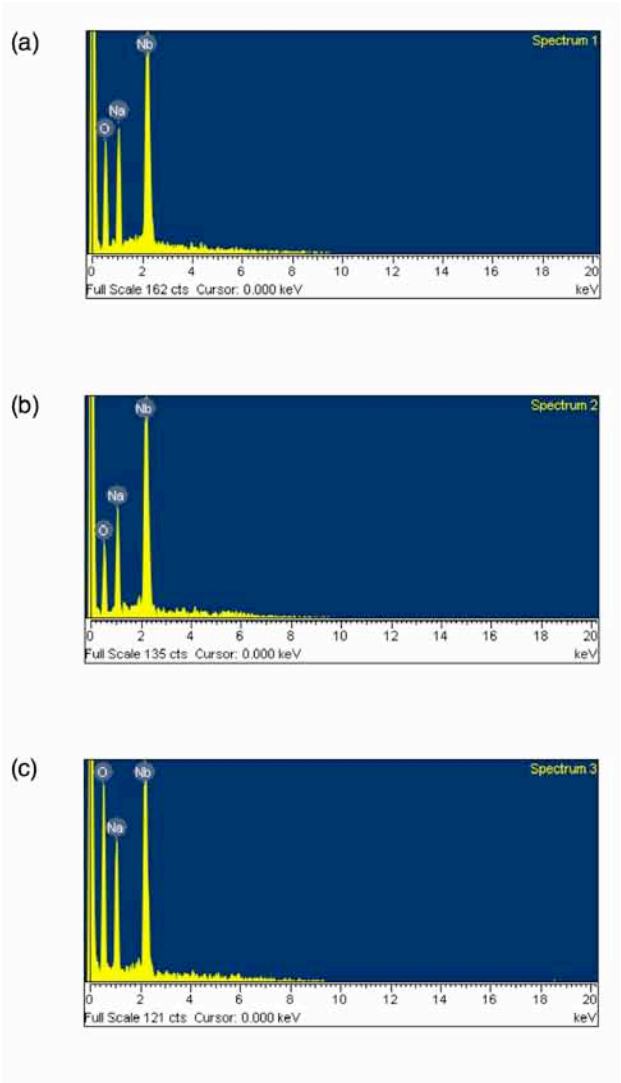

Figure 3.19: EDX spectra obtained for molten salt $NaNbO_3$ (synthesised using 1000 °C for 24 hours). All spectra indicate there is no residual Cl^- present from the molten salt synthesis process.

refined well to the Pbcm model. All Rietveld refinements completed for each sample in this heating series are shown in Figure 3.18(a-f). However, two-dimensional ^{23}Na NMR data highlighted the presence of an additional phase which consistently correlated with that identified in the initial molten salt sample synthesised. Via a systematic temperature study it was possible to eliminate this secondary phase entirely using a temperature of 1000 °C, as shown in Figure 3.21(d). However, at higher temperatures a reduction in crystallinity was observed. This is perhaps clearer to see in Figure 3.23 where the isotropic projections from each two-dimensional spectrum are compared. All two-dimensional ^{23}Na MQMAS NMR spectra

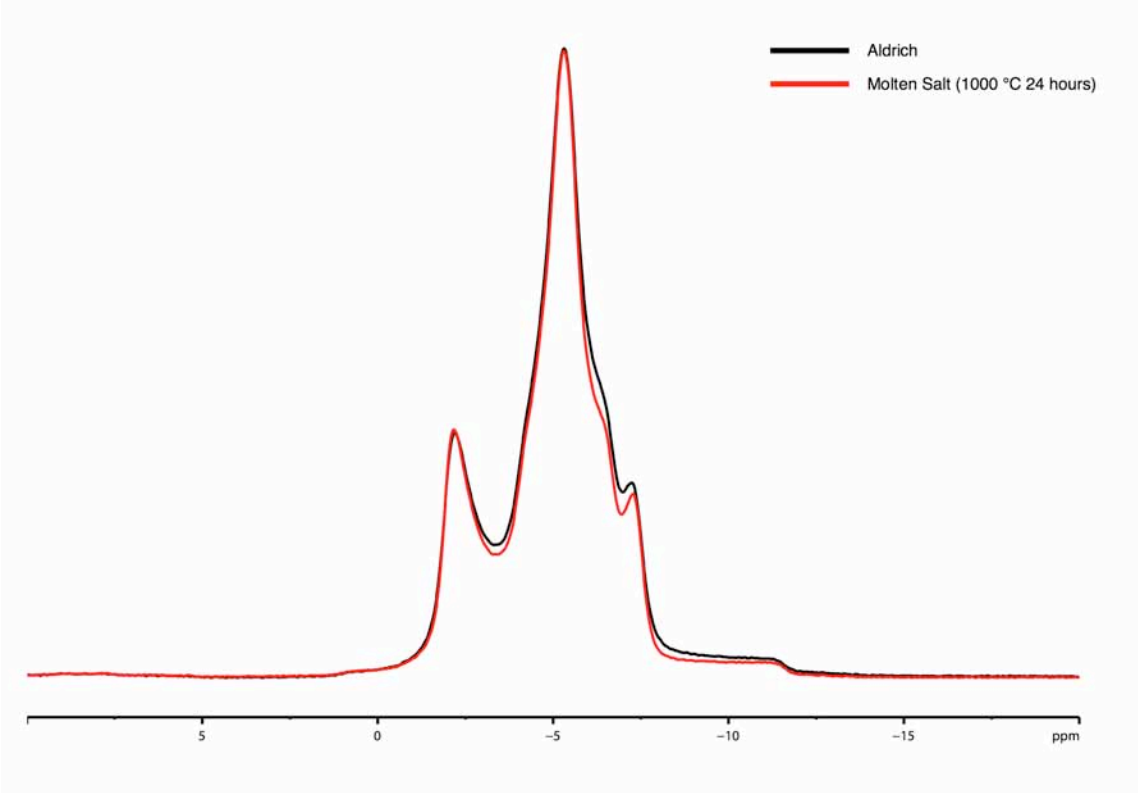

Figure 3.20: Overlay of ^{23}Na (14.1 T) MAS NMR spectra for phase pure sample $NaNbO_3$ (Aldrich) and a molten salt sample of $NaNbO_3$.

recorded for each sample in this series are shown in Figures 3.21(a-f). In addition, heating times between 3 and 48 hours were tested on reactions using 1000 °C. Rietveld refinement of all data in this series indicated excellent agreement with the literature, again suggesting the presence of single phase Pbcm $NaNbO_3$, and once again it was not possible to trace either the presence or quantity of any impurity phase using solely diffraction. All Rietveld refinements completed for each sample in this particular series are shown in Figures 3.24(a-f). Samples prepared using shorter reaction times displayed an abundance of the second phase previously identified in the temperature-dependent study. However, it was possible to eradicate the phase after 24 hours of heating to leave solely the Pbcm phase of $NaNbO_3$. Samples with longer annealing times confirmed this trend, indicating the second phase did not return to the sample and the phase produced was thermodynamically stable. Using ^{23}Na MQMAS the presence and relative quantities of second phase were

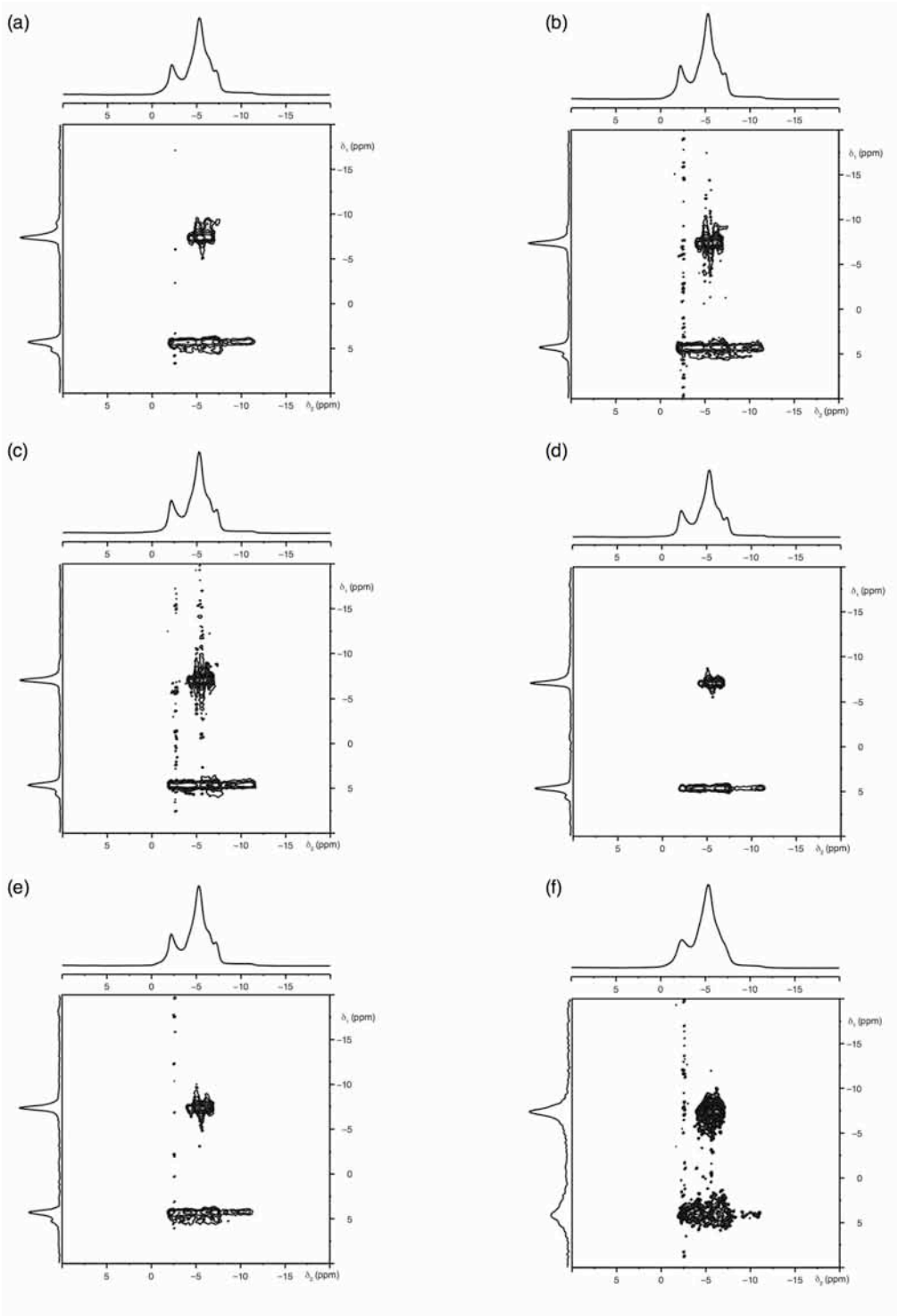

Figure 3.21: Conventional ^{23}Na (14.1 T) MAS NMR spectra, triple-quantum ^{23}Na MAS NMR spectra and corresponding isotropic projections, for molten salt $NaNbO_3$ with annealing temperatures of (a) 850 °C, (b) 900 °C, (c) 950 °C, (d) 1000 °C, (e) 1050 °C and (f) 1100 °C. In each case the annealing time was fixed at 24 hours. Small quantities of the secondary phase are observed in (a-c). This phase is fully removed in (d-f) however poor crystallinity is observed in (f) owing to high reaction temperatures and fast precipitation rates.

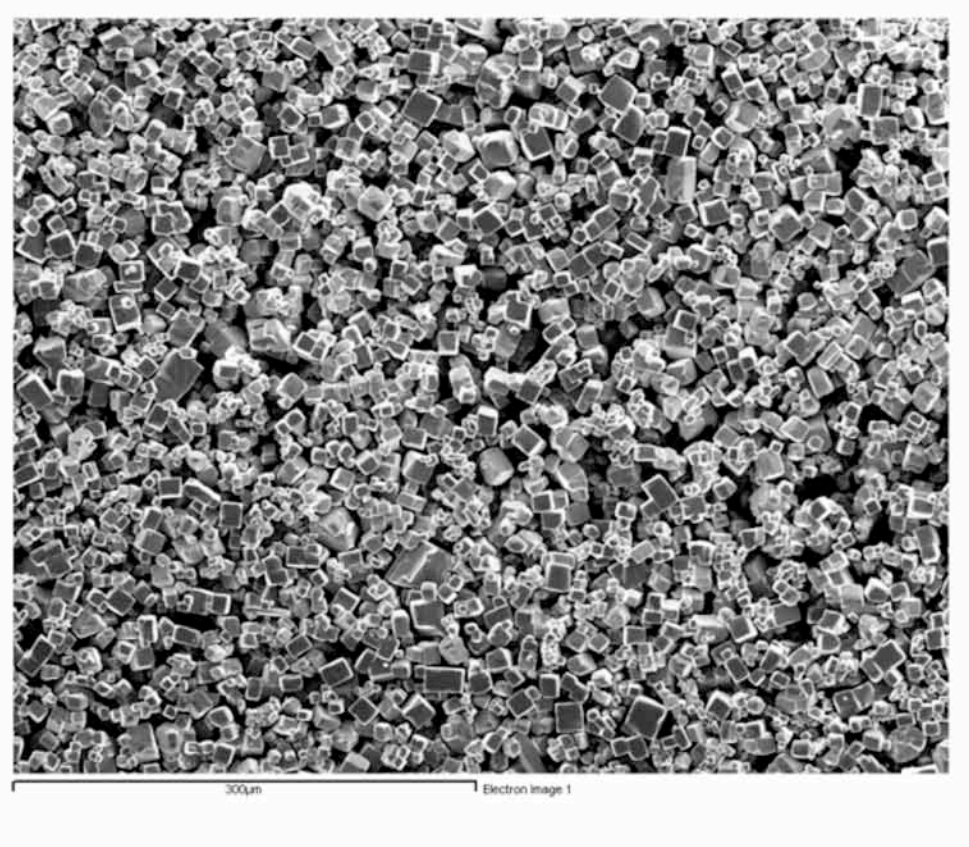

Figure 3.22: An expansion of an SEM image of a molten salt sample of $NaNbO_3$. This highlights the cube-like microstructure adopted by samples synthesised using these methods.

clearly visible, as shown in Figure 3.25. This is perhaps more easily observed by inspection of the isotropic projections shown in Figure 3.23(b). Full refinement details for both heating series are given in Appendix II.

Two phases were consistently synthesised using molten salt techniques, however both temperature and time appeared to affect the formation of the second phase. In the case of our molten salt reactions it was possible to determine the exact temperature and time of reaction required to fully eradicate the second phase. For solid-state reactions, however, this does not appear to be the case. The synthetic conditions alter the proportions of the two phases present, but it is not possible to remove either entirely. Even when reactions were carried out with

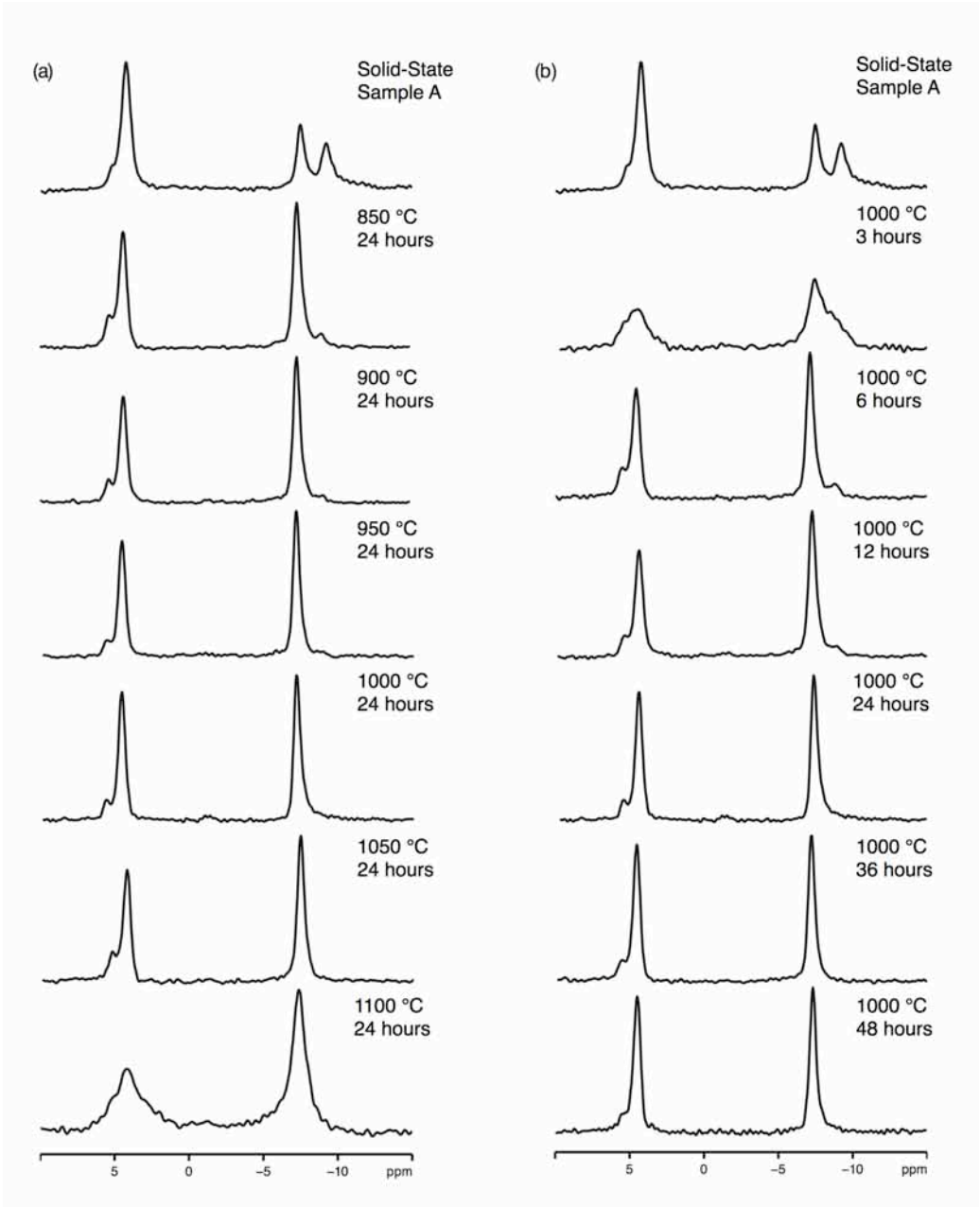

Figure 3.23: Isotropic projections obtained from triple-quantum ^{23}Na (14.1 T) MAS NMR spectra of molten salt samples of $NaNbO_3$. In (a), annealing temperature was varied from 850 °C to 1100 °C, with a fixed annealing time of 24 hours. In (b), the annealing time was varied from 3 to 48 hours, with a fixed annealing temperature of 1000 °C. For comparison the isotropic projection for Solid-State Sample A of $NaNbO_3$ is also shown.

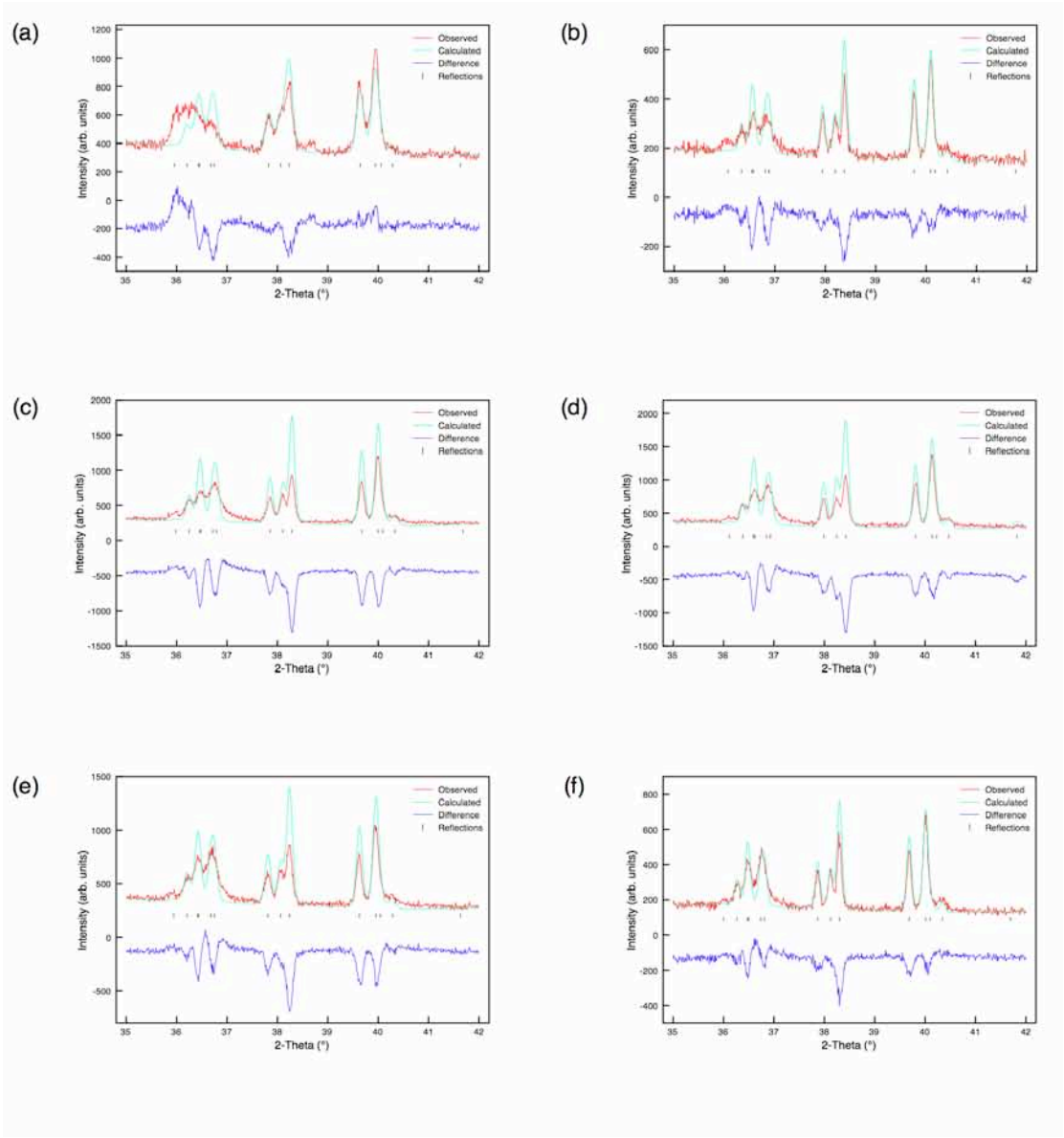

Figure 3.24: Rietveld profiles of l-PXRD data for molten salt $NaNbO_3$ with annealing times of (a) 3 hours, (b) 6 hours, (c) 12 hours, (d) 24 hours, (e) 36 hours and (f) 48 hours. In each case the annealing temperature was fixed at 1000 °C. Each refinement is consistent with the presence of single phase Pbcm $NaNbO_3$.

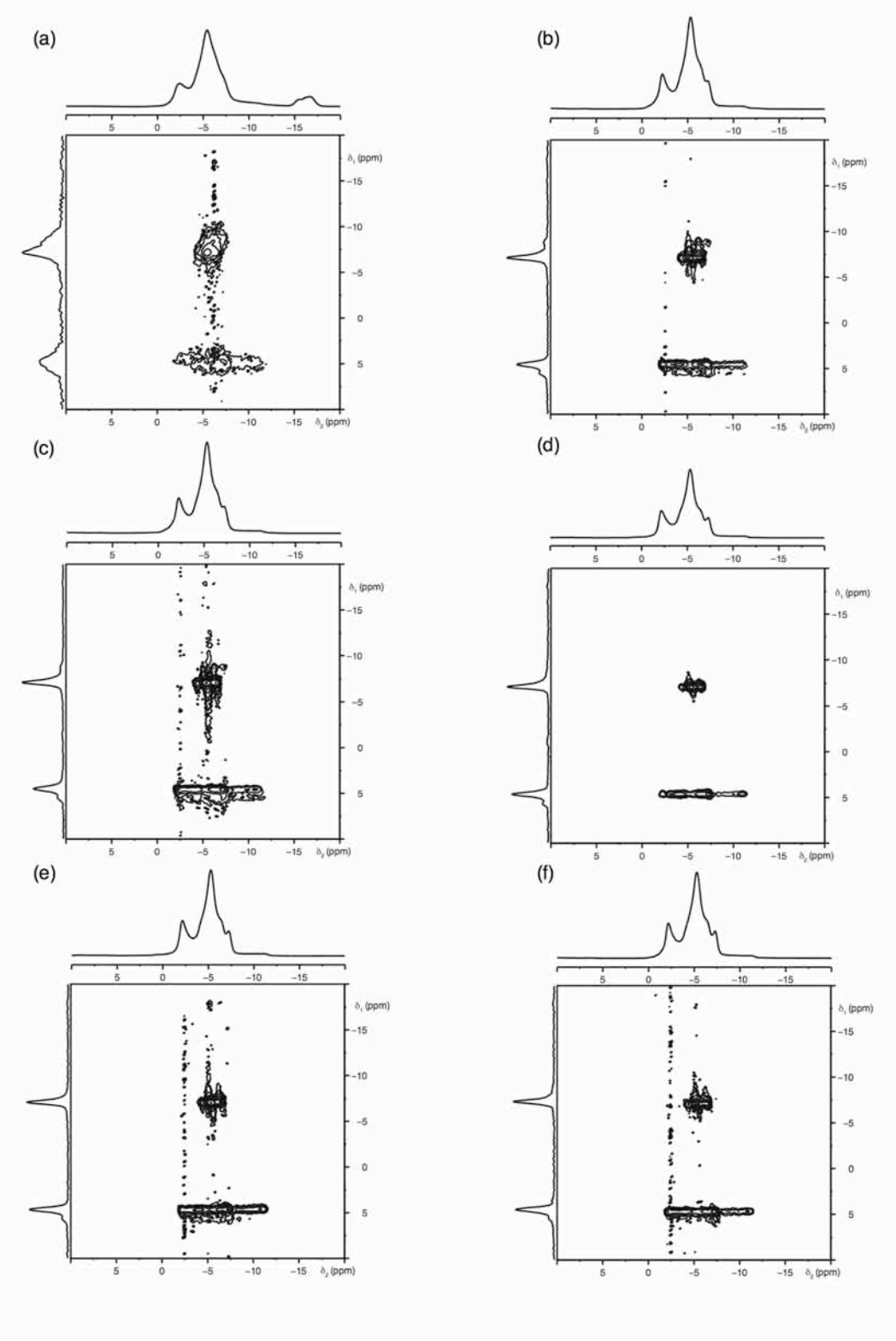

Figure 3.25: Conventional ^{23}Na (14.1 T) MAS NMR spectra, triple-quantum ^{23}Na MAS NMR spectra and corresponding isotropic projections for molten salt $NaNbO_3$, with annealing times of (a) 3 hours, (b) 6 hours, (c) 12 hours, (d) 24 hours, (e) 36 hours and (f) 48 hours. In each the annealing temperature was fixed at 1000 °C. Small quantities of the secondary phase are observed in (a-c) however this phase is fully removed in (d-f).

apparently similar conditions the proportions of the two phases obtained varied. In both solid-state and molten salt reactions the major polymorph formed was the Pbcm phase, although the proportion of the second phase was as high as ~50% in some solid-state syntheses. However, by means of a molten salt approach it was possible to synthesise phase pure Pbcm $NaNbO_3$. Unfortunately, this provides little or no assistance in determining the precise nature of the second phase, although it does, however, provide valuable information regarding reaction mechanism.

3.3.4 Sol-Gel Preparation

In order to use a diverse range of synthetic routes, and to clarify the nature of the second polymorph present in the solid-state preparations, a sol-gel approach was also utilised. In a similar manner to molten salt techniques this allows intimate mixing and reaction of the starting reagents. Conventionally, solid-state methods are adopted over sol-gel processes for the synthesis of perovskites owing, principally, to the simplicity of the reaction. However, occasionally sol-gel methods are favoured as they can enable alternative phases to form which are not commonly observed within solid-state reactions. In contrast to solid-state methods, sol-gel techniques utilise considerably lower temperatures during synthesis. However, an associated disadvantage of these processes, particularly in the case of $NaNbO_3$, is the severe lack of control and reproducibility.

Using a basic sol-gel approach a sample of $NaNbO_3$ was synthesised and structure and phase purity were studied using PXRD. It was immediately apparent a different polymorph of $NaNbO_3$ had been synthesised than the commonly formed orthorhombic Pbcm phase. Rietveld refinement of l-PXRD data (Figure 3.26(a)) highlighted differences in the superstructure peaks ($2\theta = 34° – 42°$), as shown in Figure 3.26(b), in which the theoretical model (Pbcm) placed intensity where no observed experimental data appeared. The presence of a different polymorphic form of $NaNbO_3$ was confirmed using s-PXRD and NPD. Close examination of the high-resolution diffraction data revealed the

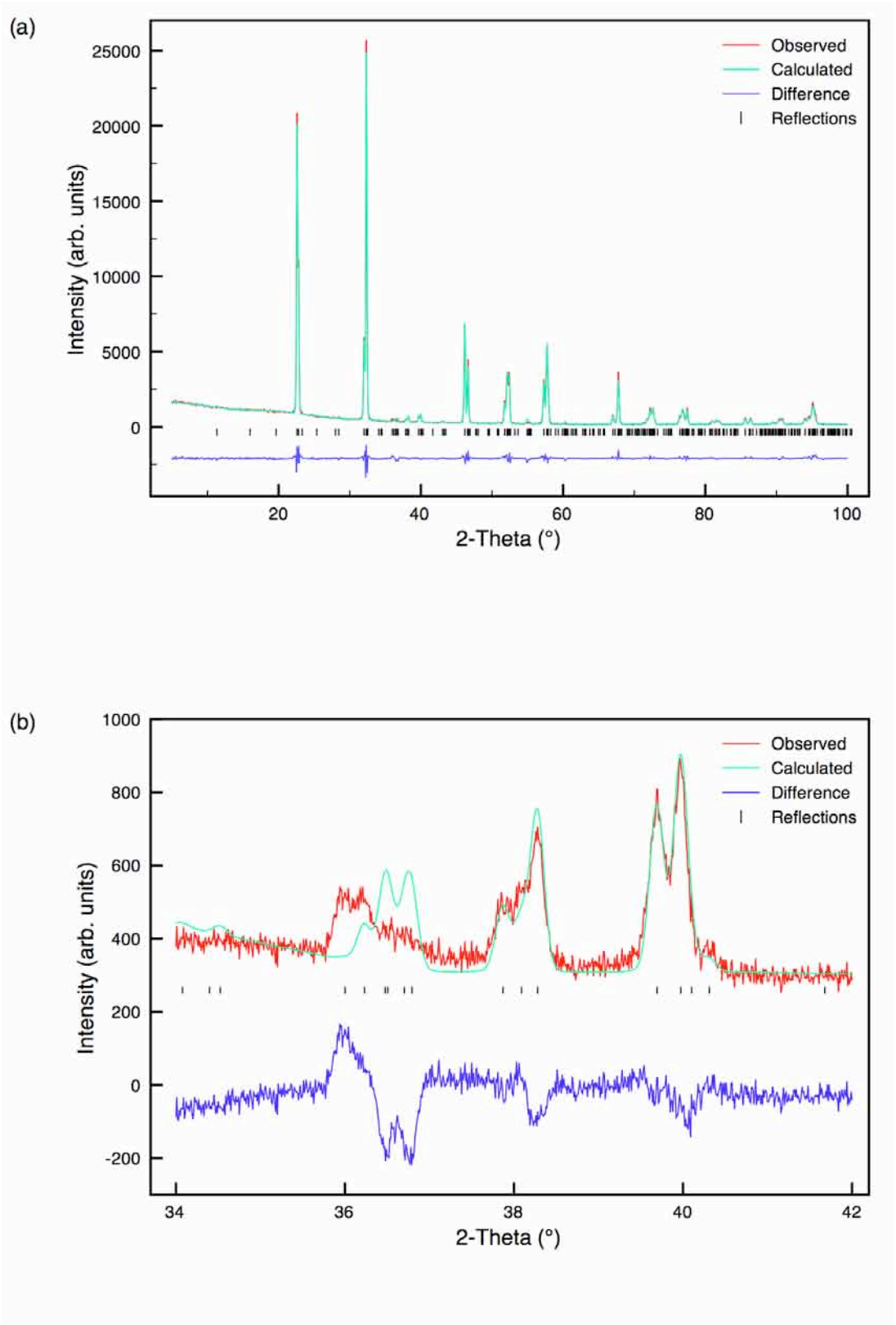

Figure 3.26: Sol-gel $NaNbO_3$ (a) Rietveld profile (Pbcm model) of l-PXRD data and (b) corresponding expansion of the superstructure peaks (2θ = 35° – 45°) highlighting areas of discrepancy.

disappearance of the peaks due to the $4a_p$ superlattice, thereby indicating the phase present did not require additional doubling of the unit cell, as in Pbcm, merely the $\sqrt{2}a_p \times \sqrt{2}a_p \times 2a_p$ cell. This type of distortion in perovskites is well known (in fact it corresponds to the most common tilt system $a^-a^-b^+$). A standard structural model for the centrosymmetric orthorhombic space group Pnma was sufficient to index all peaks, and each dataset refined reasonably well to this model, as shown in Figure 3.27. Refinement details for the NPD data (using both isotropic and anisotropic temperature factors) can be found in Tables 3.6 and 3.7. The Rietveld refinement completed using the s-PXRD data is shown in Figure 3.27(b). Full refinement details are given in Appendix II.

Using conventional ^{23}Na MAS NMR a different and broadened lineshape was observed, which appeared to have lost many of the sharp, distinct features previously identified in the commercially purchased sample. This can be seen in Figures 3.5(a) and (f), where the two lineshapes are compared. To further highlight the differences in lineshape exhibited as a function of synthesis method a comparison of all ^{23}Na MAS NMR spectra recorded at varying fieldstrengths (9.4 T, 14.1 T and 20 T) is shown in Figure 3.28. The two-dimensional ^{23}Na MQMAS NMR spectrum recorded for the sol-gel sample also confirmed the presence of a different phase of $NaNbO_3$ in addition to a small percentage (~10%) of the Pbcm phase (Figure 3.29). It was evident this new phase contained two crystallographically distinct Na sites with δ_1 values of −7.1 ppm and 13.5 ppm, thereby contradicting the conclusions initially drawn from diffraction data alone. The NMR parameters extracted from this spectrum are given in Table 3.2. Although providing an adequate refinement to both the synchrotron and neutron data, the presence of only a single distinct Na species for Pnma reveals it would not appear to be the correct model. In addition, when refined anisotropically the oxygen atom O1 did not have a positive definite thermal displacement factor, thereby indicating this model to be incorrect, as highlighted in Table 3.7.

Perovskites frequently favour centrosymmetric structures except when ferroelectric ions are present. Of the many reported polymorphs of $NaNbO_3$ the majority are centrosymmetric with only one confirmed report

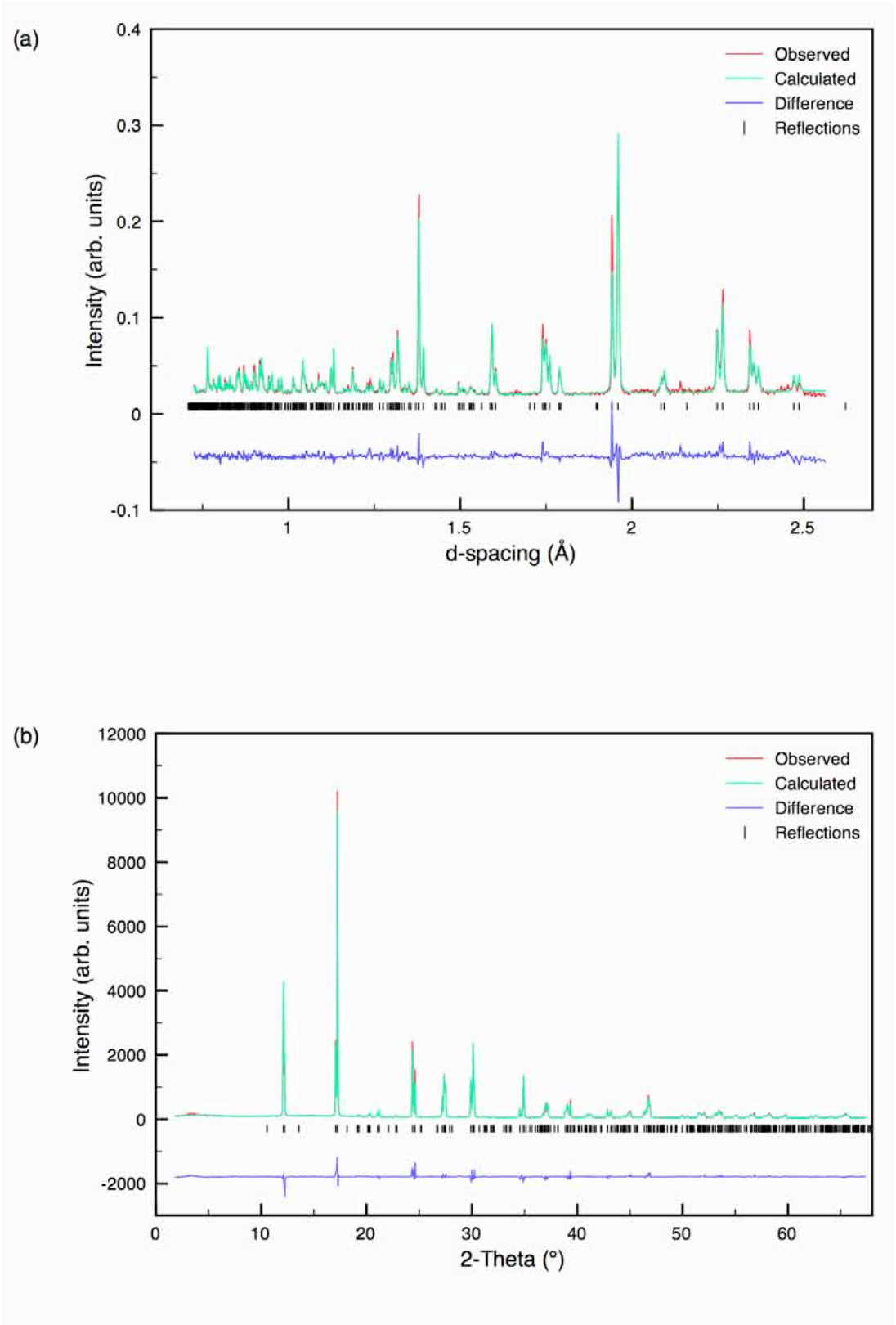

Figure 3.27: Rietveld profiles of (a) NPD and (b) s-PXRD data for sol-gel $NaNbO_3$ using the structural model Pnma. Isotropic thermal parameters were used during refinement of the NPD data.

Table 3.6: Structural parameters for sol-gel $NaNbO_3$ from NPD data, using isotropic thermal factors. Space group Pnma, a = 5.57068(10) Å, b = 7.76621(14) Å, c = 5.51329(10) Å and V = 238.522(11) Å^3. χ^2 = 5.8, wR_p = 7.3% and R_p = 6.6%.

Atom	Site	x	y	z	U(iso) × 100 / Å^2
Na1	4c	0.4958(8)	0.25	0.0026(7)	1.64(5)
Nb1	4a	0	0	0	0.31(4)
O1	4c	0.5111(4)	0.25	0.5619(3)	0.57(4)
O2	8d	0.2158(2)	0.0308(1)	0.2817(2)	1.46(4)

of a non-centrosymmetric structure, that by Shuvaeva *et al.*,[228] obtained from single crystal diffraction. Both the neutron and ^{23}Na NMR data presented suggested the newly synthesised polymorph of $NaNbO_3$ had undergone a reduction in symmetry from the centrosymmetric space group Pnma to a non-centrosymmetric structure. Therefore, to provide further support for this, the nonlinear optic (NLO) properties of selected $NaNbO_3$ samples were tested. Second Harmonic Generation (SHG) experiments are a relatively simple and effective way of identifying whether a structure is centrosymmetric or non-centrosymmetric. SHG measurements were conducted on both the sol-gel sample and a phase pure sample of $NaNbO_3$ (synthesised using molten salt techniques). No response was detected from the phase pure $NaNbO_3$ sample, as shown in Figure 3.30(a). The sol-gel sample displayed an intense SHG active (green) signal, Figure 3.30(b), indicating it to be non-centrosymmetic. This, in conjunction with the ^{23}Na NMR data, provided a significant step towards structural characterisation and allowed identification of three potential non-centrosymmetric subgroups of Pnma; $P2_1ma$, $Pn2_1a$ and $Pnm2_1$. Rietveld refinements were completed for each potential space group using the NPD data collected, although it should be noted that the $Pn2_1a$ model also possesses only a single Na site. Interestingly, the work by Shuvaeva and co-workers was the result of an electric field induced phase transition from Pbcm to $P2_1ma$ in a single crystal of $NaNbO_3$. This polymorph was also recently reported by Waser *et al.*,[226,229] as existing in submicron powders of $NaNbO_3$. Their work suggests $NaNbO_3$ undergoes

Table 3.7: Structural parameters for sol-gel $NaNbO_3$ from NPD data using anisotropic thermal factors. Space group Pnma, a = 5.57067(10) Å, b = 7.76626(12) Å, c = 5.51354(9) Å and V = 238.534(10) Å^3. $\chi^2 = 4.6$, $wR_p = 6.5\%$ and $R_p = 6.2\%$.

Atom	Site	x	y	z	$U_{11} \times 100/Å^2$	$U_{22} \times 100/Å^2$	$U_{33} \times 100/Å^2$
Na1	4c	0.4973(9)	0.25	0.0025(7)	2.94(11)	1.02(9)	2.12(12)
Nb1	4a	0	0	0	0.90(5)	0.39(6)	0.48(6)
O1	4c	0.5091(5)	0.25	0.5600(3)	2.60(9)	−0.11(6)	0.98(7)
O2	8d	0.2172(2)	0.0301(1)	0.2838(2)	2.72(7)	0.93(6)	2.18(7)

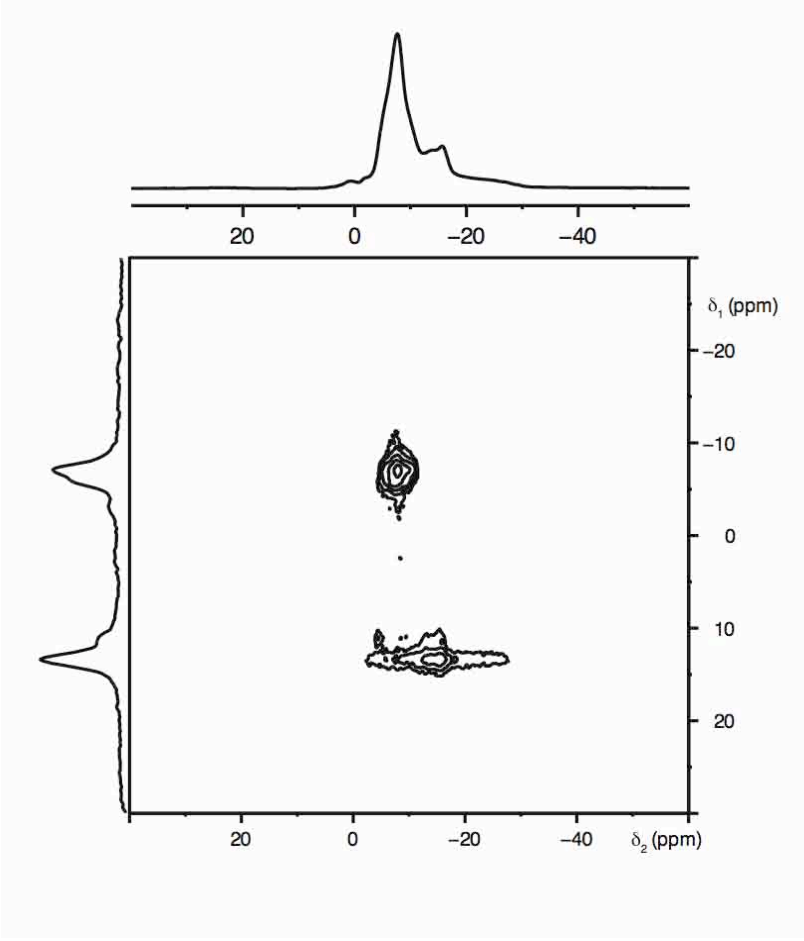

Figure 3.28: Conventional ^{23}Na (9.4 T) MAS NMR spectrum, triple-quantum MAS NMR spectrum, and corresponding isotropic projection for sol-gel sample of $NaNbO_3$.

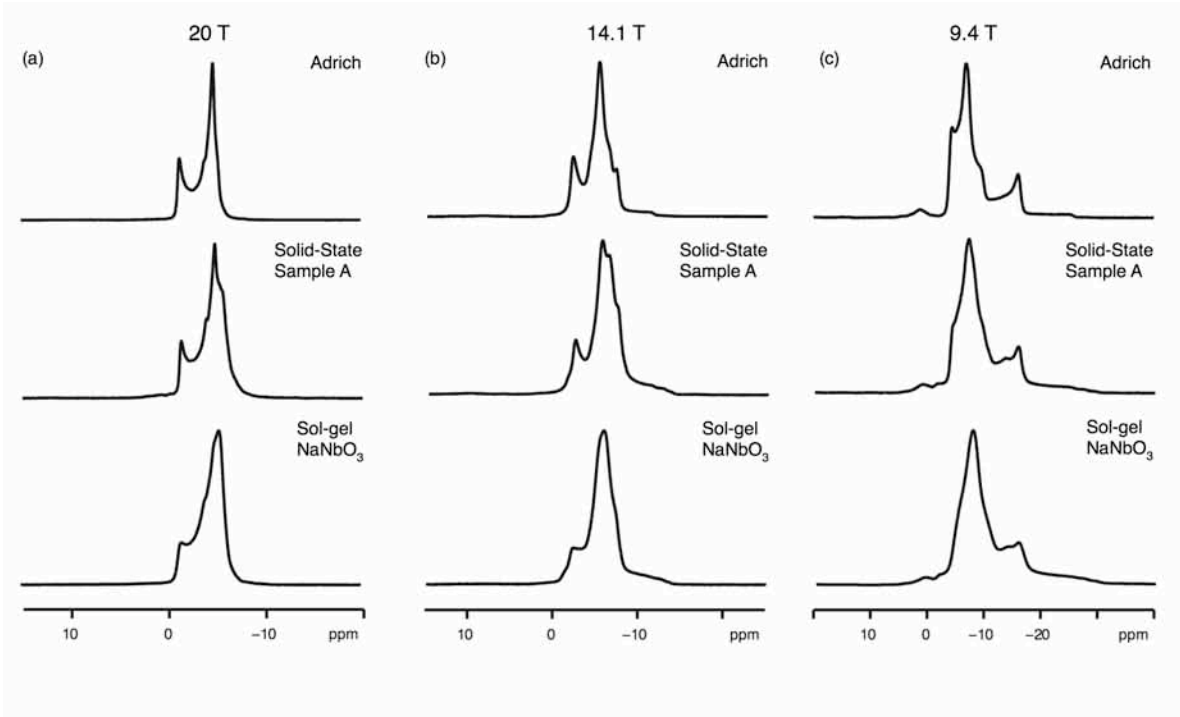

Figure 3.29: Comparison of conventional ^{23}Na MAS NMR spectra for commercial $NaNbO_3$ (Aldrich), Solid-State Sample A $NaNbO_3$ and sol-gel $NaNbO_3$ recorded at (a) 20 T, (b) 14.1 T and (c) 9.4 T. This highlights the change in lineshape observed with varying fieldstrength. The MAS rate was 14 kHz.

a particle size induced phase transition from Pbcm to Pmma via the orthorhombic phase $Pmc2_1$ (alternative setting $P2_1ma$). Using microemulsion-mediated synthetic techniques nanosized powders were synthesised and annealed at various temperatures, producing a range of micron, submicron and nano-ordered powders. In a later publication Waser *et al.*, investigated similar temperature and pressure induced phase transitions for submicron powders of $NaNbO_3$ and identified a similar submicron sample to that previously synthesised. Using piezoresponse force microscopy (PFM) the sample was confirmed to be noncentrosymmetric and, in turn, suggested the presence of the $Pmc2_1$ polymorph of $NaNbO_3$.[249] Waser concluded that enhanced piezoelectric behaviour was observed for submicron powders, in contrast to much weaker activity observed in micron powders. To date there are no reports of this phase existing in powders of $NaNbO_3$ with a larger average particle size distribution.

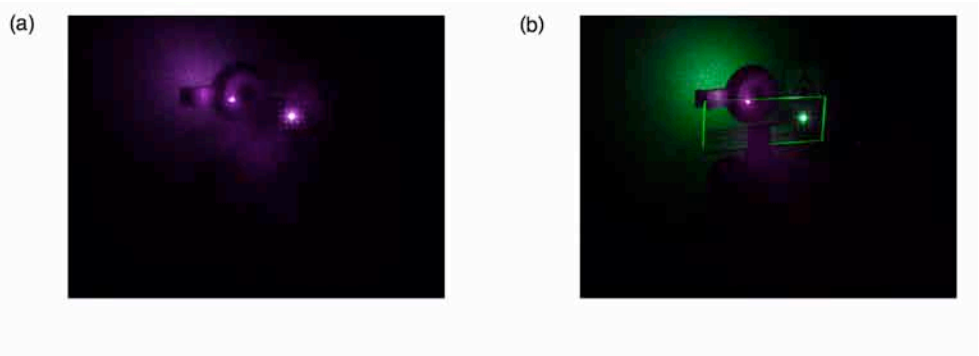

Figure 3.30: Second Harmonic Generation (SHG) measurements for (a) a phase pure sample of Pbcm $NaNbO_3$ synthesised using molten salt techniques (1000 °C for 24 hours) and (b) sol-gel $NaNbO_3$.

Rietveld refinement of the model in space group $P2_1ma$ was undertaken using the model of Shuvaeva.[228] However, structural models for $NaNbO_3$ in space groups $Pn2_1a$ and $Pnm2_1$ were not available in the literature so these were obtained by reduction down in symmetry to the respective space group from Pnma.[107] Rietveld refinement using the space group $P2_1ma$ produced a better fit when compared with $Pn2_1a$ and $Pnm2_1$. All Rietveld refinements can be found in Figures 3.31 – 3.33. Corresponding χ^2 values for the Pnma, $P2_1ma$, $Pn2_1a$ and $Pnm2_1$ Rietveld refinements are 5.8, 4.8, 5.6 and 7.9 respectively. The $Pn2_1a$ model possesses only a single Na site and can therefore be excluded. All structural parameters obtained from each refinement are given in Tables 3.8 - 3.10. Corresponding bond lengths are given in Appendix II. When refined in $Pnm2_1$ extremely high isotropic thermal parameters were obtained, thereby clearly indicating this not to be the correct structure. $P2_1ma$ provides the best agreement with the experimental data.

At no stage in this investigation was the sol-gel sample exposed to an electric field, confirming it is feasible to directly synthesise a non-centrosymmetric, polar phase of $NaNbO_3$; however it is extremely difficult to produce a phase pure sample. The Pbcm phase of $NaNbO_3$ is consistently formed within the reaction owing, presumably, to its relative thermodynamic stability. The crystallinity of the sample was also severely reduced when compared with that produced using molten salt and solid-state techniques. The microstructure adopted displayed no regularity,

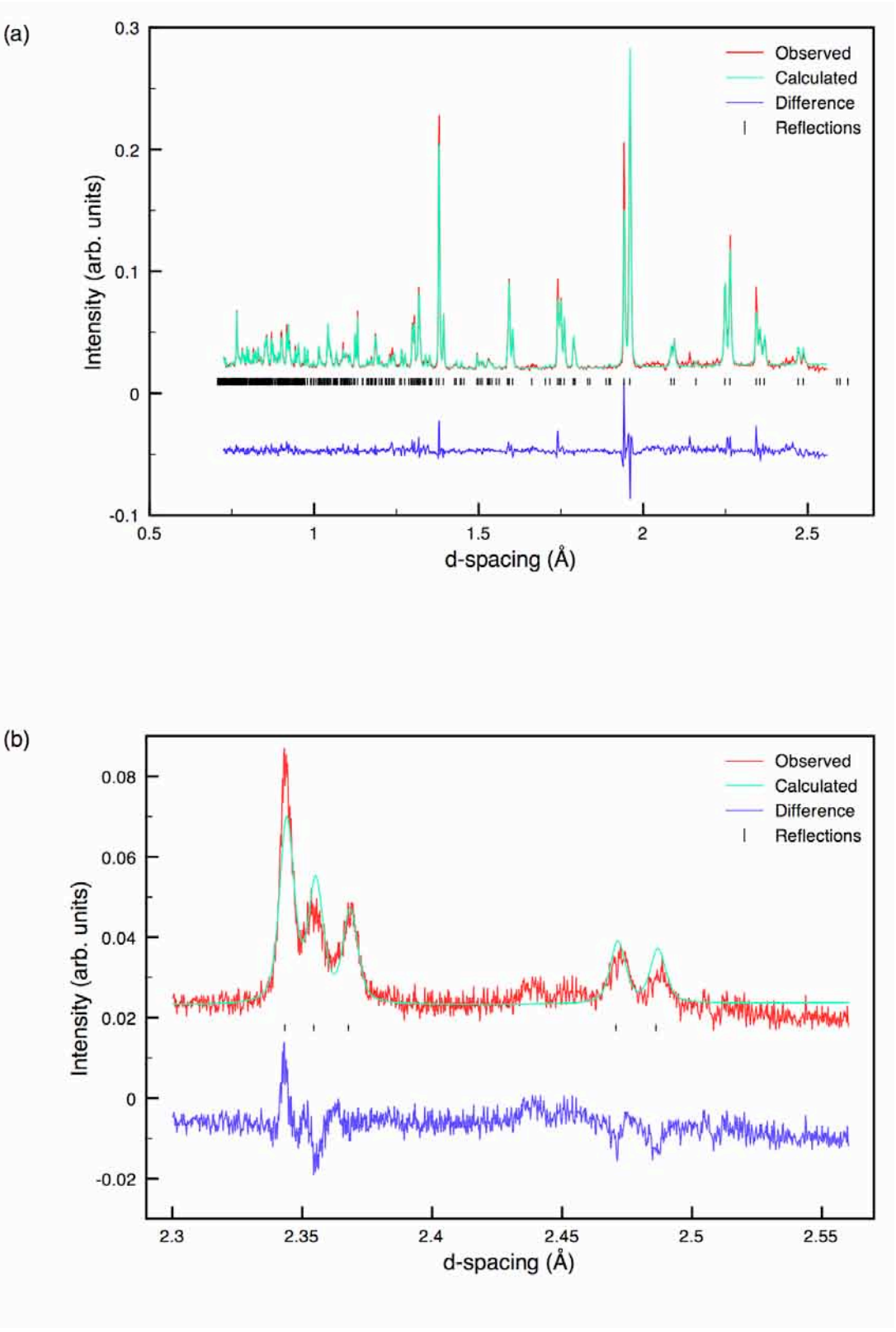

Figure 3.31: Rietveld profile of NPD data for sol-gel $NaNbO_3$ using structural model $P2_1ma$. Also shown is a corresponding expansion of the superstructure peaks (2.3 Å – 2.55 Å). Isotropic thermal parameters were used during the Rietveld refinement.

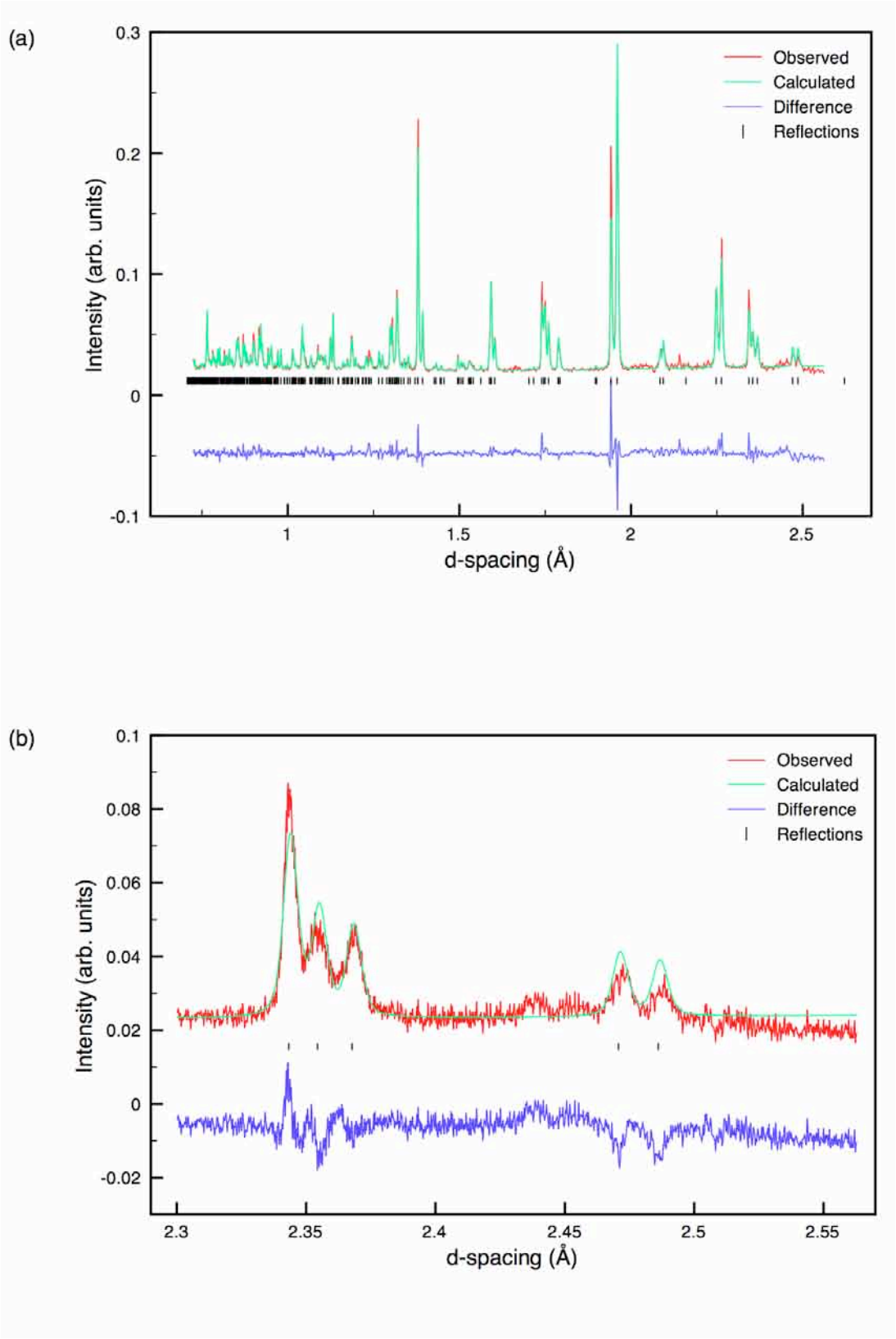

Figure 3.32: Rietveld profile of NPD data for sol-gel $NaNbO_3$ using structural model $Pn2_1a$. Also shown is a corresponding expansion of the superstructure peaks (2.3 Å – 2.55 Å). Isotropic thermal parameters were used during the Rietveld refinement.

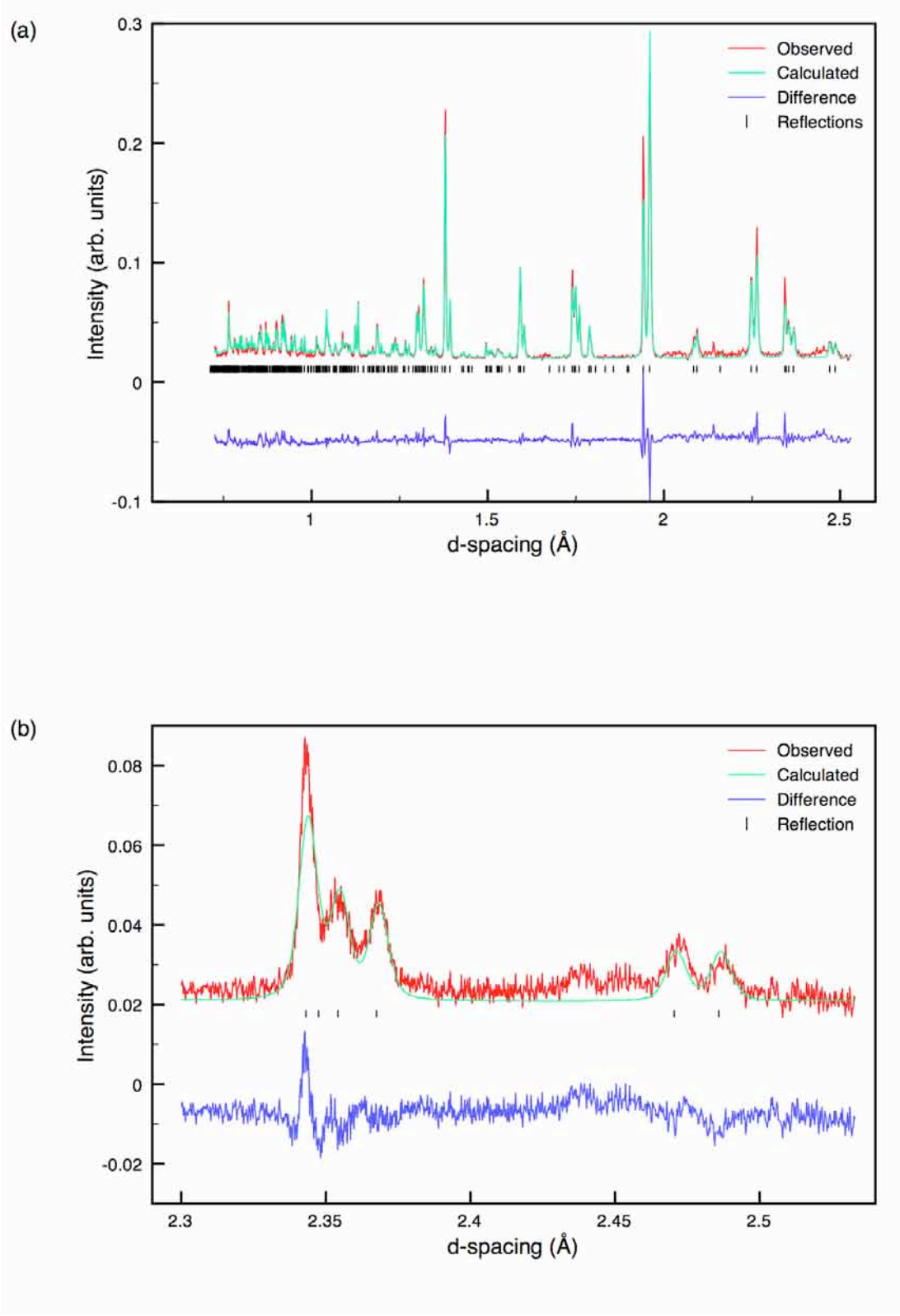

Figure 3.33: Rietveld profile of NPD data for sol-gel $NaNbO_3$ using structural model $Pnm2_1$. Also shown is a corresponding expansion of the superstructure peaks (2.3 Å – 2.55 Å). Isotropic thermal parameters were used during the Rietveld refinement.

Table 3.8: Structural parameters for sol-gel $NaNbO_3$ from NPD data, using isotropic thermal factors. Space group $P2_1ma$, a = 5.57070(9) Å, b = 7.76623(12) Å, c = 5.51331(9) Å and V = 238.524(10) Å^3. χ^2 = 4.8, wRp = 6.6% and Rp = 6.2%.

Atom	Site	x	y	z	U(iso) × 100 / Å^2
Na1	2a	0.2596(11)	0	0.7481(10)	0.50(10)
Na2	2b	0.2915(12)	0.5	0.7327(11)	2.24(15)
Nb1	4c	0.2625	0.2500(5)	0.2466(5)	0.20(4)
O1	2a	0.2409(6)	0	0.3124(11)	0.53(13)
O2	2b	0.2257(5)	0.5	0.1928(11)	0.37(12)
O3	4c	0.0131(7)	0.2790(6)	0.5272(7)	1.84(9)
O4	4c	−0.0490(6)	0.2197(5)	0.0360(6)	0.61(7)

Table 3.9: Structural parameters for sol-gel $NaNbO_3$ from NPD data using isotropic thermal factors. Space group $Pn2_1a$, a = 5.57069(10) Å, b = 7.76625(14) Å, c = 5.51334(10) Å and V = 238.526(11) Å^3. χ^2 = 5.6, wR_p = 7.2% and R_p = 6.6%.

Atom	Site	x	y	z	U(iso) × 100 / Å^2
Na1	4a	0.4952(8)	0.2487(8)	0.0031(7)	1.57(6)
Nb1	4a	0.0022(8)	0.0107(4)	−0.0045(7)	0.23(4)
O1	4a	0.5119(4)	0.2512(6)	0.5609(3)	0.78(5)
O2	4a	0.2044(5)	0.0317(6)	0.2855(8)	1.20(8)
O3	4a	−0.2276(6)	−0.0304(5)	−0.2777(9)	1.44(9)

Table 3.10: Structural parameters for sol-gel $NaNbO_3$ from NPD data using isotropic thermal factors. Space group $Pnm2_1$, a = 5.57022(13) Å, b = 7.76573(17) Å, c = 5.51272(13) Å and V = 238.463(14) Å^3. $\chi^2 = 7.9$, $wR_p = 8.5\%$ and $R_p = 7.8\%$.

Atom	Site	x	y	z	U(iso) × 100 / Å^2
Na1	2a	0.7550(13)	0.5	0.0015(11)	0.34(9)
Na2	2a	−0.226(3)	0	−0.005(3)	7.0(3)
Nb1	4b	0.2462(8)	0.2513(5)	−0.0015(13)	2.02(6)
O1	2a	0.7724(15)	0.5	0.5516(16)	4.8(2)
O2	2a	−0.2528(10)	0	−0.5666(10)	0.91(8)
O3	4b	0.4572(7)	0.2802(6)	0.2927(9)	2.40(9)
O4	4b	0.0178(9)	0.2198(8)	−0.2626(10)	4.74(17)

with a variety of different crystal sizes and morphologies adopted throughout, as illustrated in Figure 3.5(l), in contrast to the regularly repeating cube-like microstructure adopted in the molten salt samples. The reduction in crystallinity is also highlighted by broadening of the ridges observed in the ^{23}Na MQMAS NMR spectrum, Figure 3.28, and in all diffraction patterns collected.

3.3.5 ^{93}Nb MAS NMR

To date the data presented suggests that the ^{23}Na NMR parameters are sensitive to small structural changes. $NaNbO_3$ does, however, possess two additional NMR active nuclei, ^{93}Nb (I = 9/2) and ^{17}O (I = 5/2). The Nb environment in $NaNbO_3$ could potentially provide additional information regarding the different phases present in each sample. Therefore, in an attempt to establish the differences between the two phases the Nb environment of each sample was investigated using ^{93}Nb NMR. ^{93}Nb is a quadrupolar nucleus and, as observed for ^{23}Na, lineshapes commonly exhibit broadening as a result of inefficient removal of the quadrupolar interaction. Niobium-based compounds are known to exhibit large

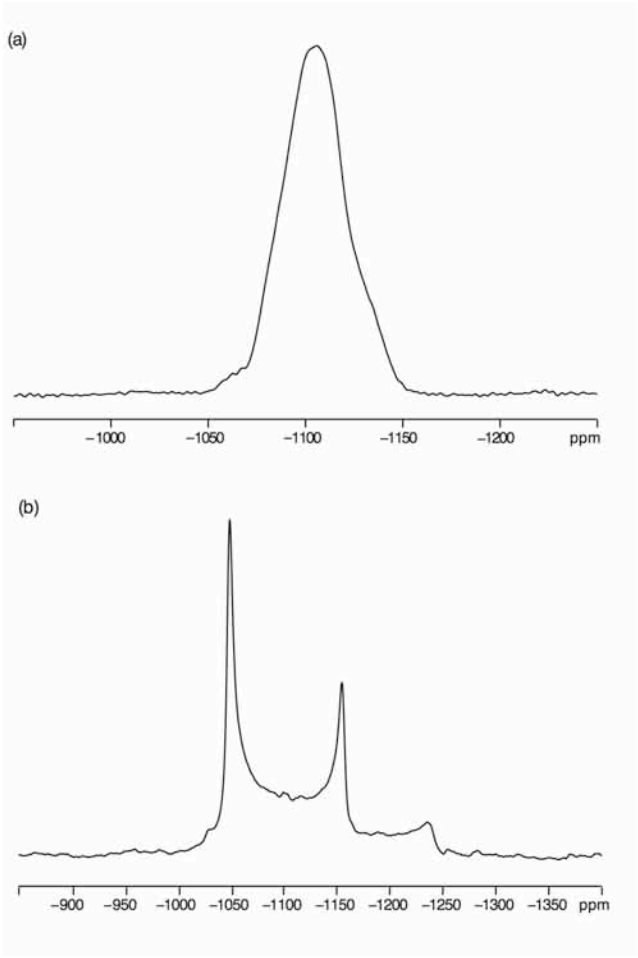

Figure 3.34: Conventional ^{93}Nb (14.1 T) MAS NMR spectra for (a) commercial $NaNbO_3$ (Aldrich) and (b) the ilmenite[225] polymorph of $NaNbO_3$. The MAS rate was 30 kHz.

quadrupolar interactions, commonly on the order of many megahertz and in order to adequately suppress this interaction high-resolution two-dimensional techniques such as MQMAS are required.

The sample purchased commercially (Sigma-Aldrich) was initially investigated and under MAS a broadened lineshape was observed, characteristic of second-order quadrupolar broadening. The MAS spectrum displayed additional broadening of the main features of the lineshape, suggesting the possible presence of disorder within the sample, as shown in Figure 3.34(a). In contrast, the ^{93}Nb MAS NMR spectrum for the ilmenite[225] polymorph of $NaNbO_3$ produces a quadrupolar lineshape characteristic of an ordered Nb environment, as shown in Figure 3.34(b). The two-dimensional ^{93}Nb MQMAS spectrum for the Aldrich sample of $NaNbO_3$ is shown in Figure 3.35(a) and confirms the presence of a single broadened resonance, in good agreement with the literature.[250,251] Full

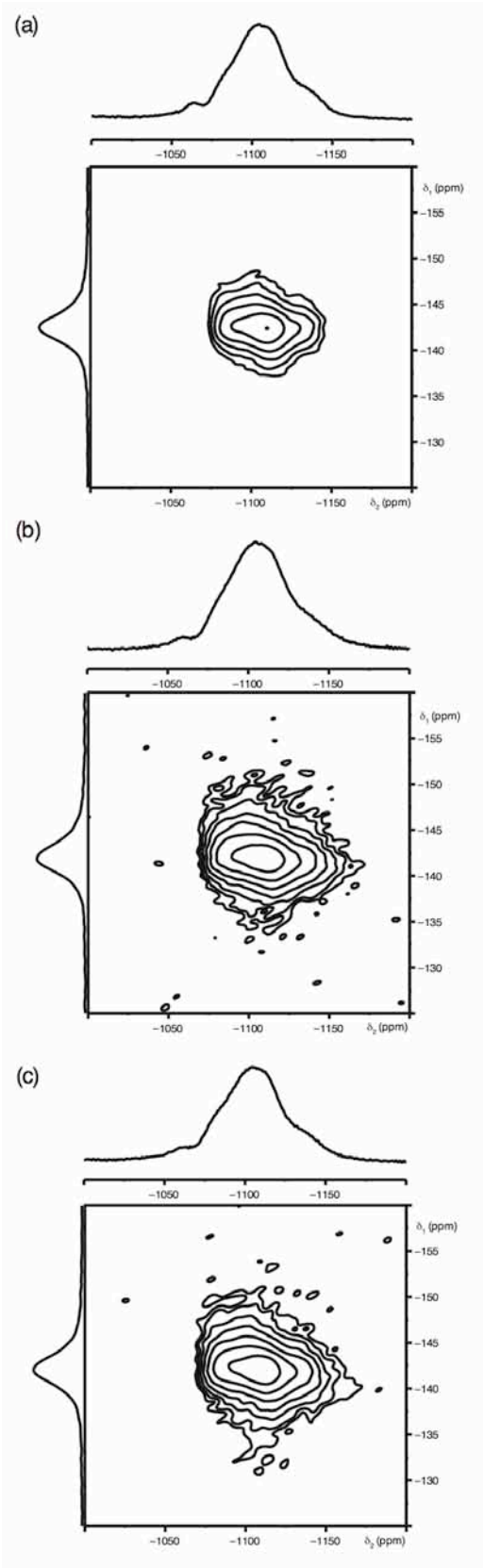

Figure 3.35: Conventional ^{93}Nb (14.1 T) MAS NMR spectrum, triple-quantum MAS NMR spectrum, and corresponding projections for (a) commercial $NaNbO_3$ (Aldrich), (b) Solid-State Sample A $NaNbO_3$ and (c) sol-gel $NaNbO_3$. The MAS rate was 30 kHz.

details of the ^{93}Nb quadrupolar parameters for this sample can be found in Table 3.11. According to diffraction, in single phase Pbcm $NaNbO_3$ the Nb 'on average' lie approximately centrosymmetrically within the octahedra. The ^{93}Nb MAS NMR spectrum however suggests the Nb^{5+} cations exhibit, to some extent, positional disorder, i.e., each Nb is marginally displaced from the centre of the octahedron. This displacement is not detected using diffraction as only the long-range order of a material is examined using diffraction and any subtle movement of the Nb is averaged over this range.

Samples from each of the synthetic methods investigated were also studied using ^{93}Nb MAS and MQMAS NMR, each of which produced similar findings to those for the Aldrich sample. Under MAS each displayed a single broad resonance, indicative of a large second-order quadrupolar broadening. In a similar manner to the Aldrich sample additional broadening of the lineshape was observed in each, again suggesting the presence of positional disorder of the Nb^{5+} cation. The ^{93}Nb MQMAS spectra recorded for the sol-gel sample of $NaNbO_3$ and Solid-State Sample A are shown in Figures 3.35(b) and (c) respectively. Interestingly, when spectra from each were overlaid it became apparent subtle changes were displayed in each depending on synthetic method used, as shown in Figure 3.36. The single resonance observed in phase pure Pbcm $NaNbO_3$ consistently covered a narrow δ_2 shift range when compared with Solid-State Sample A and the sol-gel sample of $NaNbO_3$. There are many possible reasons for this, namely crystallite size, shape, structural stress, strain and other such sample dependent effects.

Using two-dimensional ^{23}Na MAS NMR it was possible to identify the presence of two different phases of $NaNbO_3$ in Solid-State Sample A, believed to be two structurally very closely related polymorphs of $NaNbO_3$. The ^{93}Nb NMR findings presented suggest that it is not possible to distinguish between distinct phases or polymorphs of $NaNbO_3$ using ^{93}Nb MQMAS techniques. This, as a result, suggests the local environment of the Na^+ cation is more sensitive to the subtle structural changes observed in $NaNbO_3$. Close examination of the $NaNbO_3$ structure reveals the Nb is enclosed in NbO_6 units and only marginal movement of the Nb

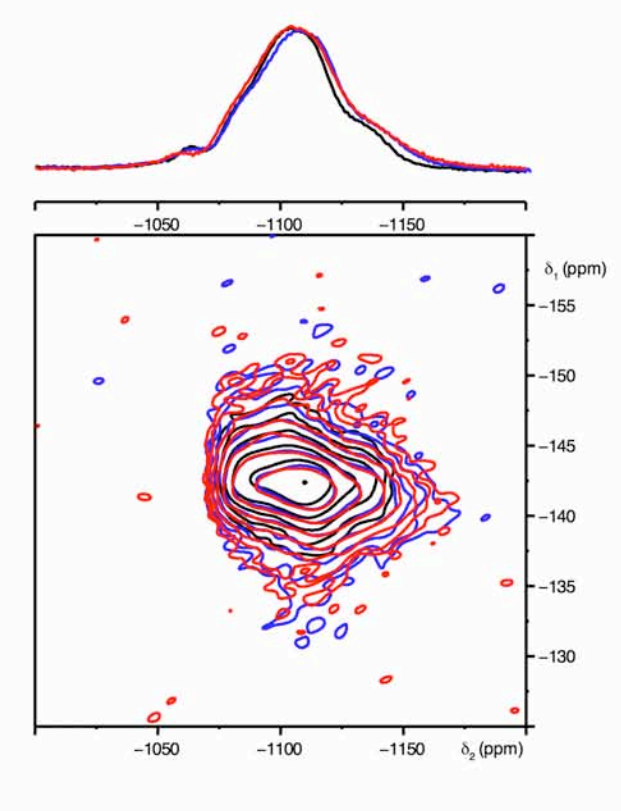

Figure 3.36: ^{93}Nb (14.1 T) MAS NMR spectra, two-dimensional triple-quantum MAS NMR spectra and corresponding isotropic projections of phase pure commercially-purchased $NaNbO_3$ (shown in black), Solid-State Sample A $NaNbO_3$ (shown in blue) and sol-gel $NaNbO_3$ (shown in red).

Table 3.11: ^{93}Nb NMR parameters, δ_{iso}, P_Q, C_Q and η_Q, for commercially purchased $NaNbO_3$ (Aldrich), Solid-State Sample A $NaNbO_3$ and sol-gel $NaNbO_3$ sample, obtained from the MQMAS spectra in Figure 3.35.

	Site	δ_{iso} (ppm)	P_Q / MHz	C_Q / MHz	η_Q
Commercial Sample (Aldrich)					
Pbcm	Nb	−1078.3(5)	21.2(2)	19.6(2)	0.7(1)
Solid-State Sample A					
Pbcm	Nb	−1077.2(5)	21.9(2)	20.3(2)	0.7(1)
Sol-gel Sample					
"$P2_1ma$"	Nb	−1076.6(5)	22.2(2)	20.8(2)	0.6(1)

is possible from the centre of the octahedron. The Na^+ cations, however, possess a considerably greater degree of positional freedom which, presumably, plays a more influential role in the phases of $NaNbO_3$ formed. In addition, the tilting and/or rotation exhibited by the NbO_6 octahedra will also affect the position of the Na^+ cation in the structure and therefore influence the phase(s) produced. The broadened ^{93}Nb MAS lineshapes obtained for each sample hinders the extraction of valuable structural information. Therefore, to aid in obtaining such information static ^{93}Nb NMR spectra were also recorded for each sample using a central-transition selective spin-echo pulse sequence.

3.3.6 Static ^{93}Nb NMR Spectra

Due to the broad nature of quadrupolar lineshapes the time-domain FID is extremely short. Much of the FID is therefore lost during the 'dead time', i.e., the time between the pulse and acquisition. Therefore, to address this problem a 180° pulse is often applied a short time, τ, after the initial pulse. This pulse refocuses evolutions due to all terms that act as offsets, for example chemical shift, dipolar and second-order quadrupolar interactions. At a time τ after the 180° pulse the signal is refocused and acquisition of the whole FID is possible, producing a spectrum free from distortions owing to dead time effects. A schematic representation of a spin-echo pulse sequence (90 - τ - 180) is shown in Figure 3.37.

Under static conditions both the quadrupolar interaction and chemical shift anisotropy are present. Each interaction contributes to the observed lineshape and, when fitted, each can provide valuable information. However, it is often difficult to deconvolute the lineshape and determine the contribution from each of the different sites present. The two interactions are however field dependent. The CSA and quadrupolar interactions are proportional to B_0 and B_0^{-1} respectively. Therefore, resolution may be improved at both higher and lower magnetic fieldstrength. To illustrate the dependency of each interaction with field several lineshapes with different CSA and quadrupolar contributions have

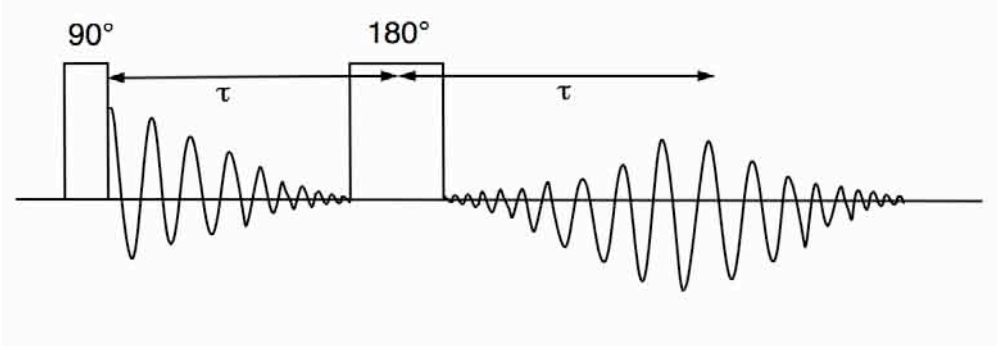

Figure 3.37: Schematic representation of a spin-echo pulse sequence (90 - τ - 180).

been simulated under static conditions at 7 T, 9.4 T, 14.1 T and 20 T using SIMPSON.[252] Figure 3.38(a) exhibits CSA lineshapes possessing $\Delta\sigma_{CS}$ = 75 ppm and η_{CS} = 0 at varying fieldstrengths. The lineshape at 20 T is considerably broadened when compared with that at 7 T. This confirms that the CSA dominates at high field and scales with B_0. In contrast, Figure 3.38(b) displays a quadrupolar lineshape with C_Q = 3 MHz and η_Q = 0. At high field the spectrum is relatively narrow and at low field a much broader resonance is observed. Such behaviour highlights the dominance of the quadrupolar interaction at low field and confirms the interaction is inversely proportional to the field. However, in reality the resonances observed in any solid-state NMR spectrum will possess both a CSA and quadrupolar contribution. Hence, the lineshape observed will depend on the contribution of each interaction to the sample, the fieldstrength used and the relative orientation of the two tensors. In such cases it can be extremely difficult to accurately determine the contribution from each interaction. To highlight how challenging this can be a spectrum possessing C_Q = 3 MHz, η_Q = 0, $\Delta\sigma_{CS}$ = 75 ppm and η_{CS} = 0 has been simulated at varying fieldstrengths and is shown in Figure 3.39. The spectra observed at 7 T and 20 T appear very different owing to the presence of both interactions. For example, the spectrum at low field possesses an obvious quadrupolar lineshape, whereas at high field the lineshape exhibits features characteristic of the CSA. The spectra shown indicate how challenging it would be to accurately determine the values of C_Q and $\Delta\sigma_{CS}$. It is for this reason that spectra are commonly recorded under static conditions at multiple fieldstrengths, as the field dependency of each interaction enables accurate values of each to be obtained. This

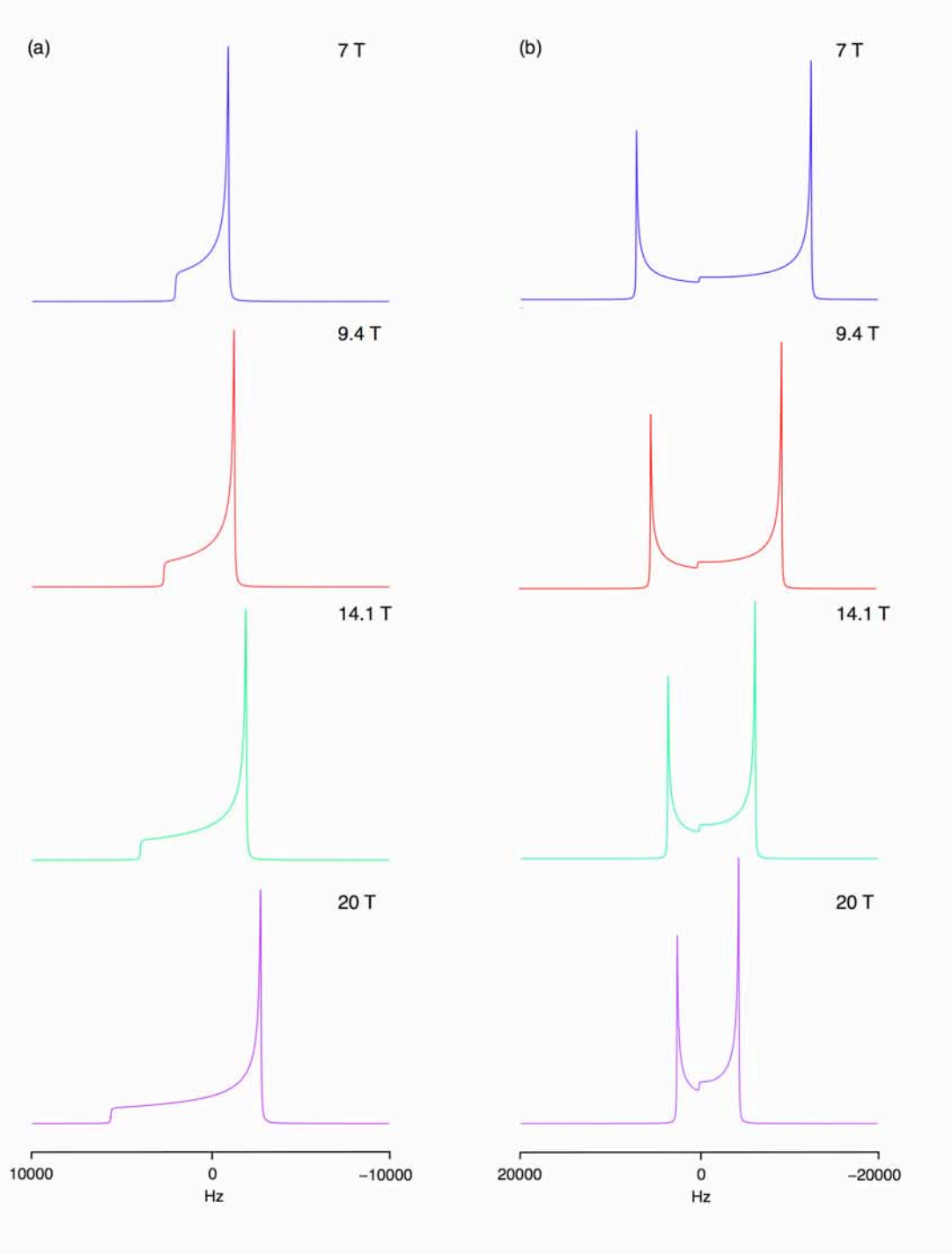

Figure 3.38: Simulated static (a) CSA and (b) second-order quadrupolar lineshapes with varying B_0 fieldstrength. Simulation parameters include (a) $\delta_{iso} = 0$, $\Delta\sigma_{CS} = 75$ ppm, $\eta_{CS} = 0$ and (b) $C_Q = 3$ MHz and $\eta_Q = 0$.

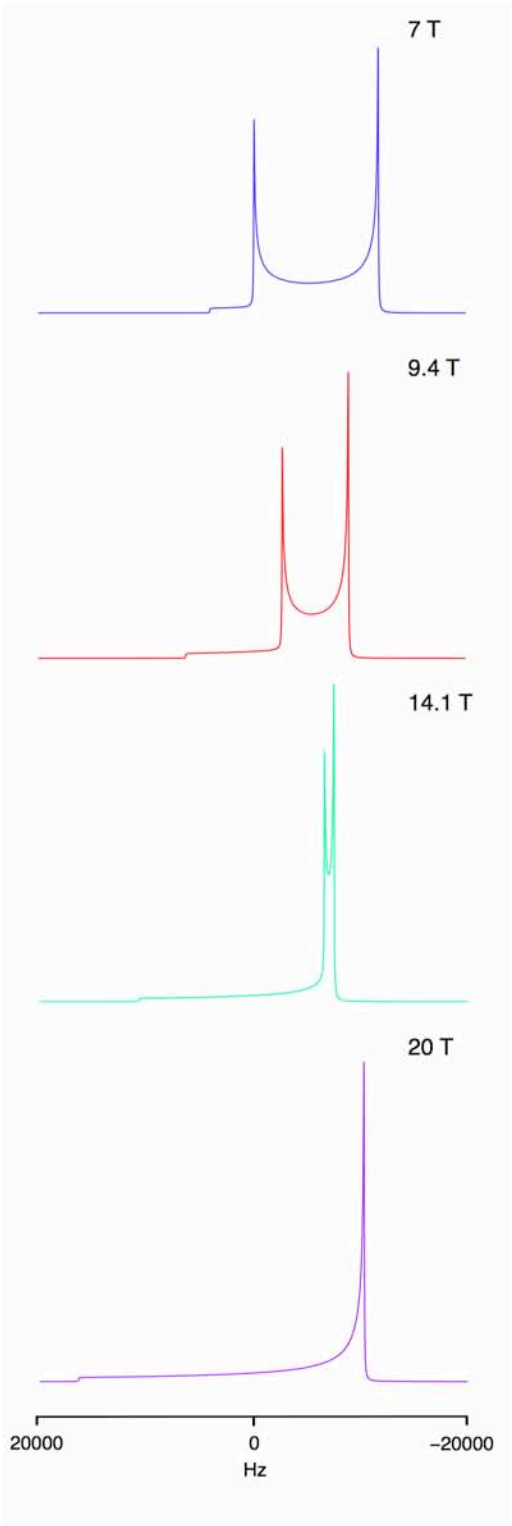

Figure 3.39: Simulated static lineshapes exhibiting contributions from both CSA and second-order quadrupolar interactions at varying B_0 fieldstrengths. Simulation parameters include $\delta_{iso} = 0$, $\Delta\sigma_{CS} = 75$ ppm, $\eta_{CS} = 0$, $C_Q = 3$ MHz and $\eta_Q = 0$.